Germán Fernández Barranco

Photodetection in intersatellite laser interferometers

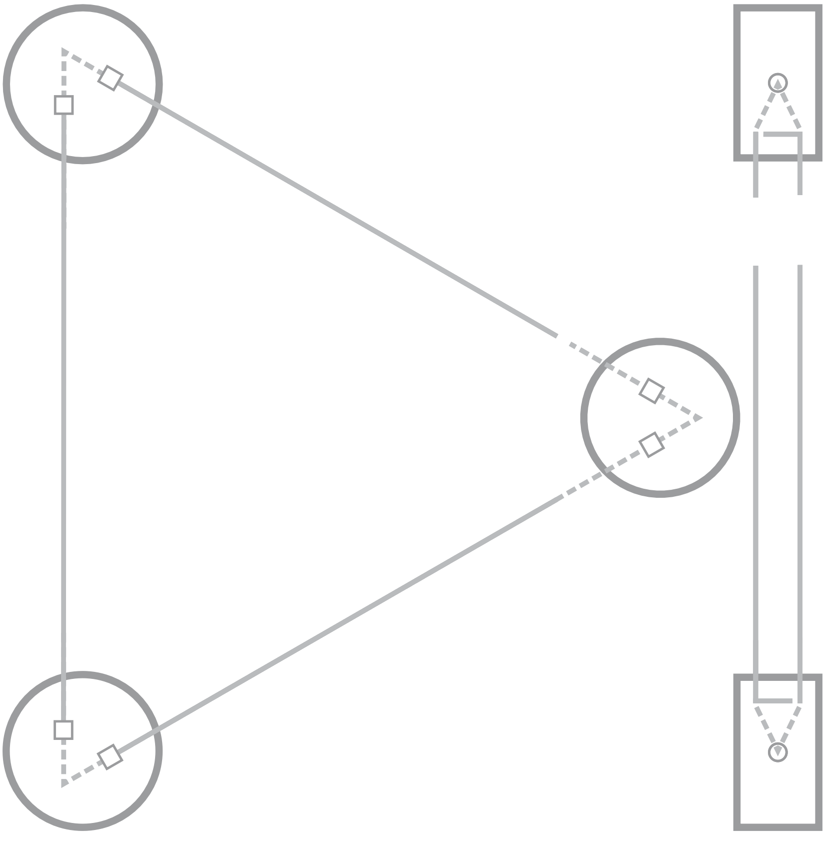

2018

Photodetection in intersatellite laser interferometers

Der Fakultät für Elektrotechnik und Informatik
der Gottfried Wilhelm Leibniz Universität Hannover
zur Erlangung des akademischen Grades

Doktor-Ingenieur
Dr.-Ing.

genehmigte Dissertation
von

M.Eng. Germán Fernández Barranco

geboren am 07. Dezember 1988
in Almería, Spanien

2018

Referent	Prof. Dr.-Ing. Wolfgang Mathis
Gutachter	apl. Prof. Dr. Gerhard Heinzel
Vorsitzender	Prof. Dr.-Ing. Heyno Garbe
Tag der Promotion	8. Dezember 2017

Our priorities now that we hold the torch
Mean we got to hold it high to illuminate the dark
And archaic
And vile

Rou Reynolds

Kurzfassung

Diese Dissertation behandelt das Design und die Charakterisierung von Photoempfängern für gegenwärtige und zukünftige Inter-Satelliten-Laserinterferometer. Der Photoempfänger, in dem die optoelektronische Wandlung der Interferenzsignale stattfindet, ist als erstes Element der Auslesekette kritisch für die Genauigkeit des Interferometers. Die Forschung im Rahmen dieser Arbeit konzentrierte sich auf Photoempfänger für den geplanten, weltraumgestützten Gravitationswellendetektor, Laser Interferometer Space Antenna (LISA), und die Gravity Recovery and Climate Experiment Follow-On (GRACE-FO) Mission, deren Ziel die Messung von Zeitvariationen im Erdschwerefeld ist.

Inter-Satelliten-Laserinterferometrie setzt aufgrund von Dopplereffekten, verursacht durch relative Satellitenbewegungen, ein heterodynes Detektionsschema voraus. Insofern müssen solche Photoempfänger mit Frequenzen bis zu 25 MHz betrieben werden können. Erschwerend kommt hinzu, dass die unvermeidbare Strahldivergenz im Zusammenspiel mit großen Inter-Satelliten-Abständen zu sehr schwachen Lichtleistungen beim Empfänger führt. Dieses Szenario erfordert Photoempfänger mit einem elektronischen Rauschen in der Größenordnung von $\mathrm{pA\,Hz^{-1/2}}$ im heterodynen Frequenzband. Außerdem darf das thermisch induzierte Rauschen des Photoempfängers die geplante Genauigkeit des Interferometers nicht verletzen. Im Falle von LISA ist zudem die erhöhte Anzahl an Photoempfängern pro Satellit zu beachten, welche wiederum den Energieverbrauch jedes einzelnen Geräts einschränkt.

In der vorliegenden Dissertation werden die Grundlagen von Inter-Satelliten-Laserinterferometrie beschrieben sowie die Anforderungen hergeleitet, die an zugehörige Photoempfänger zu stellen sind. Zudem wurde eine umfangreiche Studie zu unterschiedlichen Photoempfänger-Lösungen durchgeführt. Dabei stellten sich Quadranten-PIN-Photodioden auf Basis von Indiumgalliumarsenid (InGaAs) in Verbindung mit bipolaren Verstärkern als optimale Wahl für Inter-Satelliten-Interferometrie heraus.

Darüber hinaus werden in dieser Arbeit Methoden zur Charakterisierung von Photoempfängern vorgestellt und Resultate für verschiedene Photoempfänger-Implementierungen gezeigt. In diesem Zusammenhang wurde zudem eine Funktionalitätserweiterung der Simulationssoftware IfoCAD entwickelt, um experimentell gemessene, räumlich aufgelöste Sensitivitätsprofile realer Photodioden für Simulationen nutzen zu können. Die Charakterisierung der Photoempfänger-Flugmodelle für GRACE-FO, die vom Deutschen Zentrum für Luft- und Raumfahrt (DLR) Berlin in Zusammenarbeit mit dem Albert-Einstein-Institut (AEI) Hannover entwickelt wurden, zeigt, dass sie die

Anforderungen an Rauschen, Bandbreite, thermische Stabilität und Strahlungsresistenz erfüllen und somit für die Nutzung an Bord der beiden Satelliten freigegeben werden konnten.

Im Rahmen dieser Doktorarbeit wurde eine neue Photoempfänger-Topologie entwickelt, welche auf Heteroübergangs-Bipolartransistoren und einer herkömmlichen Quadranten-Photodiode mit 0.5 mm Durchmesser basiert. Die experimentelle Charakterisierung eines Prototyps zeigt eine 3 dB Bandbreite von 37 MHz und eine äquivalente Eingangsstromrauschdichte von $1.9\,\mathrm{pA\,Hz^{-1/2}}$ bei 25 MHz, $0.2\,\mathrm{pA\,Hz^{-1/2}}$ geringer als bei bisherigen Photoempfänger-Designs. Für die Auslesekette in LISA ist diese Reduktion des elektronischen Rauschens gleichbedeutend mit einer Verringerung des Photoempfänger-Beitrags zum relativen Längenrauschen um $0.13\,\mathrm{pm\,Hz^{-1/2}}$. Die gemessene Leistungsaufnahme des gesamten Photoempfänger-Front-Ends liegt dank der transistorbasierten Eingangsstufe und der verwendeten Operationsverstärker bei 178 mW. Dies stellt eine Verbesserung gegenüber konventionellen, rein operationsverstärkerbasierten Photoempfänger-Designs dar, die nicht auf geringe Leistungsaufnahme hin optimiert wurden. Aufgrund der genannten Eigenschaften ist dieser neue Photoempfänger-Typ ein vielversprechender Kandidat für zukünftige Inter-Satelliten-Interferometrie-Missionen.

Schlagworte: Gravitationsphysik, Inter-Satelliten-Laserinterferometrie, Photoempfänger

Abstract

This thesis describes the design and characterization of photoreceivers for present and future intersatellite laser interferometers. The photoreceiver performs the optoelectronic conversion of the interfered signals and, as the first stage of the readout chain, is critical for the interferometer sensitivity. The research focused on photoreceivers for the Laser Interferometer Space Antenna (LISA), a future space-based gravitational wave detector; and the Gravity Recovery and Climate Experiment Follow-On (GRACE-FO) mission, whose aim is to measure time variations of the Earth's gravity field.

Intersatellite interferometry requires a heterodyne scheme to cope with Doppler-induced frequency changes due to relative spacecraft motion. Therefore, the photoreceivers need to operate at frequencies up to 25 MHz. Additionally, beam divergence and a large separation between spacecraft lead to low power received signals. This requires photoreceivers with an input current noise of the order of $\mathrm{pA\,Hz^{-1/2}}$ in the heterodyne frequency band to measure the weak optical signals. The thermally induced noise of the photoreceiver must also comply with the design sensitivity of the interferometer. Another aspect to consider in LISA is the significant number of photoreceivers in a single spacecraft, which imposes tight constraints on the power consumption per device.

The thesis covers the basics of intersatellite laser interferometry and the derivation of photoreceiver requirements. It also contains an in-depth study of photoreceiver solutions. Quadrant PIN photodiodes based on indium gallium arsenide (InGaAs) and bipolar amplifiers were identified as optimal for intersatellite interferometry.

The thesis also describes photoreceiver characterization techniques and provides performance results of several photoreceiver implementations. A new functionality upgrade for the IfoCAD simulation software was developed to use experimentally measured spatial responses of photodiodes in simulated environments. The characterization of the GRACE-FO photoreceiver flight models, developed at the Deutsches Zentrum für Luft- und Raumfahrt (DLR) Berlin in collaboration with the Albert Einstein Institute (AEI), showed that the requirements for noise, bandwidth, thermal stability and radiation hardness were fulfilled, allowing the use of the units in the spacecraft.

A new photoreceiver topology featuring heterojunction bipolar transistors and an off-the-shelf 0.5 mm diameter quadrant photodiode was implemented. The experimental characterization of a prototype was found to have a 3 dB bandwidth of 37 MHz and an input current noise of $1.9\,\mathrm{pA\,Hz^{-1/2}}$ at 25 MHz, $0.2\,\mathrm{pA\,Hz^{-1/2}}$ less than in previous photoreceiver designs. The reduction of photoreceiver electronic noise translates to a $0.13\,\mathrm{pm\,Hz^{-1/2}}$ decrease of the photoreceiver contribution to the LISA readout displacement noise. The measured power consumption of the full photoreceiver is 178 mW, thanks to the low power, transistor-based input stage and the OpAmps used. This constitutes an improvement compared to standard OpAmp-only photoreceiver designs, not optimized for power consumption. Due to the described performance, this new type of photoreceiver is a competitive candidate for future intersatellite interferometry missions.

Keywords: Gravitational physics, intersatellite interferometry, photoreceivers

Contents

Kurzfassung **7**

Abstract **9**

Acronyms **13**

1 Intersatellite laser interferometry **19**
1.1 Optical metrology in space 19
1.2 LISA 21
1.3 GRACE-FO 22
1.4 Fundamentals I: Interferometry 23
1.5 Fundamentals II: Photodetection 25
1.6 The readout chain 28
  1.6.1 Optical signals 28
  1.6.2 The photoreceiver 30
  1.6.3 The phasemeter 32
  1.6.4 Noise budget and photoreceiver requirements 35

2 Photoreceiver solutions **45**
2.1 The photodetector 45
  2.1.1 Photodiode physics 46
  2.1.2 Avalanche photodiodes 49
  2.1.3 Two-dimensional materials 51
2.2 The transimpedance amplifier 51
  2.2.1 Operational amplifiers 53
  2.2.2 The DC path 58
  2.2.3 BJT vs FET 60
  2.2.4 Discrete transistors 61

3 Photoreceiver characterization **65**
3.1 Photodiode spatial response 65
  3.1.1 Spatial characterization setup 66
  3.1.2 Measured spatial response of quadrant photodiodes 67
  3.1.3 The IfoCAD extension 70

3.1.4 Simulation setup and results 71
3.2 Temperature stability of photodiodes 77
3.3 Noise and bandwidth characterization 79
3.4 The GRACE-FO photoreceiver 84
3.4.1 Radiation hardness 85
3.4.2 Noise and bandwidth 87
3.4.3 Phase thermal stability 88
3.5 A photoreceiver for LISA based on discrete transistors 95

4 Summary and outlook **103**

Appendix **107**

Bibliography **123**

Acknowledgments **125**

Curriculum Vitae **127**

Publications **129**

Acronyms

AAF anti-aliasing filter

ADC analog-to-digital converter

ADPLL all-digital phase-locked loop

AEI Albert Einstein Institute

APD avalanche photodiode

ATA advanced tilt Actuator

BJT bipolar junction transistor

BMBF Bundesministerium für Bildung und Forschung

C/N_0 carrier-to-noise density

CHAMP Challenging Mini-satellite Payload

DAQ data acquisition

DLR Deutsches Zentrum für Luft- und Raumfahrt

DUT device under test

DWS differential wavefront sensing

EOM electro-optic modulator

ESA European Space Agency

ETS-6 Engineering Test Satellite - 6

FET field effect transistor

FPGA field-programmable gate array

GaAs gallium arsenide

GBWP gain bandwidth product

GOCE Gravity field and steady-state Ocean Circulation Explorer

GRACE Gravity Recovery and Climate Experiment

GRACE-FO Gravity Recovery and Climate Experiment Follow-On

GRS gravitational reference sensor

HBT heterojunction bipolar transistor

InGaAs indium gallium arsenide

JPL Jet Propulsion Lab

LED light emitting diode

LIGO Laser Interferometer Gravitational-Wave Observatory

LISA Laser Interferometer Space Antenna

LNA low noise amplifier

LOB LISA optical bench

LPF LISA Pathfinder

LPS longitudinal pathlength signal

LRI Laser Ranging Interferometer

MELF metal electrode leadless face

NASA National Aeronautics and Space Administration

NCO numerically controlled oscillator

NPRO non-planar ring oscillator

OpAmp operational amplifier

PCB printed circuit board

PI proportional-integral

PRB photoreceiver back-end

PRF photoreceiver front-end

QPD quadrant photodiode

RF	radio frequency
RFGW	response function to gravitational waves
RIN	relative intensity noise
RMS	root mean square
RTD	resistance temperature detector
SiGe:C	silicon-germanium:carbon
SiGe	silicon-germanium
SNR	signal-to-noise ratio
SPICE	Simulation Program with Integrated Circuit Emphasis
STELA	Satellite Test Environment for Laser Applications
STI	SpaceTech GmbH
TDI	time-delay interferometry
TIA	transimpedance amplifier
TVAC	thermal vacuum chamber

List of Figures

1.1 Basic principle of displacement measurements with optical interferometry 20
1.2 Orbit configuration of the LISA mission 22
1.3 Picture of the GRACE-FO satellites 24
1.4 Electric field and intensity for homodyne and heterodyne interferometry 26
1.5 Basic scheme of the photodetection process 27
1.6 LISA subsystems and interaction 29
1.7 Scheme of an intersatellite interferometer arm 30
1.8 Block diagram of the readout chain 31
1.9 Scheme of a quadrant photodetector and DWS 32
1.10 Block diagram of the phasemeter ADPLL 34
1.11 Strain sensitivity of LISA and detectable sources 36
1.12 Block diagram of the full readout chain in LISA 41
1.13 Phase noise budget for a LISA photoreceiver 43

2.1 Responsivity versus wavelength for germanium, silicon and InGaAs . . 49
2.2 Simple electrical model of a photodiode 50
2.3 Circuit diagram of a resistor-based TIA 52
2.4 Photoreceiver electronic noise representation 53
2.5 Schematic of the OpAmp-based TIA 54
2.6 Frequency response of an OpAmp-based TIA 56
2.7 Noise in an OpAmp-based TIA 57
2.8 Input current noise density for several OpAmps 59
2.9 Circuit diagram of the split TIA configuration 60
2.10 Circuit diagram of a transistor-based TIA 62
2.11 Bipolar junction transistor noise model 63

3.1 Setup for the spatial response characterization of photodiodes 67
3.2 Normalized spatially resolved response of the QP22 68
3.3 Normalized spatially resolved response of the GAP9119 69
3.4 Normalized spatially resolved response of the FCIQ1000 69
3.5 Flowchart of an IfoCAD simulation with the extension for measured QPD responses 71
3.6 Scheme of the IfoCAD simulation setup 72

3.7 Simulated horizontal DWS signal for yaw tilts 73
3.8 QPD spatial responses featured in IfoCAD simulations 74
3.9 Simulated horizontal DWS signal for yaw tilts at $P_\mathrm{e} = 1$ mm for all cases 75
3.10 Simulated longitudinal signal for yaw tilts 76
3.11 Simulated longitudinal signal for yaw tilts at $P_\mathrm{e} = 1$ mm for all cases . . 76
3.12 Setup for the thermal characterization of photodiodes 77
3.13 Ratio $V_\mathrm{DUT}V_\mathrm{REF}^{-1}$ versus temperature for a silicon-based photodiode . . . 78
3.14 Picture of a PC50-7 sample tested in STELA 79
3.15 Setup diagram for photoreceiver characterization with the white light method 81
3.16 Picture of a laser diode and its custom-made driver 82
3.17 Picture of a 16-channel TIA design for the LOB and ATA experiments . 83
3.18 Optical frequency response of the 16-channel TIA 84
3.19 Picture of the hexagonal interferometer testbed 85
3.20 Circuit diagram of the TIA from the GRACE-FO photoreceiver 86
3.21 Block diagram of the GRACE-FO photoreceiver 86
3.22 Input noise density $\tilde{\imath}_\mathrm{en}$ for the GRACE-FO photoreceiver 88
3.23 Frequency response of the GRACE-FO photoreceiver 89
3.24 Setup for the TVAC test of the GRACE-FO photoreceivers 90
3.25 Picture of the three photoreceiver flight models of GRACE-FO 90
3.26 Quadrant photodiode diagram and DWS signals description 91
3.27 Longitudinal phase stability of the GRACE-FO photoreceiver 93
3.28 Differential phase stability of the GRACE-FO photoreceiver 93
3.29 Phase noise budget of the GRACE-FO photoreceiver 94
3.30 Circuit diagram of the HBT-based photoreceiver for LISA 96
3.31 Picture of the HBT-based photoreceiver for LISA 98
3.32 HBT-based photoreceiver input current noise at different collector currents 99
3.33 HBT-based photoreceiver input current noise for all 4 channels 101
3.34 HBT-based photoreceiver input current noise for different photodiodes 101

1 Intersatellite laser interferometry

This first chapter of the thesis is an introduction to the field of intersatellite laser interferometry and the photoreceiver. The photoreceiver, the first component of the interferometer readout chain, is the central element of this work. The motivation for developing intersatellite laser interferometers is discussed in Section 1.1 in terms of scientific and technical goals. Sections 1.2 and 1.3 delve into this motivation by presenting the LISA mission, a gravitational wave observatory based entirely on intersatellite laser interferometry, and the GRACE-FO mission, a geodesy project which will benefit from this technology as well. Sections 1.4 and 1.5 analyze two fundamental concepts in physics and engineering that are basic for the field: interferometry and photodetection. At the end of the chapter, Section 1.6 dissects the readout chain of the interferometer and describes the instrument noise budget. Photoreceiver requirements can be derived from the noise budget to set a frame of work for the photoreceiver design, development and characterization.

1.1 Optical metrology in space

Optical metrology involves the use of light to measure magnitudes such as time and distance with high precision. In general, distance measurements based on optical metrology can employ a time of flight or an interferometric scheme [1]. The latter is the core technology of the Laser Interferometer Gravitational-Wave Observatory (LIGO), a pair of multi-kilometer Michelson-like interferometer detectors aimed at observing gravitational waves in the 10 Hz - 10 kHz frequency range [2]. The basic idea behind the measurement scheme can be seen in Figure 1.1. The phase difference $\Delta\phi$ between the two interfered light beams is related to the relative displacement ΔL between the test masses of the interferometer (also known as end mirrors). The phase extraction depends on the specific interferometer implementation. Equation 1.1 [1] shows how the light wavelength λ relates both magnitudes.

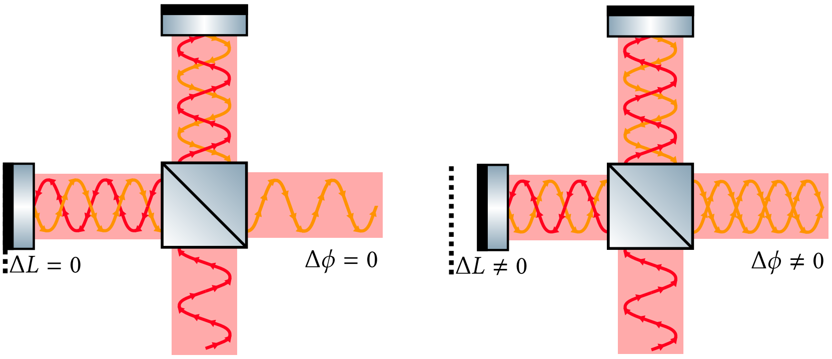

Figure 1.1: The phase difference $\Delta\phi$ between the two interfered light beams is related to the relative displacement ΔL between the test masses of the interferometer (also known as end mirrors). The wavelength of the light relates both magnitudes according to Equation 1.1. The phase extraction technique is a characteristic of the specific interferometer implementation.

$$\begin{aligned} \Delta L &= \frac{\lambda}{2\pi}\Delta\phi, \\ [\Delta L] &= \mathrm{m}. \end{aligned} \tag{1.1}$$

The most prominent astrophysical gravitational wave sources in the LIGO frequency band are supernovae and compact binary inspirals, formed by neutron stars or black holes. Advanced LIGO, an upgraded version of the original detectors, presented a strain sensitivity of $1 \times 10^{-23}\,\mathrm{Hz}^{-1/2}$ at 100 Hz during its first observation run. This sensitivity corresponds to a relative displacement between the test masses of about $1 \times 10^{-20}\,\mathrm{m\,Hz}^{-1/2}$ [2]. This unprecedented precision of displacement measurements allowed LIGO to detect a gravitational wave for the first time in history in September 2015 [3]. The detection marked the beginning of a new era in astronomy, confirmed by three more black hole coalescences detected in the following years [4] [5] [6] and the first observation of a binary neutron star inspiral in August 2017 [7]. The observed electromagnetic counterpart after the binary neutron star coalescence represented a breakthrough for multi-messenger astronomy.

LIGO features an outstanding strain sensitivity at the design frequency band and future upgrades will enhance its performance even further. However, gravity-gradient noise represents a hurdle difficult to overcome at low frequencies [8]. The mHz gravitational wave band promises unique insights into astrophysics processes. That includes supermassive black hole binaries, extreme mass ratio inspirals and white dwarf binaries. These sources cannot be tracked by LIGO due to its low-frequency limitation. For this reason, an international effort was carried out to design a space-borne gravitational wave detector that could deliver the science of the mHz gravitational wave spectrum. The Laser Interferometer Space Antenna (LISA) was the result of this endeavor. LISA, whose first design dates back to the early ’90s, was chosen by the European Space Agency (ESA) as its third large-class mission (L3) on June 17, 2017. LISA, just as LIGO, relies on laser interferometry for gravitational wave detection. On the other hand, LISA uses optical heterodyne interferometry (as opposed to the homodyne scheme of LIGO) to cope with the Doppler effect present in an intersatellite detector [9]. A more detailed description of the LISA mission can be found in Section 1.2.

Gravitational wave astronomy is not the only field that can benefit from optical metrology in space, which has the potential to improve orbital geodesy experiments as well. The Gravity Recovery and Climate Experiment Follow-On (GRACE-FO) mission will include an intersatellite laser interferometer to enhance the precision at which time-variations of the Earth’s gravity field are measured. The laser interferometer in GRACE-FO is partially based on technology developed for the LISA mission [10]. Details about GRACE-FO can be found in Section 1.3.

1.2 LISA

LISA will be the first gravitational wave detector in space. The LISA concept is based on measuring changes in the distance between test masses contained in three identical spacecraft orbiting around the sun. Gravitational waves will cause variations in the LISA constellation arms (circa 2.5 Gm long), which will be observable within the detector frequency band (0.1 mHz-100 mHz). Figure 1.2 depicts the configuration of the LISA mission during operation. The equilateral triangle, formed by the spacecraft and the laser links, follows the Earth along its orbit around the Sun. The mission shares similarities with the LIGO detectors, in which distance variations between test masses are tracked using a Michelson-like laser interferometer (see Figure 1.1). Although there is some shared technology with ground-based detectors, LISA uses a different interferometric approach: optical heterodyne interferometry. This method can handle Doppler-induced frequency dynamics in the science signal, which are a consequence of relative velocity changes of the spacecraft. Additionally, a space mission like LISA requires particular considerations in the design and development of the interferometer units and other spacecraft systems due to the harsh environment during launch and operation. This includes mechanical and thermal stability, radiation hardness and power consumption. Testing the performance of some of these units is also a challenging task on ground. The need for an experimental verification of some key technologies for LISA led to the development of LISA Pathfinder (LPF), a single satellite proof-of-concept mission [9].

LPF was launched on December 3, 2015. The total mission duration was 576 days, during which LPF successfully tested the technologies included in its payload. LPF demonstrated the feasibility of having two free-falling test masses within a spacecraft

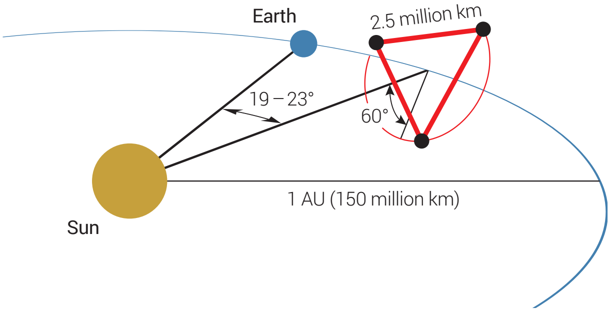

Figure 1.2: Configuration of the LISA mission during operation. The equilateral triangle formed by the three identical spacecraft and the laser links follows the Earth along its orbit. Gravitational waves will cause variations in the LISA constellation arms (circa 2.5 Gm long), which will be detectable within the detector frequency band (0.1 mHz-100 mHz) [9].

with sub-femto g $\mathrm{Hz}^{-1/2}$ acceleration noise [11]. It was also a confirmation of the reliability, stability and robustness of all tested subsystems in orbit, including the interferometric measurements, micronewton thrusters or the test mass capacitive sensing and electrostatic suspension.

LPF results represent a decades-long effort to conceive a mature design for a space-based gravitational wave observatory, which led to the selection of LISA as the L3 mission by the ESA [12]. In the following years, the development of the different LISA units will be distributed among the members of an international consortium.

There is a continuing scientific effort to find the optimal solution for elements of the mission such as the backlink [13], the telescope [14] or the laser [15]. In a similar fashion, the work in this thesis focuses on finding an optimal design for the LISA photoreceiver.

1.3 GRACE-FO

In the last fifteen years, space-borne gravimetric geodesy missions such as the Challenging Mini-satellite Payload (CHAMP), the Gravity field and steady-state Ocean Circulation Explorer (GOCE) or the Gravity Recovery and Climate Experiment (GRACE) provided useful scientific data that improved our understanding of physical phenomena on Earth that can be observed by their gravitational influence. These phenomena include the evolution of underground water supplies, changes in flood patterns, ocean currents or observations of ice loss. Our ability to quantify these phenomena is highly relevant to our predictions in climate science, which is a topic of international concern nowadays. The original GRACE mission was launched in 2002 with the goal of mapping time variations of the Earth's gravity field. A K-Band microwave ranging system measured fluctuations in the distance between two spacecraft induced by local variations of the gravity field. The spacecraft were separated by 220 km (nominal) and followed a polar orbit [16]. The success of the mission and the importance of avoiding a science data gap motivated the prompt construction of the GRACE Follow-On (GRACE-FO) satellites. The design of GRACE-FO is primarily based on the previous mission, but with a significant addition: a Laser Ranging Interferometer (LRI). The LRI has the potential to improve the precision of intersatellite displacement measurements from the $10\,\mu\mathrm{m\,Hz^{-1/2}}$ of the K-Band microwave instrument down to $80\,\mathrm{nm\,Hz^{-1/2}}$ [10]. Figure 1.3 is a picture of the two GRACE-FO satellites in a clean room at the iABG facilities in Munich (2017).

The LRI in GRACE-FO is considered a technology demonstrator since it will become the first intersatellite laser interferometer in operation. The LRI employs a scheme based on optical heterodyne interferometry and therefore its technology resembles that of the LISA mission. GRACE-FO partially inherits components developed within the frame of LISA, which includes the phase metrology system (or phasemeter, more in Section 1.6.3), the laser [17] and the photoreceivers.

Part of this thesis is related to the design, characterization and testing of the photoreceivers for GRACE-FO, from early prototypes to the final flight hardware installed in the spacecraft. The GRACE-FO photoreceivers were developed at the DLR Berlin in a close collaboration with the AEI. A description of the GRACE-FO photoreceivers and their performance can be found in Section 3.4.

1.4 Fundamentals I: Interferometry

The wave equation and its modifications have found application in a wide variety of fields, from acoustics to quantum mechanics. The electromagnetic wave equation describes the propagation of electromagnetic waves, like those emitted by lasers in intersatellite interferometry. Assuming that two electromagnetic waves of the same frequency f_0 are superimposed, the resulting wave carries information about the phase difference between the original waves ϕ, as described by Equation 1.2 [18, p. 64].

$$\begin{aligned} I_\mathrm{T} &= I_1 + I_2 + 2(I_1 I_2)^{1/2}\cos(\phi), \\ [I_\mathrm{T}] &= \mathrm{W\,m^{-2}}. \end{aligned} \tag{1.2}$$

I_1 and I_2 are the intensities of the initial waves and I_T is the intensity of the resulting

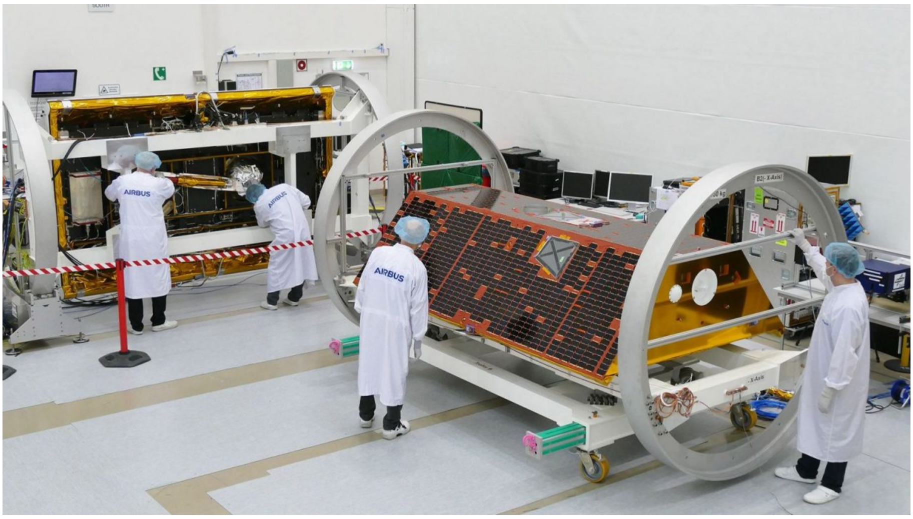

Figure 1.3: The two GRACE-FO satellites in a clean room at the iABG facilities in Munich, Germany. The assembly of the final components finished in the second half of 2017. In 2016 and 2017, a series of tests at spacecraft level verified all requirements prior to launch. This included environmental and functionality tests. Image credit: Airbus DS GmbH, Mathias Pikelj.

wave. The mechanism described by Equation 1.2 is called interference, and interferometry is any set of techniques used to exploit this effect to extract information [18]. I_T also contains a time-variable component at $2f_0$ which is not considered. In laser metrology, f_0 is of the order of THz and practical detectors cannot track intensity changes at that speed [19, p. 35]. The calculation of the electromagnetic wave intensity for a given electric field strength can be found in [19, p. 36] [20] [21, p. 2].

Even though nowadays it seems intuitive to use wave theory and interference to describe features observed in everyday objects such as strings or water, it was not until the early 19th century when Thomas Young introduced these concepts. Young studied these phenomena first in sound waves and later in light. His famous double-slit experiment was part of this work and helped him establish the wave theory of light [22] [23]. From that point on, wave interference was studied as a phenomenon itself but also became a useful tool to analyze different physical magnitudes. The Jamin interferometer (1856) was used to measure the refractive index and dispersion of gases [24]. In 1887, Michelson and Morley conducted their famous interferometric experiment to demonstrate the existence of aether. Their negative result set the foundation for Einstein's Special Theory of Relativity [25].

In the 20th century, astronomical observations continued benefiting from interferometry by interfering signals in radio telescope arrays [26]. Other fields studying wave-like phenomena also started applying this technique extensively. Examples are seismology [27], acoustics [28] and, recently, atomic interferometers [29].

The invention of the laser in 1960 [30] marked a milestone in optical metrology and interferometry. Lasers produce light with a narrow linewidth and high spatial coherence, which enables greater precision for length measurements using interferometers. Improvements in the frequency stabilization of lasers using optical resonators allowed the field of interferometric gravitational wave detectors to flourish [31]. Frequency noise couples into displacement noise due to the interferometer arms mismatch in real interferometers. In the presence of exactly equal arms, the frequency noise would not play a role in the interferometer precision [32].

In both LISA and GRACE-FO, a change of the relative velocity between spacecraft produces frequency variations of the received light due to the Doppler Effect (see Section 1.6.1). Equation 1.3 [19, p. 37], a modification of Equation 1.2, shows the intensity of the resulting wave when there is a frequency difference ($f_{\mathrm{Diff}} = f_1 - f_2$) between the interfered waves.

$$I_{\mathrm{T}} = I_1 + I_2 + 2(I_1 I_2)^{1/2} \cos(2\pi f_{\mathrm{Diff}} t + \phi). \tag{1.3}$$

Again, I_{T} contains THz components at $2f_1$, $2f_2$ and $f_1 + f_2$ [33, p. 9] which cannot be tracked with practical detectors. On the other hand, the $f_1 - f_2$ component can be tracked if the frequency difference falls within the detector band. Figure 1.4 shows the electric field strength of the two interfered waves (left) and the intensity of the resulting wave I_{T} (right) over time, for the two cases described by Equations 1.2 and 1.3. In the top-left corner, two waves with the same frequency and phase are considered. The resulting intensity I_{T}, in the top-right corner, is constant over time. This corresponds to the output of a homodyne detector. In the bottom-left corner, the two waves have different frequencies, yielding a resulting intensity I_{T} which changes over time at a frequency $f_{\mathrm{Diff}} = f_1 - f_2$ (bottom-right). The latter scenario corresponds to a heterodyne interferometer.

1.5 Fundamentals II: Photodetection

Photodetection is used in light-based interferometers to convert an optical signal into an electrical signal. The process of photodetection has different forms, classified according to the change produced by the incident light on the detector. The first kind of photodetectors in history could be considered those related to photochemistry or photography, namely photosensitive materials [34]. The discovery of the photovoltaic and the photothermal effects happened shortly after, bringing more sophisticated ways to link the phenomenon of light with electrical properties of materials [35].

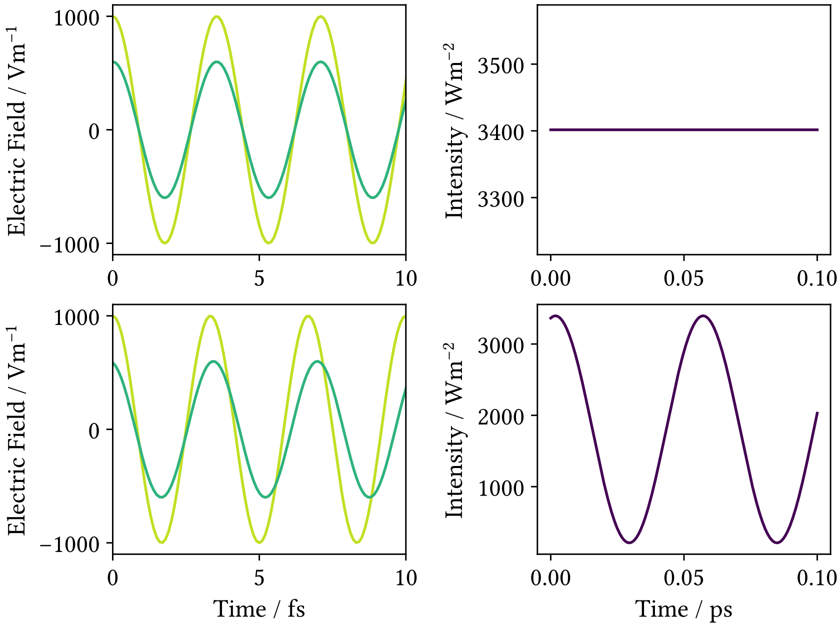

Figure 1.4: Electric field strength of the interfered waves (left) and intensity of the resulting wave (right). The plots in the upper row correspond to a homodyne detector, where the two interfered waves have the same frequency. The resulting intensity I_T is given by Equation 1.2. The lower row corresponds to a heterodyne detector, where I_T is given by Equation 1.3. Homodyne interferometry is used in ground-based gravitational wave detectors. Intersatellite laser interferometers, such as LISA and GRACE-FO, feature heterodyne interferometry. The calculation of the electromagnetic wave intensity for a given electric field strength can be found in [19, p. 36] [20] [21, p. 2].

In today's world, a variety of photodetectors based on these effects are available, and some of their properties are discussed in Section 2.1. Photodetectors used in laser interferometers operate according to the internal photoelectric effect in semiconductor devices. In this process, sufficiently energetic light impinging on the photodetector liberates electrons in a semiconductor crystal. The free electrons can move within the semiconductor material and can potentially contribute to the current flowing through the device. The number of free electrons is proportional to the light intensity [36]. This mechanism was mainly described by Einstein in his 1905 paper [37], with the only difference being the free electrons in Einstein's theory would escape the material (cathode) and travel through a gas or vacuum, like in classical phototubes.

Understanding how light creates free electrons in a semiconductor crystal is not trivial. The most accurate and universal theory of light which describes this effect is quantum electrodynamics [38]. This section contains a more practical explanation, centered around the photodetector function within the interferometer.

Equation 1.2 described the intensity of the resulting wave after interference. We can obtain the power P_T of this wave by integrating over a given surface S, as seen in Equation 1.4 [19, p. 37].

$$\begin{aligned} P_\mathrm{T} &= \int_S I_\mathrm{T} \cdot \mathrm{d}A, \\ [P_\mathrm{T}] &= \mathrm{W}. \end{aligned} \tag{1.4}$$

If we assume planar wavefronts with an ideal overlap over S, and define $P = IS$, the power of the resulting wave is given by Equation 1.5 [19, p. 37].

$$P_\mathrm{T} = P_1 + P_2 + 2(P_1 P_2)^{1/2} \cos(2\pi f_\mathrm{Diff} t + \phi), \tag{1.5}$$

where P_1 and P_2 are the powers of the interfered light waves. The photodetector is a semiconductor crystal that can convert the incident power from Equation 1.5 into a stream of electrons per second, the photocurrent I_photo, as shown in Figure 1.5. The conversion factor R is called responsivity, and it depends on the material properties, structure, and dimensions. Equation 1.6 defines the generated photocurrent [39, p. 5].

$$\begin{aligned} I_\mathrm{photo} &= R P_\mathrm{T}, \\ [I_\mathrm{photo}] &= \mathrm{A}. \end{aligned} \tag{1.6}$$

The responsivity also depends on the frequency of the incident light. Section 2.1.1 further elaborates on the properties of semiconductor photodetectors and the value of R.

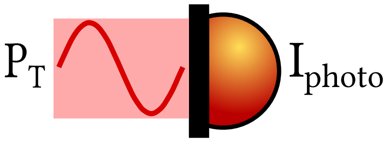

Figure 1.5: In the photodetection process, light intensity over a given area is converted into a photocurrent. This linear conversion is given by the photodetector responsivity R.

1.6 The readout chain

An intersatellite laser interferometer is a complex setup formed by several subsystems. Each of them performs tasks which happen either solely within the subsystem or interacting with the rest of the subsystems. In the case of LISA, the main subsystem considered are the following:

- Gravitational reference sensor (GRS): Each gravitational reference sensor (GRS) contains a test mass which acts as the geodesic reference of the interferometer. The main task of the GRS is to read the position of the test mass and maintain its free fall without introducing acceleration noise. The position of the test mass can be controlled within the GRS by means of capacitive sensing and electrostatic suspension. The interferometric readout can also be used as a reference for the test mass position control.
- Optical system: It includes all the optical components of the interferometer. They are mostly passive components, such as beam splitters (BS) and mirrors, with two active components being electro-optic modulators (EOMs) and the laser source. The active components can modify the optical signals dynamically, as commanded by an element of the readout chain: the phasemeter (section 1.6.3).
- Readout chain: The elements in the readout chain capture the optical signals and process them to either extract the main science information or to control the spacecraft or other subsystems.

Figure 1.6 shows the basic interactions between the three main LISA subsystems described above. This section expands on the elements of the readout chain.

1.6.1 Optical signals

In this text, the optical signals to be detected and processed are not considered an intrinsic part of the readout chain. On the other hand, their parameters set the requirements for the readout components. A detailed description of the laser sources used in GRACE-FO or proposed for LISA are out of the scope of this thesis, but can be found in [15] [17]. In a similar fashion, the properties of the optical bench, where the optical signals interfere, were reported in [9], [40] and [41].

The optical signal to be detected in the long-arm interferometer is produced by the interference of two light beams in the near-infrared range (1064 nm): the beam from the local spacecraft (LO beam) and the received beam from the distant spacecraft (RX beam). The optical power of the interfered beams is orders of magnitude apart. The LO beam power is at the mW level, whilst the RX beam power is of the order of pW due to the great divergence of the beam after propagating along the 2.5 Gm arm. The process is reciprocal in that the local spacecraft also sends a beam to the

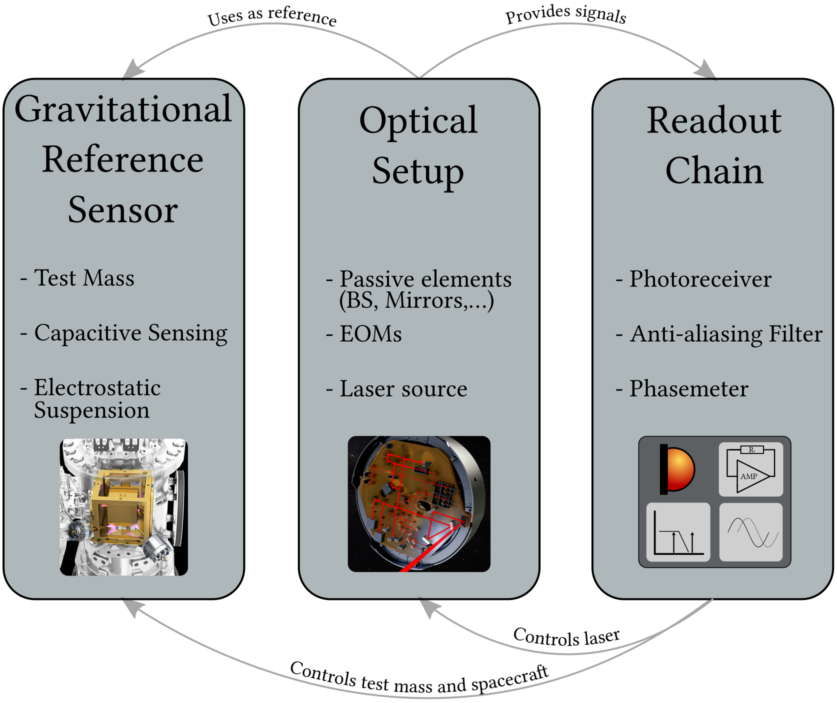
Uses as reference
Provides signals
Gravitational Reference Sensor
- Test Mass
- Capacitive Sensing
- Electrostatic Suspension
Optical Setup
- Passive elements (BS, Mirrors,...)
- EOMs
- Laser source
Readout Chain
- Photoreceiver
- Anti-aliasing Filter
- Phasemeter
AMP
Controls laser
Controls test mass and spacecraft

Figure 1.6: Main three subsystems in LISA and their interactions. The GRS contains the free floating test mass used as geodesic reference. The position of the test mass is measured by the GRS itself via capacitive sensing or by the readout chain using the interferometric signals from the optical setup. The test mass position is controlled using electrostatic suspension or spacecraft motion. The readout chain also provides the science data. Pictures from ESA/ATG Medialab.

remote spacecraft. The end mirror of a traditional Michelson interferometer is replaced in intersatellite interferometry by one of the spacecraft acting as transponder. The transponder tracks the phase of the received signal and sends an equivalent, high power copy back to the local spacecraft, also known as master spacecraft. As mentioned in Section 1.4, the relative motion of the satellites creates a frequency shift (f_{Doppler}) in the RX beam due to the Doppler Effect. Since the Doppler-shifted signal is tracked and copied by the transponder, the frequency of the RX beam at the master spacecraft is $2 \times f_{\text{Doppler}}$ apart from the original LO beam. Additionally, a frequency offset is added to the copy to avoid zero crossings when f_{Doppler} changes signs. That occurs when the spacecraft change from approaching to moving away from each other or vice versa. The interfering process described above is depicted in Figure 1.7.

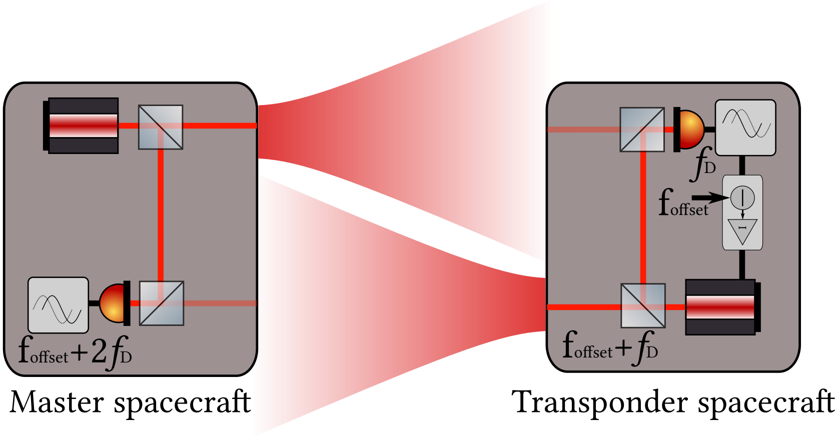

Figure 1.7: Scheme of an intersatellite interferometer arm. An optical beam is sent to the distant spacecraft, where the received beam is of the order of pW due to divergence and long intersatellite distances. One of the spacecraft acts as transponder sending back a copy of the received beam, which is Doppler-shifted due to spacecraft relative motion. The frequency of the RX beam at the master spacecraft is $2 \times f_{\text{Doppler}}$ apart from the original sent beam. A frequency offset is added to the copy to avoid zero crossings.

Using Equation 1.5, assuming an ideal heterodyne efficiency and with P_{LO} and P_{RX} being the power of the interfered beams on the photodetector surface, the total optical power is given by Equation 1.7.

$$P_{\text{T}} = P_{\text{LO}} + P_{\text{RX}} + 2(P_{\text{LO}}P_{\text{RX}})^{1/2}\cos(2\pi(f_{\text{offset}} \pm 2f_{\text{Doppler}})t + \phi), \tag{1.7}$$

where f_{Diff} was replaced by $f_{\text{offset}} \pm f_{\text{Doppler}}$. Equation 1.7 summarizes well the requirements for the readout chain, which needs to detect and process an optical signal with:

- A DC component in the µW range (with P_{LO} as main contributor).
- An AC beat-note in the nW range (greatly reduced by the pW level of P_{RX}), and with a variable frequency of up to 25 MHz in the case of LISA [19, p. 41]. For GRACE-FO, this value is 13 MHz.

1.6.2 The photoreceiver

As briefly introduced in Section 1.5, the photodetector of an intersatellite laser interferometer is a semiconductor device that converts the incoming light into free electrons. These free electrons or carriers can subsequently contribute to a current, also known

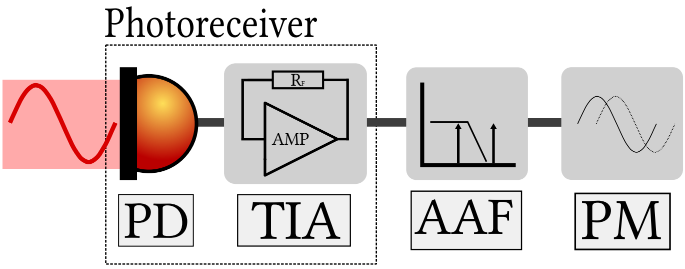

Figure 1.8: Block diagram of the readout chain with the photoreceiver elements on the left side. In general, the photoreceiver in this text represents the combination of a photodetector (PD) and the transimpedance amplifier (TIA). The other elements of the readout chain are the anti-aliasing filter (AAF) and the phasemeter (PM).

as photocurrent (I_{photo}). The amount of photocurrent is proportional to the power of the incident light and the conversion factor is given by the responsivity R, as seen in Equation 1.6. In Section 2.1, the properties of the semiconductor material which define the value of R are discussed. In practice, photodetectors come together with a transimpedance amplifier (TIA) of some sort. The TIA is a set of electronics that converts the photocurrent into voltage. For this reason, it was traditionally called a current-to-voltage converter [42]. The simplest form of TIA would be a single shunt-resistor. Different TIA approaches are more adequate depending on photocurrent parameters like amplitude or frequency, or the equivalent impedance of the photodetector. In Section 2.2, the TIA is analyzed in order to find the optimal solution for the requirements of intersatellite laser interferometry.

It is common to find diverse nomenclature in the bibliography regarding photodetection devices. In this text, the concept of photoreceiver refers to the combination of a photodetector and a TIA, as seen in Figure 1.8. This definition is widely-accepted by the scientific community and by industry manufactures.

In some cases, additional electronic stages are included in the photoreceiver for filtering, amplifier gain selection or voltage regulation. From these additional stages, the most critical in terms of photoreceiver performance is the anti-aliasing filter (AAF). The AAF, shown in Figure 1.8, removes frequency components outside the targeted band of the readout chain. By doing this, unwanted high frequency components of the signal do not downconvert when the output voltage from the photoreceiver is digitized at the phasemeter (Section 1.6.3). Alternatively, the AAF can be localized in the phasemeter, an approach used for example in the elegant breadboard model of the LISA phasemeter [43, p. 13]. In other cases, such as in the GRACE-FO mission, the photoreceiver includes the AAF (see Section 3.4).

A distinctive characteristic of photoreceivers in intersatellite laser interferometers

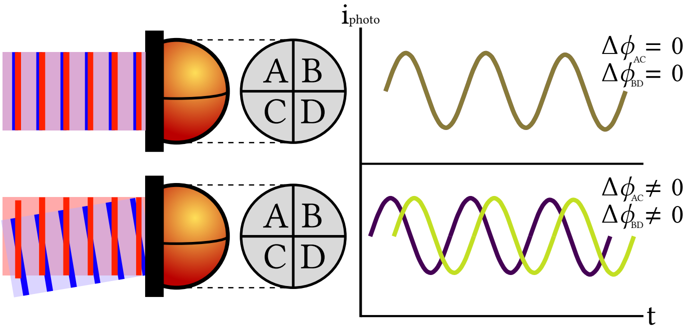

Figure 1.9: Quadrant detectors, with four independent photosensitive surfaces adjacent to each other, can provide information about the angular misalignment between the beams via DWS. Beams impinging at different angles produce unequal phases in the various segments. For example, $\Delta\phi_{\mathrm{AC}}$ is the phase difference between the beat-notes from segments A and C. The longitudinal displacement is proportional to the average phase of all four segments.

is the segmented structure of the photodetector, usually a quadrant photodiode (QPD). The four independent photosensitive surfaces of a QPD are used to measure the angular misalignment between the interfered beams. The technique used for this purpose is called differential wavefront sensing (DWS) [10, p. 7]. Figure 1.9 shows the idea behind DWS. The wavefronts are shown as straight red or blue lines in the example. Two light beams impinging at different angles will produce beat-notes with unequal phases in the various segments, since the phase difference between the interfered electromagnetic waves changes across the QPD surface. The angular misalignment can be derived from the four beat-notes. In homodyne detection, fringe patterns appear when the phase relationship between the interfered electromagnetic waves changes across the detector surface. With a QPD, the longitudinal displacement described in Equation 1.1 is proportional to the average phase of all four QPD segments.

Finding the optimal photoreceiver for intersatellite laser interferometers is the core of this thesis. The qualitative photoreceiver requirements presented at the end of Section 1.6.1 are described quantitatively at the end of Section 1.6.4.

1.6.3 The phasemeter

The phasemeter, or phase metrology system, is an element of the readout chain with three main functionalities:

- Digitize the analog voltage produced by the photoreceiver.
- Track the frequency and phase of the beat-note.

- Lock the laser of the transponder spacecraft.

From the perspective of the photoreceiver, the specifications of the analog-to-digital converter (ADC) that performs the digitization of the signal are important. The photoreceiver output voltage cannot be greater than the ADC input range to avoid saturation. Additionally, the ADC sampling frequency sets the maximum frequency component of the photoreceiver signal for which aliasing does not occur (Nyquist frequency). Higher frequency components should be filtered out in the AAF, mentioned in the previous section, located either in the photoreceiver or in the phasemeter prior to the ADC [19, p. 59]. For LISA, the proposed sampling frequency is $80\,\mathrm{MS\,s^{-1}}$ [9]. The sampling jitter at the ADC is a known phase noise source. A pilot tone is used to correct for this effect, with the downside of creating potential crosstalk between readout channels. The pilot tone itself jitters, but this effect can be compensated in post-processing [44, p. 98].

Once the signal is digitized, the phase is tracked by means of an all-digital phase-locked loop (ADPLL). The basic idea is that the input signal is mixed with a sinusoidal wave of equal frequency produced by an adjustable oscillator. The DC component of the mix is fed back to the oscillator, which keeps the lock and provides the instantaneous frequency and phase. The ADPLL is implemented in a field-programmable gate array (FPGA), which provides the required parallel processing capabilities. Figure 1.10 shows a block diagram of the ADPLL. The digitized signal is mixed with a sine wave of the same frequency and phase, which is produced by a numerically controlled oscillator (NCO). The result of this mixing is a product near DC and a product at twice the signal frequency. A low-pass filter removes the high frequency component, leaving only the quadrature component of the signal (Q). The Q value is the error signal, which is very close to zero if the NCO correctly generates a copy of the input signal in terms of frequency and phase. In order to do that, changes in the Q value are processed first by a proportional-integral (PI) controller. An initial frequency is added to the output of the PI controller. This initial frequency f_i is needed to start the ADPLL near the actual beat-note frequency. The output of the PI controller feeds the NCO, which is a combination of:

- The phase increment register (PIR), which contains the instantaneous frequency.
- The phase accumulator (PA), which contains the instantaneous phase. This register can be used therefore to extract information about the spacecraft and test mass alignment.
- A sine and cosine look-up table (LUT) in order to generate the sine and cosine waves for the mixing.

As explained in Section 1.6.1, the laser of the transponder spacecraft is locked to the master spacecraft laser. A frequency offset f_offset is used in this laser lock loop, so that zero-crossings are avoided when the Doppler shift changes signs. Additionally, having

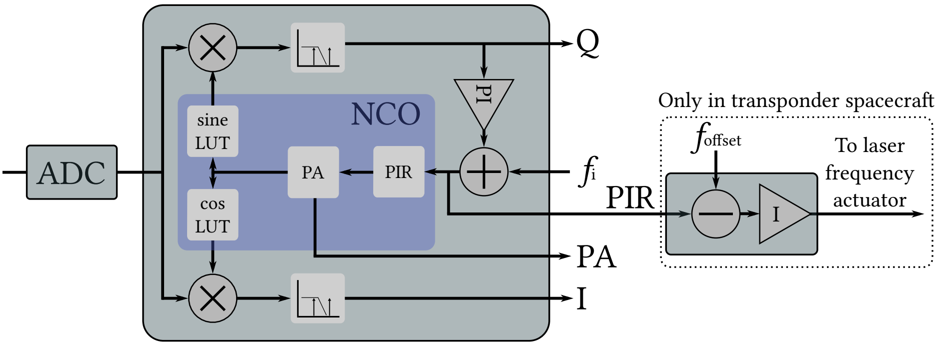

Figure 1.10: Block diagram of the phasemeter ADPLL. The digitized signal from the ADC is mixed with a sine wave from an NCO. A low-pass filter removes the high frequency component of the mix, leaving the quadrature component (Q). Q is processed first by a PI controller. The output for the PI controller feeds the NCO, which is a combination of the phase increment register (PIR), the phase accumulator (PA) and the look-up tables (LUTs). The PIR contains the instantaneous frequency and the PA the instantaneous phase. The ADPLL also provides the In-phase component (I) which represents the instantaneous amplitude. The instantaneous frequency from the PIR is used at the transponder spacecraft to lock the local laser to the incoming beam.

a beat-note above ~ 5 MHz mitigates the effect of relative intensity noise (RIN) in non-planar ring oscillator (NPRO) lasers [44, p. 75]. In LISA, the offset frequency needs to be switched regularly to keep the beat-note within a feasible operating range. This is called the frequency plan [44, p. 80]. In the case of GRACE-FO, the offset frequency is fixed at 10 MHz.

The ADPLL also mixes the input signal with a cosine wave of the same frequency and phase. The result of this mixing after filtering is the In-phase component of the signal (I), which represents the instantaneous amplitude.

The phasemeter also performs a set of auxiliary functions which are not directly related to the phase extraction of the main science signal, but are also needed for the metrology chain to operate. The following auxiliary functions are implemented in the phasemeter:

- Beat-note acquisition for automatic lock of the frequency. This is a necessary step prior to science measurements. The function is based on a Fast Fourier Transform (FFT) and a peak finding algorithm.

- Active measurement of the absolute distance between any two spacecraft to suppress laser frequency noise via time-delay interferometry (TDI) [45]. The measurement is based on a pseudo random noise (PRN) modulation of the outgoing laser beams.

- Data transfer for direct laser communication between spacecraft.

1.6.4 Noise budget and photoreceiver requirements

Any practical metrology system is ultimately limited by noise. In a general sense, noise can be described as any contribution to the measurement that does not originate from the physical property to be measured. A complex system such an intersatellite laser interferometer for precision displacement measurements is not an exception, with a long list of potential noise sources in the different subsystems or linked to external factors.

Figure 1.11 shows the LISA strain sensitivity for a 3-arm configuration as shown in the L3 proposal [9, p. 6]. The strain sensitivity ultimately defines the capability of the detector to observe gravitational waves. Some types of gravitational wave sources in the LISA frequency band are plotted as well.

Advanced LIGO presents a strain sensitivity of $1 \times 10^{-23}\,\mathrm{Hz}^{-1/2}$ at 100 Hz, orders of magnitude better than LISA. This apparent lack of sensitivity is compensated by the stronger astrophysical sources in the LISA frequency band, from 0.1 mHz to 100 mHz. These sources include massive black hole binaries, extreme mass ratio inspirals and several of thousand of galactic binaries [9, p. 6].

The final strain sensitivity of the interferometer S_h is mainly defined by three parameters: the total displacement noise $\tilde{x}$, the arm length of the Michelson interferometer L_arm and the response function to gravitational waves (RFGW).

$$S_h(\tilde{x}, L_\mathrm{arm}, \mathrm{RFGW}) \tag{1.8}$$

- The displacement noise $\tilde{x}$ determines the precision of relative distance measurements in the interferometer. The displacement noise $\tilde{x}$ can originate from noise sources which mimic distance changes between the test masses, namely readout noise, or from unwanted stray acceleration of the test masses themselves. The displacement noise is indistinguishable from actual displacements produced by gravitational waves or gravity field variations. A detailed description of the different contributions in LISA can be found in [46]. The photoreceiver also contributes to $\tilde{x}$. This thesis focuses on understanding and minimizing that contribution.

- The arm length L_arm represents the absolute distance between the test masses in the long arm of the interferometer. It divides $\tilde{x}$ to define the effective strain sensitivity of the interferometer measuring distance changes. In a simple model not including RFGW, increasing L_arm while maintaining $\tilde{x}$ constant improves the strain sensitivity of the observatory.

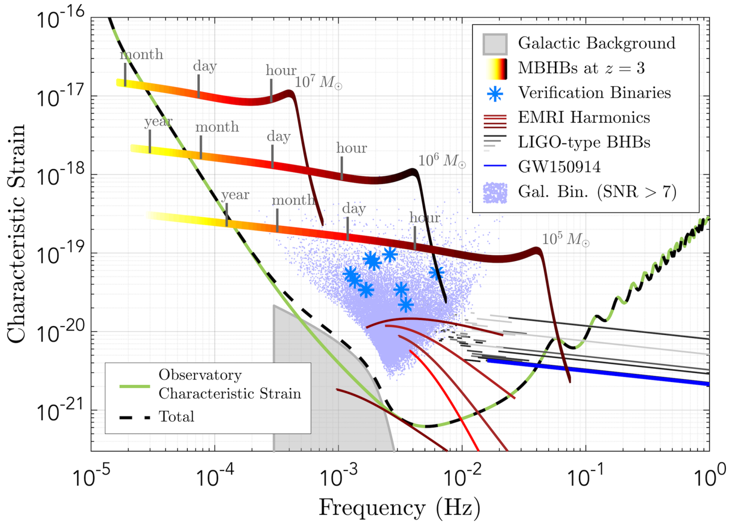

Figure 1.11: Strain sensitivity of the LISA mission for a 3-arm configuration and detectable astrophysical sources in the LISA band. The strain sensitivity represents the capability of the observatory to detect gravitational waves. The strain sensitivity is mainly defined by the interferometer displacement noise, the arm length and the response to gravitational waves [9].

- The RFGW depends on the arm length to gravitational-wave wavelength ratio. For low frequencies, the wavelength of the gravitational wave is long enough compared to L_{arm} and the resulting RFGW is flat. At high frequencies, when the wavelength is equal or smaller than L_{arm}, the gravitational wave oscillation partially cancels out, reducing the effective strain sensitivity of the observatory. Additionally, the non-stationary behavior of the LISA configuration (constellation breathing, rotations) modulates the RFGW, producing ripples in the strain sensitivity at high frequencies. The strain sensitivity of LISA also depends on the propagation direction of the incoming gravitational wave. The antenna pattern of LISA produces blind spots where the strain sensitivity of the observatory is degraded [44, p. 55].

For the expected strain sensitivity in LISA, shown in Figure 1.11, the performance is limited below 3 mHz due to test mass residual acceleration noise, which was experimentally measured in LPF to levels down to $5.2\,\text{fm}\,\text{s}^{-2}\,\text{Hz}^{-1/2}$ [11]. Above 3 mHz, the observatory sensitivity is mainly limited by the long-arm interferometer readout noise. Even if the readout noise is flat over frequency, the effect of the RFGW becomes important at frequencies above 10 mHz, degrading the strain sensitivity at about one order

Table 1.1: Breakdown of the optical metrology chain displacement noise, showing the photoreceiver contribution. The values shown are current best estimates at frequencies above ~ 3 mHz [46]. The value of a given row contributes to the combined noise of the row above.

	Instrument subsystem	$\mathrm{pm\,Hz^{-1/2}}$
Breakdown ↓	Total noise	7.7
	Long-arm interferometer	5.2
	Photoreceiver	2.2

of magnitude per decade.

Table 1.1 is a breakdown of the optical metrology chain displacement noise $\tilde{x}$, from the total noise down to the photoreceiver electronic noise contribution. The value in a given row contributes to the combined noise of the row above. For instance, the displacement noise $\tilde{x}_{\mathrm{en}}$ ($2.2\,\mathrm{pm\,Hz^{-1/2}}$) generated by photoreceiver electronic noise contributes to the long-arm interferometer noise ($5.2\,\mathrm{pm\,Hz^{-1/2}}$), which is mainly dominated by shot noise. These values are directly extracted from the last LISA performance model and error budget [46]. The noise contributions in [46] are current best estimates. Ideally, the contribution of the photoreceiver should be smaller, to the point at which shot noise is the only significant contribution to the long-arm interferometer readout noise. The detailed description of other noise contributions, laser frequency noise reduction via TDI or the way they combine with $\mathrm{L_{arm}}$ and RFGW to obtain the final strain sensitivity is out of the scope of this thesis. A comprehensive description of the sensitivity calculation can be found in [46].

Since the metrology system tracks variations in the phase of the beat-note produced by length displacements of the test masses, the phase noise ($\tilde{\phi}$) is commonly used to describe the noise budget. Equation 1.9 shows the relationship between displacement noise and phase noise.

$$\begin{aligned} \tilde{\phi} &= \frac{2\pi\tilde{x}}{\lambda}, \\ [\tilde{\phi}] &= \mathrm{rad\,Hz^{-1/2}}. \end{aligned} \tag{1.9}$$

with λ being the wavelength of the light source used (1064 nm). According to Equation 1.9 and assuming a noise contribution of $5.2\,\mathrm{pm\,Hz^{-1/2}}$ for the readout chain of the long-arm interferometer, the equivalent phase noise contribution is about $30\,\mathrm{\mu rad\,Hz^{-1/2}}$. The requirement for the long-arm interferometer phase noise is relaxed towards low frequencies, since the acceleration noise of the test mass limits in any case the sensitivity of the interferometer [46].

In the following, the noise sources related to the photoreceiver that contribute to the overall phase noise will be discussed. This analysis was part of an article published in Optics Express [47]. The carrier-to-noise-density of the system ($\mathrm{C/N_0}$), common in satellite communications, can be used to analyze different noise contributions in a photoreceiver like the one described in Section 1.6.2. The concept is similar to the signal-to-noise ratio (SNR), also used in photodetector designs [48, p. 61]. On the other hand, the carrier-to-noise density ($\mathrm{C/N_0}$), which is a function of frequency, contains more information about the signals spectra. The inverse of $\mathrm{C/N_0}$ directly provides the noise spectral density of the readout chain in terms of phase [19], which can be used as a figure of merit for the total photoreceiver noise contribution. This simple conversion occurs because noise (e.g. amplitude fluctuations) at the optical beat-note frequency is converted into phase noise by the phasemeter, making it indistinguishable from the actual phase of the beat-note. The following noise analysis focuses first on a single channel of the photoreceiver. In the last part of the section, the total photoreceiver noise including all channels and photoreceiver units involved is given. The beat-note signal (carrier), which corresponds to the AC part of Equation 1.7, has a root mean square (RMS) value after photo-conversion given by Equation 1.10.

$$\begin{aligned} i_{\mathrm{bn}}^{\mathrm{s}} &= R(2\gamma P_{\mathrm{LO}}^{\mathrm{s}} P_{\mathrm{RX}}^{\mathrm{s}})^{1/2}, \\ [i] &= \mathrm{A}, \end{aligned} \tag{1.10}$$

where R is the responsivity of the photodetector given in $\mathrm{A\,W^{-1}}$ (details in Section 2.1.1), γ is the heterodyne efficiency of the interferometer, which describes how the two interfered beams overlap, and $P_{\mathrm{LO}}^{\mathrm{s}}$ and $P_{\mathrm{RX}}^{\mathrm{s}}$ are the optical powers of the two interfered beams on a photodetector segment. P_{LO} corresponds to the power of the local laser and P_{RX} to the power of the received beam from the distant spacecraft.

The first noise contribution presented is shot noise. Shot noise does not originate in the photoreceiver but it is intrinsic to the photodetection process and ultimately dominates the long-arm interferometer performance above 2 mHz assuming standard mission parameters. The amplitude spectral density of shot noise is given by Equation 1.11 [49, p. 45].

$$\begin{aligned} \tilde{i}_{\mathrm{sn}}^{\mathrm{s}} &= (2qR(P_{\mathrm{LO}}^{\mathrm{s}} + P_{\mathrm{RX}}^{\mathrm{s}}))^{1/2}, \\ [\tilde{i}] &= \mathrm{A\,Hz^{-1/2}}, \end{aligned} \tag{1.11}$$

with q being the charge of an electron. Now, we use the inverse of the $\mathrm{C/N_0}$ to obtain the phase noise density contribution of shot noise [19, p. 45].

$$\tilde{\phi}_{\mathrm{sn}}^{\mathrm{s}} = \frac{\tilde{i}_{\mathrm{sn}}^{\mathrm{s}}}{i_{\mathrm{bn}}^{\mathrm{s}}} = \left(\frac{q(P_{\mathrm{LO}}^{\mathrm{s}} + P_{\mathrm{RX}}^{\mathrm{s}})}{R\gamma P_{\mathrm{LO}}^{\mathrm{s}} P_{\mathrm{RX}}^{\mathrm{s}}}\right)^{1/2}. \tag{1.12}$$

A simplification of Equation 1.12 is commonly used. Assuming $P_{\mathrm{LO}}^{\mathrm{s}}$ is much greater than $P_{\mathrm{RX}}^{\mathrm{s}}$, $\tilde{\phi}_{\mathrm{sn}}^{\mathrm{s}}$ can be described by Equation 1.13.

$$\tilde{\phi}^{\mathrm{s}}_{\mathrm{sn}} = \frac{\tilde{\imath}^{\,\mathrm{s}}_{\mathrm{sn}}}{i^{\,\mathrm{s}}_{\mathrm{bn}}} \approx \left(\frac{q}{R\gamma P^{\mathrm{s}}_{\mathrm{RX}}}\right)^{1/2}. \tag{1.13}$$

Equation 1.13 reveals that the shot noise contribution to phase noise is limited by the power of the received beam if this beam is much weaker than the local beam. Additionally, even if shot noise is not produced at the photoreceiver, the responsivity of the photodetection device R affects the shot noise contribution to phase noise.

In a similar fashion, we can calculate the contribution of electronic noise (resistors Johnson-Nyquist noise, operational amplifier (OpAmp) noise...). This noise $\tilde{\imath}_{\mathrm{en}}$ is usually referred to the input of the photoreceiver and is given directly in $\mathrm{A\,Hz^{-1/2}}$. A detailed description of the electronic noise in a photoreceiver can be found in Section 2.2.1. It is important to remark that $\tilde{\imath}_{\mathrm{en}}$ refers to electronic noise in the MHz band, which produces amplitude fluctuations at the beat-note frequency. Even though $\tilde{\imath}_{\mathrm{en}}$ is in general flat in the kHz regime, it increases towards high frequencies in the MHz range. When a single value of $\tilde{\imath}_{\mathrm{en}}$ is given, it refers to the worst-case scenario: its value at the highest heterodyne frequency. In this analysis we do not take into account upconversion of low frequency phasemeter or photoreceiver electronic noise into the MHz band. The phase noise contribution of the photoreceiver electronic noise is given by Equation 1.14 [44, p. 41].

$$\tilde{\phi}^{\mathrm{s}}_{\mathrm{en}} = \frac{\tilde{\imath}^{\,\mathrm{s}}_{\mathrm{en}}}{i^{\,\mathrm{s}}_{\mathrm{bn}}} = \frac{\tilde{\imath}^{\,\mathrm{s}}_{\mathrm{en}}}{R(2\gamma P^{\mathrm{s}}_{\mathrm{LO}} P^{\mathrm{s}}_{\mathrm{RX}})^{1/2}}. \tag{1.14}$$

The following two noise sources are less common in the literature. A previous analysis of their effects on the phasemeter can be found in [49]. The first one is the thermally induced phase noise in the photoreceiver. Temperature variations in the spacecraft area where the photoreceiver is located produce changes in the phase response of the photoreceiver, inducing noise. An AAF located in the photoreceiver would be particularly susceptible to phase fluctuations over temperature due to its typically steep frequency response. Thanks to temperature simulations, we can anticipate the temperature stability in the spacecraft, a factor $\tilde{T}_{\mathrm{PR}}$ given in $\mathrm{K\,Hz^{-1/2}}$. The dependency of the main beat-note phase on temperature can be measured experimentally, obtaining a coefficient ϕ_{LT} given in $\mathrm{rad\,K^{-1}}$. This coefficient could, in general, be a function of the absolute temperature, but experimental results from photoreceiver characterization (Section 3.4.3) showed a mostly linear relationship between phase and temperature for a given frequency. This means that the coefficient is constant at least for the temperature range used. The thermally induced phase noise contribution in the photoreceiver can then be obtained using Equation 1.15.

$$\tilde{\phi}^{\mathrm{s}}_{\mathrm{tin}} = \tilde{T}^{\mathrm{s}}_{\mathrm{PR}} \phi^{\mathrm{s}}_{\mathrm{LT}}. \tag{1.15}$$

The last noise source of this analysis comes from the finite phase response of the photoreceiver. Operating in the MHz range, the photoreceiver phase response over frequency is not flat, having a coefficient ϕ_{LF} given in rad Hz^{-1}. The coefficient ϕ_{LF} is in general frequency-dependent, but it can be approximated to a constant in a narrow frequency range. Changes in the frequency of the beat-note would couple as phase variations in the system. The lasers used in intersatellite interferometry, like any other laser source, present a frequency noise $\tilde{f}_{\mathrm{laser}}$, given in Hz Hz$^{-1/2}$, which produces phase noise due to the finite phase response of the photoreceiver. Additionally, the dynamics of the beat-note frequency due to relative spacecraft motion, with an amplitude spectral density $\tilde{f}_{\mathrm{Doppler}}$ given also in Hz Hz$^{-1/2}$, also couple as phase variations via the finite phase response. This $\tilde{f}_{\mathrm{Doppler}}$ can be estimated from the spectral density of the relative velocity between the satellites [10]. Expression 1.16 shows the total contribution due to the finite phase response of the photoreceiver.

$$\tilde{\phi}^{\mathrm{s}}_{\mathrm{fpn}} = (\tilde{f}^{\,2}_{\mathrm{laser}} + \tilde{f}^{\,2}_{\mathrm{Doppler}})^{1/2}\phi^{\mathrm{s}}_{\mathrm{LF}}. \tag{1.16}$$

A difference between $\tilde{\phi}^{\mathrm{s}}_{\mathrm{fpn}}$ and the rest of noise sources in the photoreceiver is that post-processing methods can be used to mitigate the effect of this noise contribution. Strictly speaking, $\tilde{f}_{\mathrm{Doppler}}$ is not a purely stochastic component of the phase noise density, since it can be tracked and corrected. Additionally, assuming $\phi^{\mathrm{s}}_{\mathrm{LF}}$ is carefully measured, it can be used to calibrate the readout chain and reduce $\tilde{\phi}^{\mathrm{s}}_{\mathrm{fpn}}$. For this reason, this noise contribution is not included in the following calculation of the photoreceiver noise budget. Assuming that the other three contributions to phase noise are uncorrelated, the total phase noise in a photoreceiver segment is given by Equation 1.17.

$$\tilde{\phi}^{\mathrm{s}}_{\mathrm{T}} = \left(\tilde{\phi}^{\mathrm{s}\ 2}_{\mathrm{sn}} + \tilde{\phi}^{\mathrm{s}\ 2}_{\mathrm{en}} + \tilde{\phi}^{\mathrm{s}\ 2}_{\mathrm{tin}}\right)^{1/2}. \tag{1.17}$$

Equation 1.17 provides the noise of a single channel or from a single-element photoreceiver. The actual phase noise of the photoreceiver in the readout chain also depends on:

- The segmented nature of the photodetector: The photoreceiver features quadrant photodiodes with four different phase signals provided by a single device.
- More than one photoreceiver is used to read out the same interferometric signal. In general, two independent photoreceivers measure the two outputs of the recombining beam splitter used to interfere the optical signals. The beams contain the same information, shifted in phase by π rad. Balanced detection benefits from this by using the two available signals to cancel out the laser relative intensity noise (RIN). Additionally, the current LISA scheme includes a copy of the photoreceiver pair in each interferometer to provide the system with redundancy, which prevents the loss of balanced detection if a photoreceiver fails.

The combination of the signals in the current design of the LISA long-arm interferometer can be seen in Figure 1.12. A total of 16 photoreceiver channels provide phase

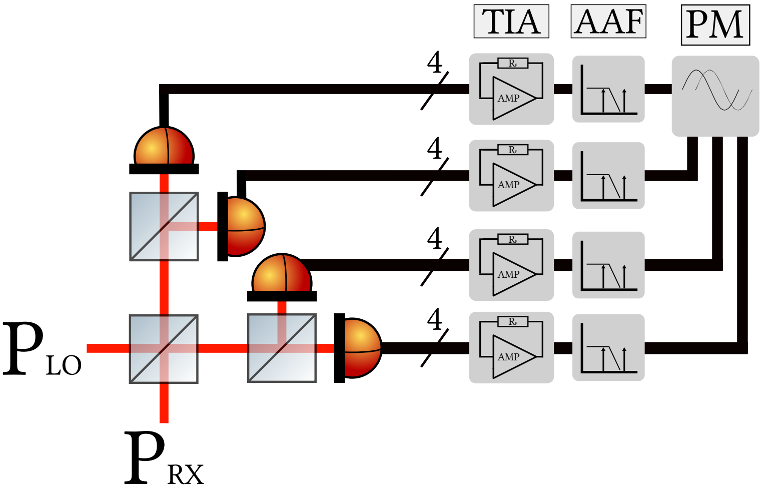

Figure 1.12: Block diagram of the full readout chain in the current LISA long-arm interferometer design. The two outputs of the recombining beam splitter are used to maximize the SNR, provide redundancy and reduce RIN via balanced detection. LISA includes a copy of the photoreceiver pair in each interferometer to provide extra redundancy. A total of 16 photoreceiver channels provide information about the longitudinal displacements (mean phase) or angular misalignment (differential phase).

signals which are averaged to obtain the mean longitudinal phase signal. The interesting figure of merit is the phase noise $\tilde{\phi}_\mathrm{T}$ of the combined signal. We can assume that shot noise and electronic noise are incoherent in the different channels and thermally induced noise, in the worst-case scenario, is not. The total noise contributions after averaging the 16 channels is given by Equations 1.18, 1.19 and 1.20.

$$\tilde{\phi}_\mathrm{sn} = \frac{1}{16}\left(\sum_{s=1}^{16}\tilde{\phi}_\mathrm{sn}^{\mathrm{s}\;2}\right)^{1/2} = \frac{16^{1/2}}{16}\left(\frac{q(P^\mathrm{s}_\mathrm{LO}+P^\mathrm{s}_\mathrm{RX})}{R\gamma P^\mathrm{s}_\mathrm{LO}P^\mathrm{s}_\mathrm{RX}}\right)^{1/2} = \left(\frac{q(P_\mathrm{LO}+P_\mathrm{RX})}{R\gamma P_\mathrm{LO}P_\mathrm{RX}}\right)^{1/2}. \tag{1.18}$$

$$\tilde{\phi}_\mathrm{en} = \frac{1}{16}\left(\sum_{s=1}^{16}\tilde{\phi}_\mathrm{en}^{\mathrm{s}\;2}\right)^{1/2} = \frac{16^{1/2}}{16}\,\frac{\tilde{\imath}^\mathrm{s}_\mathrm{en}}{R(2\gamma P^\mathrm{s}_\mathrm{LO}P^\mathrm{s}_\mathrm{RX})^{1/2}} = \frac{16^{1/2}\,\tilde{\imath}^\mathrm{s}_\mathrm{en}}{R(2\gamma P_\mathrm{LO}P_\mathrm{RX})^{1/2}}. \tag{1.19}$$

$$\tilde{\phi}_\mathrm{tin} = \frac{1}{16}\sum_{s=1}^{16}\tilde{\phi}^\mathrm{s}_\mathrm{tin} = \tilde{\phi}^\mathrm{s}_\mathrm{tin}. \tag{1.20}$$

The equations above assume that all factors (R,γ...) are the same in all 16 segments. The total phase noise is given then by Equation 1.21.

$$\tilde{\phi}_{\mathrm{T}} = \left(\tilde{\phi}^2_{\mathrm{sn}} + \tilde{\phi}^2_{\mathrm{en}} + \tilde{\phi}^2_{\mathrm{tin}}\right)^{1/2} . \tag{1.21}$$

Figure 1.13 shows the phase noise budget for the photoreceiver, obtained using the expected long-arm interferometer parameters from the last LISA performance model and error budget [46]. The parameters used are summarized in Table 1.2. The red curve represents the allocated phase noise for the long-arm interferometer readout. As mentioned above, this noise goal is relaxed towards low frequencies, where the displacement noise is dominated by test mass acceleration noise. The purple line represents $\tilde{\phi}_{\mathrm{T}}$, which is dominated by shot noise above 2 mHz, with the photoreceiver electronic noise as second major contribution. Below 2 mHz, the thermally induced phase noise dominates, but lies below the relaxed readout noise goal at all frequencies.

Table 1.2: Long-arm interferometer parameters in LISA [46] used to calculate the phase noise contributions of Figure 1.13. T_{PR} shows only the noise floor at 1 Hz for simplification. In reality, it increases towards low frequencies as seen in Figure 1.13.

Local laser power	P_{LO}	2.9	mW
Received power	P_{RX}	510	pW
Photodiode responsivity	R	0.7	$\mathrm{A\,W^{-1}}$
Heterodyne efficiency	γ	0.8	1
Photoreceiver electronic noise	$\tilde{i}_{\mathrm{en}}$	3.5	$\mathrm{pA\,Hz^{-1/2}}$
Temperature stability	T_{PR}	10^{-3}*	$\mathrm{K\,Hz^{-1/2}}$
Longitudinal phase temperature coefficient	ϕ_{LT}	5×10^{-3}	$\mathrm{rad\,K^{-1}}$

The noise analysis of this section does not consider the RIN in the interferometer, assumed to be negligible due to balanced detection or a sufficiently low local oscillator optical power P_{LO} [44, p. 41]. The following list summarizes the main photoreceiver requirements:

- The long-arm interferometer must be shot-noise-limited above $\sim$ 1 mHz, which means that the photoreceiver must have a minor contribution in the readout noise compared to shot noise. The LISA performance model and error budget [46] assigns 2.2 $\mathrm{pm\,Hz^{-1/2}}$ (or 13 $\mathrm{\mu rad\,Hz^{-1/2}}$ in terms of phase noise) to the current best estimate for the photoreceiver electronic noise contribution, but a lower value is desired. The photodetector responsivity R should be at least 0.7 $\mathrm{A\,W^{-1}}$ at the required wavelength. In terms of electronic noise, the nominal value is $\tilde{i}_{\mathrm{en}}$ = 3.5 $\mathrm{pA\,Hz^{-1/2}}$, although currently some photoreceiver candidates present lower

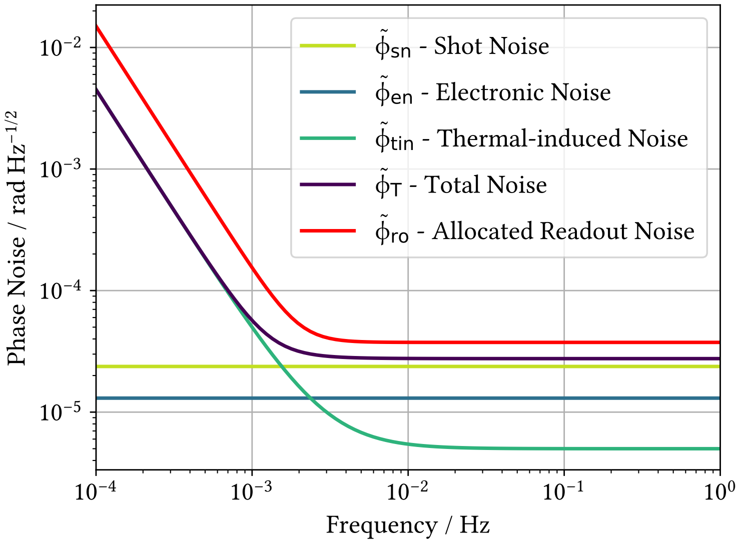

Figure 1.13: Phase noise budget for a LISA photoreceiver. The conditions of the interferometer are summarized in Table 1.2. The red curve represents the allocated phase noise for the long-arm interferometer. The purple line represents the combined noise $\tilde{\phi}_{\mathrm{T}}$, which is dominated by shot noise above 2 mHz, with the photoreceiver electronic noise as second major contribution. Below 2 mHz, the thermally induced phase noise dominates, but lies below the relaxed readout noise goal.

electronic noise contributions. A detailed analysis of $\tilde{\imath}_{\mathrm{en}}$ can be found in Section 2.2.1, with experimentally measured values shown in Sections 3.4.2 and 3.5.

- The bandwidth of the photoreceiver must cover the heterodyne frequency range of the mission. For LISA, the maximum expected heterodyne frequency is 25 MHz. This implies that the requirement for the photoreceiver electronic noise $\tilde{\imath}_{\mathrm{en}}$ must be fulfilled also at 25 MHz.
- The photoreceiver must be DC-coupled to provide a path for the DC component of the photocurrent (Equation 1.6). Section 2.2.2 analyzes the two potential solutions for a DC-coupled photoreceiver.
- For LISA, the photoreceiver power consumption is a concern due to the high number of photodetection devices in a single spacecraft. The last power budget allocates 500 mW per photoreceiver, including the TIA electronics.

2 Photoreceiver solutions

This chapter presents a discussion of photoreceiver solutions to find the optimal approach for intersatellite laser interferometers. The chapter is divided into two main sections. Section 2.1 focuses on the photodetector, discussing the possibilities of traditional, present and future technologies detecting infrared light. Section 2.2 concentrates on the TIA, presenting topologies available and also theoretical estimations of important photoreceiver parameters such as noise, bandwidth and power consumption.

2.1 The photodetector

The gradual discovery of photodetection mechanisms over the last two centuries, briefly discussed in Section 1.5, turned into a wide variety of practical photodetector solutions. Not every photodetector available today covers the particular demands of a photoreceiver for intersatellite laser interferometry. In practice, only one technology fulfills all requirements: semiconductor-based photodiodes. This section also presents other photodetector types, showing that they lack fundamental properties needed in optical metrology systems like LISA or the LRI.

The type of light used in the interferometer plays an important role in defining the photodetector. NPRO lasers are used in precision metrology due to their extensively tested frequency stability. The laser frequency stability, also known as linewidth, can limit the precision of measuring length variations [44, p. 52]. With the right locking scheme, linewidths of a few kHz can be achieved [50]. NPROs are typically based on a single Nd:YAG (Neodymium-doped Yttrium aluminum garnet) laser crystal with an operating wavelength of 1064 nm, in the near-infrared range. NPRO lasers have been successfully used in LIGO [51] and in LPF [52]. GRACE-FO also features an NPRO laser [17], and such a device also constitutes the baseline for LISA's light source [9]. For this reason, a photodetector candidate for intersatellite laser interferometers needs to be responsive at 1064 nm. Equations 1.12 and 1.14 show how the responsivity of the detector R affects the photoreceiver noise budget, whereby decreasing the responsivity leads to an increase in phase noise. Additionally, since the photoreceiver needs to handle AC beat-notes of up to 25 MHz in the case of LISA (see Section 1.6.1), the photodetector must be able to detect changes of optical power in that frequency range as well. In terms of detector structure, the DWS technique used in intersatellite laser interferometers (Section 1.6.2) requires photodetectors with at least 4 segments. With a segmented structure it is possible to measure the angular misalignment between the interfered beams.

Thermal detectors are historically the first devices used to detect infrared wavelength. Devices based on the Seebeck effect [53] are in general imprecise, being able to detect changes in the incoming infrared radiation of only a few percent. Additionally, they cannot detect quick variations of the incident light and are limited to speeds of $\sim 100\,\mathrm{Hz} - 1\,\mathrm{kHz}$.

Phototubes or photomultipliers replaced previous solutions for near-infrared detection. The precision achieved with this relatively old technology is remarkable. Photomultipliers can still be found in photon-counting experiments [54]. On the other hand, their bulky structure and the very high bias voltage needed, of the order of 100 V, render them a poor choice for photodetectors aimed at space applications.

The boom of semiconductor devices in the second half of the 20th century had a direct impact on photodetection in the infrared range. An advantage of semiconductor-based photodetectors is the possibility to optimize the responsivity R at different wavelengths by alloying multiple compounds. A ternary alloy formed by indium, gallium and arsenic (InGaAs) has been well developed since the 1960s, presenting high R values for near-infrared wavelengths like 1064 nm [55]. The speeds achieved with InGaAs semiconductor-based detectors are sufficient for heterodyne interferometry applications in the MHz domain. The speed depends on material properties (like carrier mobility) and structure, therefore it can also be optimized with different compounds and design techniques.

Table 2.1 summarizes the characteristics of the different photodetector technologies from the perspective of the requirements in an intersatellite laser interferometer.

Table 2.1: Photodetection technology comparison

	R @ 1064 nm	Speed	Segmented	Bias Voltage
Thermal detectors	✗	✗	✗	✓
Phototubes	✓	✓	✗	✗
Semiconductor-based	✓	✓	✓	✓

2.1.1 Photodiode physics

The revolution in computing that occurred during the second half of the 20th century can be attributed to the invention of the integrated circuit (IC) in the late 1950s. Reaching this milestone would not have been possible without the extensive research on semiconductor materials in the first half of the century. In essence, a semiconductor is a device whose electrical properties change with temperature. Above absolute zero there is a finite probability for an electron to be in the conduction band (free electron) and this probability increases with temperature [56, p. 5]. When a voltage is applied across the semiconductor, the free electrons in the conduction band and hole vacancies in the valence band can contribute to the current flowing through the device. The initial conductivity of the semiconductor can be increased by introducing donor dopants, obtaining an n-type semiconductor with an excess of free electrons. In a similar fashion, an acceptor dopant increases the conductivity creating an excess of hole vacancies, obtaining a p-type semiconductor. The union of a p-type and an n-type of semiconductor, known as p-n junction, represents the building block of all solid-state electronics. A p-n junction allows the construction of diodes and transistors with which electrical magnitudes can be controlled electrically [57].

The creation of free electron-hole pairs in semiconductor devices is not only produced by temperature. As described in Section 1.5, sufficiently energetic light radiation (i.e. with an energy greater than the semiconductor band gap) can create carrier pairs in a semiconductor device via the internal photo-electric effect [56, p. 11]. Semiconductor-based photodetectors benefited from the development of p-n junctions, since light absorption improves in such devices. Light penetrates into the junction and is absorbed in the depletion region between the two sections. The built-in electric field sweeps the generated electron-hole pairs towards the external contacts before they recombine. An external reverse-biased voltage can be applied to magnify the effect of the built-in electric field.

Ideally, all carriers should be generated in the depletion region. Wider depletion regions translate into greater absorption coefficients (i.e. greater responsivity). That is the basis of PIN photodiodes, in which an additional layer of intrinsic semiconductor is used in order to increase the absorption area [58, p. 260]. Moreover, the increment of the depletion layer width also reduces the junction capacitance, which directly affects the speed of the device (see Section 2.2.1). The depletion region, or spatial charge region, is essentially a planar capacitor due to the charge distribution between the p-type and the n-type semiconductors after reaching equilibrium. By introducing a layer of intrinsic material in between, the effective capacitance decreases. The size of this intrinsic region should not exceed a certain limit, from which the speed of the device decreases due to longer carrier transit time.

The semiconductor materials have a direct impact on the responsivity of the device. The main two mechanisms that define the responsivity for a given material are:

- The energy band gap (E_g). The wider this band gap is, the higher the energy needed to generate carriers. Higher energies are equivalent to higher frequencies or shorter wavelengths.
- The type of band gap. Light impinging on an indirect band gap material can

penetrate farther without being absorbed compared to a direct band gap material [59]. Additionally, the absorption spectrum of indirect band gap materials is more dependent on the material temperature.

The first material used for photodiodes was germanium, which was quickly replaced by silicon since the latter presented better performance in terms of dark current (wider band gap) and higher responsivity at shorter wavelengths [60, p. 129]. Silicon also became predominant in the sector of photovoltaics (solar cells) for its trade-off of absorption efficiency and cost. As mentioned in Section 2.1, an advantage of semiconductor devices is the possibility of changing the properties by alloying more complex materials. Detection in the 1000 nm to 1500 nm wavelength range improved significantly thanks to the indium gallium arsenide (InGaAs) ternary alloy. Figure 2.1 shows the responsivity R of photodiodes based on the three different semiconductor materials discussed. The InGaAs-based device has the highest R at the working wavelength (1.064 µm). Additionally, the fundamental limit given by the quantum efficiency QE is also plotted. Equation 2.1 shows the relation between R, QE and λ [61, p. 4].

$$\begin{aligned} R &= QE\frac{q\lambda}{hc}, \\ [R] &= \mathrm{A\,W^{-1}}, \end{aligned} \tag{2.1}$$

with h being Planck's constant, q the elementary charge and c the speed of light.

The major drawback of InGaAs-based photodiodes is the greater junction capacitance for a given detector area compared to other materials. The junction capacitance of a photodiode is described by Equation 2.2 [61, p. 3]

$$\begin{aligned} C_\mathrm{j} &= \frac{\epsilon A}{w}, \\ [C_\mathrm{j}] &= \mathrm{F}, \end{aligned} \tag{2.2}$$

where C_j is the junction capacitance, ϵ is the absolute permittivity of the material, A is the detector area and w is the width of the depletion region. The permittivity in InGaAs is higher than in silicon. The junction capacitance of the photodiode, as explained later in Section 2.2.1, has a direct impact on the photoreceiver noise and bandwidth. The photodiode manufacturer Discovery Semiconductors Inc developed an InGaAs-based segmented photodiode with an extended intrinsic region, consequently increasing w. The photodiode presented a junction capacitance of 2.4 pF per segment in a 4-segment, 1 mm diameter device [65]. An equivalent silicon-based photodiode would present a junction capacitance of around 1.2 pF, using standard material parameters.

The baseline for intersatellite laser interferometers is to use InGaAs photodiodes as photodetectors. Their higher absorption at the required wavelength (1064 nm) compensates for the side effects of having a higher capacitance. Additionally, lower-capacitance

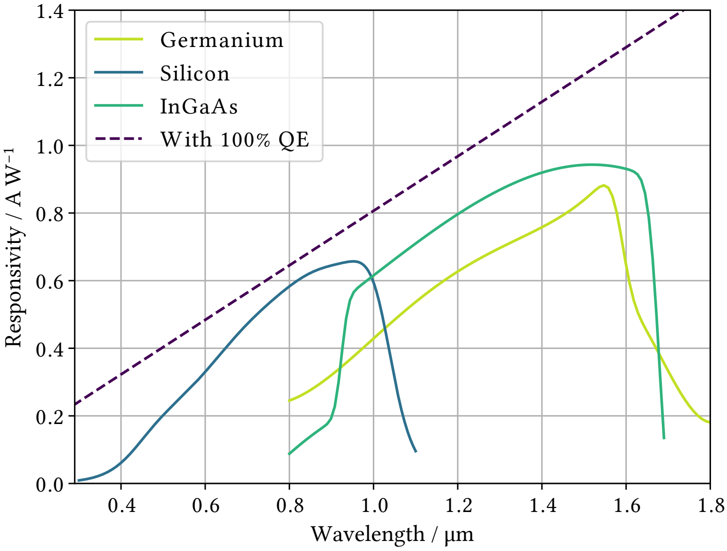

Figure 2.1: Responsivity R over wavelength for a typical photodiode based on germanium [62], silicon [63] and InGaAs [64]. The InGaAs-based device has the highest R at the working wavelength (1.064 µm). The responsivity for an ideal quantum efficiency QE (Equation 2.1) is also plotted.

InGaAs devices such as the Discovery Semiconductor model are available. Bootstrapping, a technique commonly employed to reduce the effect of C_j in photodetectors [66], cannot be easily applied to segmented photodiodes due to their common cathode configuration.

It is very useful in photoreceiver design to replace the photodiode by its electrical model. A simple model, sufficiently accurate for the calculations and simulations of this thesis, is shown in Figure 2.2. The current source represents the photocurrent generated by the device, which is in parallel with the junction capacitance C_j. A more complex model, in agreement with an experimental characterization of the photodiode frequency response up to 10 GHz, can be found in [67]. The equivalent circuit shown in [68, p. 79] was used to improve fits of the experimentally measured photodiode impedance.

2.1.2 Avalanche photodiodes

Avalanche photodiodes (APDs) are a particular type of detectors that show an internal gain when high reverse bias voltages are applied. This internal gain is produced by

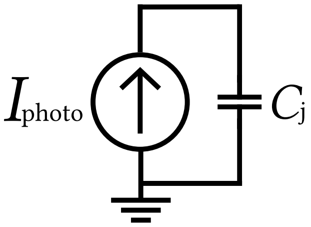

Figure 2.2: Simple electrical model of a photodiode. The current source represents the generated photocurrent, which is in parallel with the junction capacitance C_j.

the avalanche effect. When a free electron is accelerated by a very high electric field within the semiconductor device, it can transfer momentum to electrons of the valence band, potentially creating new electron-hole pairs. They newly created carriers will subsequently continue the process, resembling an avalanche. The high electric field needed to sufficiently accelerate the electrons exists in an additional thin, highly doped layer.

From the perspective of the generated photocurrent and noise, APDs present two additional coefficients that do not exist in the PIN diodes from the previous section. The first one obviously is the increase of the generated photocurrent for a given amount of optical power. An additional factor M representing the internal gain multiplies the photocurrent. The RMS value of the beat-note would then be described by Equation 2.3 [69, p. 1].

$$i_\text{bn} = MR(2\gamma P_\text{LO} P_\text{RX})^{1/2}. \tag{2.3}$$

The internal gain M also needs to be taken into account for the calculation of shot noise, together with a factor called excess noise (F), which arises from higher statistical noise due to the multiplication process. The shot noise in an APD is given by Equation 2.4 [69, p. 3].

$$\tilde{\imath}_\text{sn} = (2qRM^2F(P_\text{LO} + P_\text{RX}))^{1/2}. \tag{2.4}$$

If we now express the shot noise contribution in terms of phase noise as shown in Equation 1.12, the result is given by Equation 2.5.

$$\tilde{\phi}_\text{sn} = \frac{\tilde{\imath}_\text{sn}}{i_\text{bn}} = \left(\frac{Fq(P_\text{LO} + P_\text{RX})}{R\gamma P_\text{LO} P_\text{RX}}\right)^{1/2}. \tag{2.5}$$

Equation 2.5 clearly shows that an APD with an excess noise factor F always presents a shot noise contribution higher than an equivalent PIN photodiode, if the responsivity R of both devices is the same. If the setup is shot-noise-limited, as is the case for the photoreceiver in intersatellite laser interferometers (see Section 1.6.4), the use of APDs is not a viable option.

On the other hand, APDs are widely used in applications where the electronic noise of the photoreceiver is the limiting factor. Equation 2.6 shows the electronic noise contribution in terms of phase noise.

$$\tilde{\phi}_{\text{en}} = \frac{\tilde{\imath}_{\text{en}}}{i_{\text{bn}}} = \left(\frac{\tilde{\imath}_{\text{en}}}{R^2 M^2 \gamma P_{\text{LO}} P_{\text{RX}}} \right)^{1/2} . \tag{2.6}$$

The internal gain M decreases the phase noise, since the photoreceiver electronic noise contribution is independent of the photodetection process. In applications like single-photon detection, where the detector noise is the limitation, APDs are the preferred choice.

2.1.3 Two-dimensional materials

The trends of the last decade indicate that the future of photodetection will be linked to two-dimensional materials [70]. Their versatility and customizability promise field-changing solutions, such as transparent and flexible large area infrared detectors [71]. Two-dimensional materials seem also promising for improvements in photodetection for optical communications and laser metrology in the near-infrared range. A responsivity R of $1.21\,\mathrm{A\,W^{-1}}$ at 1064 nm using reduced graphene oxide (RGO) has recently been reported [72]. However, the device exhibited a response time of seconds. A device based on a graphene-molybdenum telluride-graphene heterostructure presented a lower responsivity ($0.110\,\mathrm{A\,W^{-1}}$ at 1064 nm) but showed a response time of the order of microseconds [73]. Even though these highly tunable materials seem promising, practical solutions for the photoreceiver of an intersatellite laser interferometer seem unavailable in the near future. The best solution still is an InGaAs-based PIN photodiode, for the reasons described in Section 2.1.

2.2 The transimpedance amplifier

The transimpedance amplifier (TIA) is the most common term referring to the device which converts an input current into an output voltage. Based on its operation principles, this device was traditionally called current-to-voltage converter. As described in Section 1.6.2, the TIA is one of the two fundamental blocks of a photoreceiver. The specifics of the TIA are dictated by the application and photodetector used. In the simplest case, a resistor can act as TIA, as seen in Figure 2.3. Using basic circuit theory, the frequency-dependent output voltage V_{o} is defined by Equation 2.7.

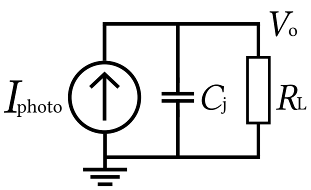

Figure 2.3: Circuit diagram of a resistor-based TIA. R_L is the load resistor connected to the reverse-biased photodiode. A small resistor increases the bandwidth but also increases the noise and reduces the transimpedance gain. With this topology, the bias voltage over the photodiode is not fixed and depends on the amount of photocurrent.

$$\begin{aligned} V_o &= I_{photo}\frac{R_L}{j2\pi f C_j R_L + 1}, \\ [V_o] &= \mathrm{V}, \end{aligned} \tag{2.7}$$

where R_L is the load resistor connected to the reverse-biased photodiode, f is the frequency of the photocurrent and j is the imaginary unit. At DC (f = 0), the output voltage is simply $V_o = I_{photo}R_L$, and decreases over frequency. The cut-off frequency f_{3dB} of such a topology is $1/(2\pi R_L C_j)$, which is the first limitation of this simple approach. A small resistor increases the bandwidth but also increases the noise and reduces the transimpedance gain (as described later in Section 2.2.1). Additionally, the bias voltage over the photodiode is not fixed and depends on the amount of photocurrent, which changes the output voltage. This is an unwanted feature in a photoreceiver, since important parameters (i.e. the photodiode junction capacitance) are bias voltage dependent. In other words, a photoreceiver needs a TIA with a very low input impedance [48, p. 70].

The performance of a photoreceiver for intersatellite laser interferometry is mainly defined by two main parameters: noise and bandwidth. In some practical implementations like the LISA mission, the high number of photoreceivers in a single spacecraft additionally increases the importance of the power consumption.

The phase noise contribution of the photoreceiver to the long-arm interferometer phase noise was introduced in the noise budget calculations of Section 1.6.4. An optimal TIA would present the lowest photoreceiver electronic noise $\tilde{\imath}_{en}$ possible. The last LISA performance model and error budget [46] indicates that the current best estimate for the photoreceiver electronic noise $\tilde{\imath}_{en}$ is 3.5 pA Hz$^{-1/2}$, which yields a displacement noise of 2.2 pm Hz$^{-1/2}$. The electronic noise requirement must be fulfilled in the full heterodyne frequency range, up to 25 MHz in the case of LISA. The nature of the electronic noise is diverse, but it can always be interpreted as an equivalent current noise source at the input of the photoreceiver, which competes with the generated photocurrent. This situation is described in Figure 2.4.

The range of the heterodyne beat-note frequency determines the bandwidth needed

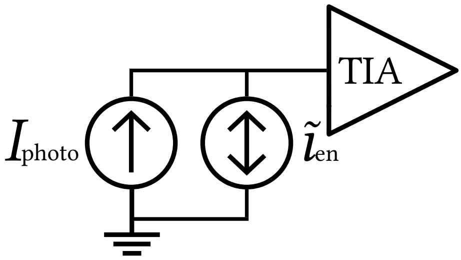

Figure 2.4: Photoreceiver electronic noise $\tilde{\imath}_{\text{en}}$ represented as a current noise source in parallel with the photocurrent from the photodiode. The TIA is assumed to be ideal. The effect of the photodiode junction capacitance C_{j} is included in $\tilde{\imath}_{\text{en}}$, shown in Equations 2.14 and 2.15.

in the photoreceiver. The ideal response would be flat in magnitude and phase, with an abrupt step and no gain right above the maximum expected heterodyne frequency. A flat magnitude response should be maintained so that the amplitude of the beat-note is always the highest possible. A decrease in the beat-note RMS value increases the displacement noise produced by the photoreceiver in the readout chain, since it degrades the carrier-to-noise ratio (Equations 1.12 and 1.14). A flat phase response is in general beneficial for thermally induced noise and finite phase response noise. In practice, an ideal flat response for both magnitude and phase is difficult to achieve. A sufficiently fast TIA combined with an AAF can approximate the ideal behavior well.

The photodetector, the first stage of the photoreceiver, needs to respond very quickly to variations of the input optical signals. The variations in the MHz range of the nW level AC beat-note are not an issue for modern InGaAs-based photodiodes with a low (5 V) bias voltage. The TIA electronics must provide enough gain within the heterodyne MHz range. With sufficient gain in the first TIA stage, the following stages are not critical in terms of noise [74]. The required bandwidth usually translates to electronics with unity gain frequencies, of the order of GHz.

2.2.1 Operational amplifiers

A TIA based on an operational amplifier (OpAmp) is probably the most common solution for the current-to-voltage conversion in a photoreceiver. Figure 2.5 shows the schematic of a basic OpAmp-based TIA. A resistor connects the output of the device to the inverting input, creating a negative feedback path. The photodetector is also connected to the negative input of the OpAmp. The positive input is connected to ground. An OpAmp ideally fulfills two main rules if operated in a negative feedback configuration:

- The output always tries to make the voltage difference between the inputs zero.

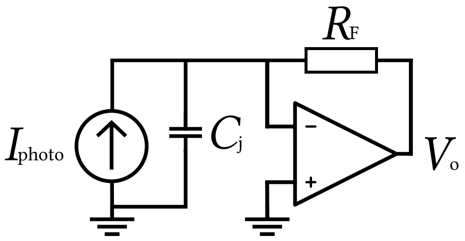

Figure 2.5: Electrical diagram of an OpAmp-based TIA. A feedback resistor connects the output of the OpAmp to the inverting input. The value of the resistor sets the TIA gain.

- There is no current being drawn into the inputs.

The negative input node is held at the same potential as the positive input (virtual ground), which translates to a TIA with a low input impedance. The virtual ground fixes the DC voltage drop on the reverse-biased photodiode, making the junction capacitance stable. The output voltage at DC can be simply obtained as $V_o = -I_{photo}R_F$ [48, p. 62]. For the AC behavior of the OpAmp, which will allow us to estimate the bandwidth, the non-ideal behavior of the device needs to be considered.

The limited bandwidth of a real OpAmp is usually defined by the gain bandwidth product (GBWP), the frequency at which the gain of the device is one. In an open-loop configuration, the frequency response of the OpAmp can be approximated with a dominant-pole model [75, p. 2]. The frequency response starts with high gain at low frequencies and rolls off at a 10% rate gain drop per decade, reaching the gain of one at the GBWP. For intermediate frequencies the phase is −90° shifted at the output, until the effect of other non-ideal OpAmp components (such as transistor cut-off frequency) dominates. The open-loop transfer function A_{OL} of the dominant-pole model described above is given by Equation 2.8 [75, p. 2].

$$\begin{aligned} A_{OL} &= \frac{A_{OL_{DC}}}{1 + \frac{j2\pi f}{2\pi f_c}}, \\ [A_{OL}] &= 1, \end{aligned} \tag{2.8}$$

where j is the imaginary unit, $A_{OL_{DC}}$ is the open-loop gain at DC and f_c is the cut-off frequency at which the open-loop gain becomes $0.707 \times A_{OL_{DC}}$. These two parameters are related to the GBWP according to Equation 2.9 [75, p. 4].

$$\begin{aligned} \text{GBWP} &= A_{OL_{DC}} f_c, \\ [\text{GBWP}] &= \text{Hz}. \end{aligned} \tag{2.9}$$

The feedback resistor R_F needed for the transimpedance configuration is part of the feedback network β. We also need to include in β the junction capacitance C_j of the photodiode and the parasitic input capacitance of the OpAmp C_op. Using the voltage divider rule, the transfer function of the feedback network β is given by Equation 2.10.

$$\begin{aligned} \beta &= \frac{V_-}{V_\mathrm{o}} = \frac{Z_\mathrm{i}}{Z_\mathrm{F}+Z_\mathrm{i}} = \frac{\frac{1}{j(C_\mathrm{op}+C_\mathrm{j})2\pi f}}{\frac{1}{j(C_\mathrm{op}+C_\mathrm{j})2\pi f}+R_\mathrm{F}}, \\ [\beta] &= 1. \end{aligned} \tag{2.10}$$

The closed-loop transfer function of the TIA Ω_TIA is given by Equation 2.11 [75, p. 2].

$$\begin{aligned} \Omega_\mathrm{TIA} &= \frac{V_\mathrm{o}}{I_\mathrm{i}} = \frac{V_\mathrm{o}}{V_\mathrm{i}/Z_\mathrm{i}} = A_\mathrm{CL}Z_\mathrm{i} = \frac{Z_\mathrm{i}A_\mathrm{OL}}{1+A_\mathrm{OL}\beta} = \frac{\beta Z_\mathrm{F}A_\mathrm{OL}}{1+A_\mathrm{OL}\beta} = \frac{Z_\mathrm{F}}{\frac{1}{A_\mathrm{OL}\beta}+1}, \\ [\Omega_\mathrm{TIA}] &= \Omega. \end{aligned} \tag{2.11}$$

Depending on the values, this TIA closed-loop transfer function could present some peaking due to the second pole introduced by the input capacitance (mostly from C_j). For that reason, it is common practice to add a small capacitor in parallel to the feedback resistor, adding an additional zero to the transfer function, in Z_F [75, p. 2]. The effect of this compensation can be seen as an increment of the phase margin, or in a different picture, as a decrease in the Q factor of the magnitude response.

Figure 2.6 shows the magnitude and phase of the TIA transfer function $\Omega(f)$ for different values of C_F, ranging from 1 pF to 10 pF. The values of the other OpAmp and circuit components are given in Table 2.2. To sum up, the bandwidth of the photoreceiver increases with lower C_j and higher GBWP.

Table 2.2: Component values used to calculate the frequency response of an OpAmp-based TIA (Figure 2.6).

$A_{\mathrm{OL}_\mathrm{DC}}$	98	dB
GBWP	1.5	GHz
R_F	20	kΩ
C_j	11	pF
C_op	1	pF

Equation 2.12 provides the value of the feedback capacitor C_F that yields an optimal Butterworth flat frequency response with a Q factor of 0.707 [76].

$$C_\mathrm{F}^\mathrm{opt} \approx \left(\frac{C_\mathrm{j}+C_\mathrm{op}}{\pi R_\mathrm{F}\mathrm{GBWP}}\right)^{1/2}. \tag{2.12}$$

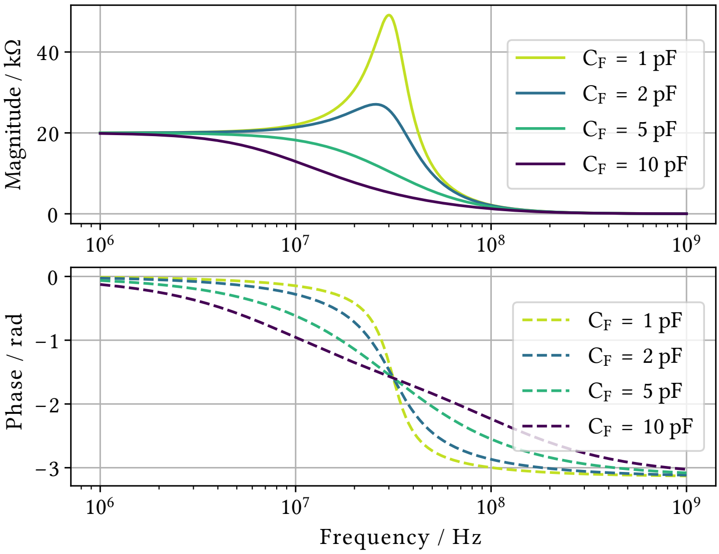

Figure 2.6: Frequency response (magnitude and phase) of an OpAmp-based TIA using the parameters from Table 2.2 and several values of C_F. The effect of C_F can be seen as an increment of the phase margin, or as a decrease in the Q factor of the magnitude response.

When using C_F^{opt}, the 3 dB bandwidth of the TIA frequency response is given by Equation 2.13 [76].

$$f_{3dB} = \left(\frac{\text{GBWP}}{2\pi R_F (C_j + C_{op} + C_F^{opt})} \right)^{1/2}, \qquad (2.13)$$
$$[f_{3dB}] = \text{Hz}.$$

The inner components of an OpAmp produce electronic noise, which competes with the desired photocurrent as seen in Figure 2.4. The noise of an OpAmp is generally described as a combination of a voltage noise source $\tilde{e}_n$ and a current noise source $\tilde{\imath}_n$. Figure 2.7 is an adaptation of Figure 2.5 illustrating the OpAmp noise sources as well [77, p. 2].

The equivalent input current noise source $\tilde{\imath}_{en}$ is a convenient figure of merit since it can be used for noise budget calculations without the full knowledge of the photoreceiver parameters (Section 1.6.4). Equation 2.14 gives $\tilde{\imath}_{en}$, by incoherently adding

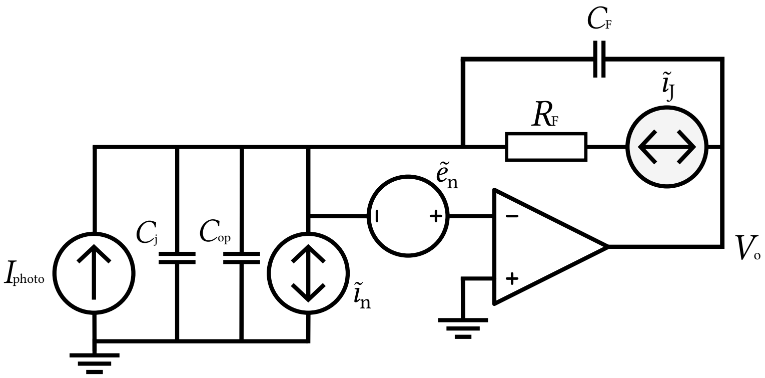

Figure 2.7: Noise in an OpAmp-based TIA. The noise of an OpAmp is described by a voltage noise source $\tilde{e}_n$ and a current noise source $\tilde{\imath}_n$. The input current noise $\tilde{\imath}_{en}$ is obtained from the incoherent sum of the OpAmp noise contributions and the Johnson noise of the feedback resistor $\tilde{\imath}_J$ (Equation 2.14).

the contributions of the OpAmp noise sources and the Johnson noise of the feedback resistor $\tilde{\imath}_J$ [77, p. 2].

$$\tilde{\imath}_{en} = \left(\tilde{\imath}_J^2 + \tilde{\imath}_n^2 + \left(\frac{\tilde{e}_n}{|Z_T|} \right)^2 \right)^{1/2}, \tag{2.14}$$

with $|Z_T|$ being the modulus of the total circuit impedance seen from the OpAmp inverting input, which is the parallel combination of the capacitors and the feedback resistor. $|Z_T|$ is given by Equation 2.15 [77, p. 2].

$$\begin{aligned} |Z_T| &= \frac{R_F}{\left(\left(2\pi f R_F (C_j + C_{op} + C_F) \right)^2 + 1 \right)^{1/2}}, \\ [|Z_T|] &= \Omega. \end{aligned} \tag{2.15}$$

The Johnson noise of the feedback resistor is given by Equation 2.16 [77, p. 2].

$$\tilde{\imath}_J = \left(\frac{4 k_B T}{R_F} \right)^{1/2}, \tag{2.16}$$

where k_B is the Boltzmann constant and T the temperature of the feedback resistor R_F. Resistors based on the metal electrode leadless face (MELF) technology, used in high-end low-noise audio electronics, also present this intrinsic Johnson noise contribution $\tilde{\imath}_J$. The lower excess noise at low frequencies in MELF resistors does not confer an advantage at MHz heterodyne frequencies [78]. In Equation 2.14, the two current noise sources are simply added quadratically, whilst the contribution of the voltage noise source needs to be converted first to current noise via $|Z_\mathrm{T}|$. At typical heterodyne frequencies of intersatellite laser interferometers, the photoreceiver electronic noise $\tilde{\imath}_\mathrm{en}$ is dominated by the voltage noise contribution. This situation is particularly critical when having a relatively high photodiode junction capacitance.

Figure 2.8 shows the theoretical input current noise density $\tilde{\imath}_\mathrm{en}$ when using three high speed ultra-low noise OpAmp models. The feedback network is formed by C_F = 1 pF and R_F = 25 kΩ. The junction capacitance of the photodiode used is 10 pF. These are typical values of a TIA for intersatellite interferometry. Considering that the goal is the minimum noise at the highest heterodyne frequency (25 MHz), the LMH6624 provides the best performance. Table 2.3 summarizes the parameters of the OpAmp models.

Table 2.3: Parameters of high speed, ultra-low noise OpAmps

	Type	GBWP / MHz	$\tilde{\imath}_\mathrm{n}$ / pA	$\tilde{e}_\mathrm{n}$ / nV	C_op / pF	I_q / mA
LMH6624	Bipolar	1800	2.3	0.92	0.9	12
EL5135	Bipolar	1500	0.9	1.5	1	6.7
LTC6268-10	FET	4000	0.007	4	0.45	16.5

Section 2.2.3 delves into the underlying technologies used in OpAmps and how they affect the bandwidth and particularly the noise properties.

The power consumption of an OpAmp is given by its quiescent current I_q and the supply voltage range. In general, high speed low noise OpAmps are not optimized for power consumption and have a quiescent current of 6 mA or higher. This is one of the major drawbacks of using a traditional OpAmp-based scheme.

2.2.2 The DC path

From Equation 1.5 and 1.6 and the LISA parameters from Table 1.2, we can infer that the generated photocurrent, I_photo, contains an AC beat-note of the order of nW superimposed on a DC component usually in the µW regime. The disparate signal levels require special care in the photocurrent amplification. There are essentially two approaches:

- Using a common TIA stage for both the AC and the DC component of the photocurrent (as shown in Figure 2.5), splitting the signals in following stages. The main issue with this approach is that the DC component can saturate the common stage if the local oscillator power P_LO or the feedback resistor R_F are too high. Reducing P_LO increases the electronic noise contribution $\tilde{\phi}_\mathrm{en}$ (Equation 1.14), affecting the desired shot-noise-limited operation. Lowering R_F has a similar effect on $\tilde{\phi}_\mathrm{en}$ (Equations 2.14, 2.15 and 2.16). On the positive side, the stability criteria

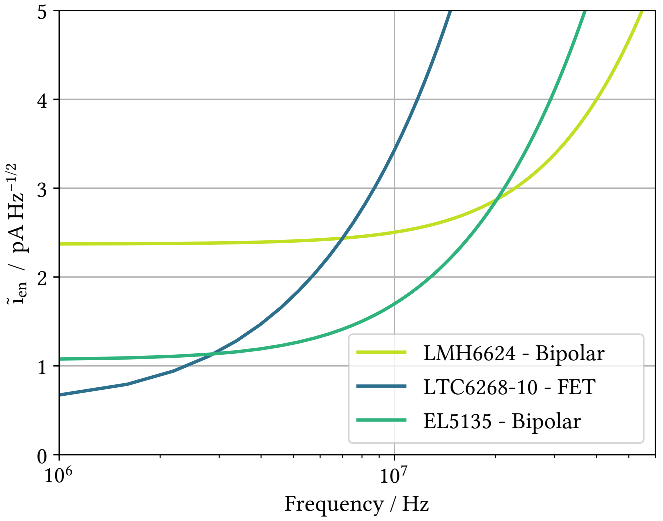

Figure 2.8: Theoretical input current noise $\tilde{\imath}_{en}$ of a TIA for several OpAmp models. The values used for the rest of the components are $C_F = 1$ pF, $R_F = 25$ kΩ and $C_j = 10$ pF. The LMH6624 provides the best performance with the lowest noise at 25 MHz. Table 2.3 summarizes the parameters of the OpAmp models.

and the noise analysis are well known in this scheme, as seen in Section 2.2.1. Matching the output of the first common OpAmp with the following separated AC and DC stages is also not critical.

- The second approach is the so-called direct split, and the circuit diagram of this topology is shown in Figure 2.9. Here, the DC and AC components are separated right after the photodiode. The advantage of this topology is that different gains can be used for the two components of the optical power, avoiding saturation regardless of the signal levels. Additionally, the AC-coupled path allows the realization of a TIA based on discrete transistors with independent biasing conditions. Discrete transistors in a TIA can potentially improve the performance of the photoreceiver (Sections 2.2.4 and 3.5). On the other hand, the direct split topology could suffer from additional electronic noise from the DC stage if not correctly isolated. The stability criteria for the split topology are more complex and, in general, SPICE simulations need to be performed.

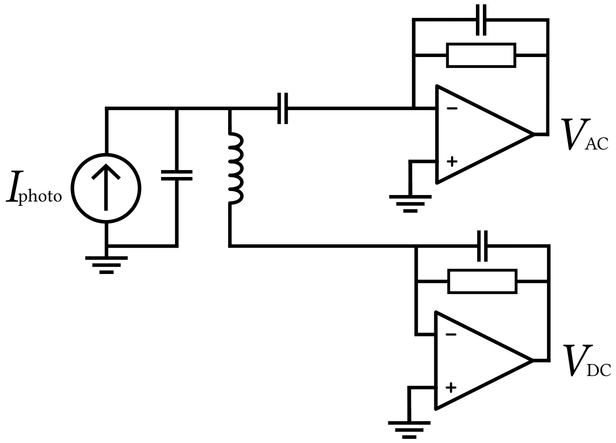

Figure 2.9: Circuit diagram of the split TIA configuration. Different gains can be used for the DC and AC components. The AC-coupled path allows the realization of a TIA based on discrete components with independent biasing conditions (Sections 2.2.4 and 3.5). The split topology could suffer from additional electronic noise from the DC TIA.

2.2.3 BJT vs FET

The first OpAmps available were based on vacuum tubes, with the first patent created in 1941 at Bell Laboratories. The concept of negative feedback in amplifiers, a cornerstone in countless fields and applications including the OpAmps, was conceived by Black in 1934, also at Bell Laboratories. The OpAmps of the second half of the 20th century benefited from the boom in semiconductor technology mentioned in Section 2.1.1. The main difference with respect to large area semiconductor-based photodetectors is that in OpAmps other design techniques are used to create highly dense integrated circuits with all the building blocks that form an OpAmp. These building blocks are based on transistors that subsequently form current mirrors and differential amplifiers among others. This set of functional blocks provide the close-to-ideal OpAmp properties described in the Section 2.2.1.

OpAmps can be divided into two main categories based on the technology of their internal transistors. Some OpAmps feature bipolar junction transistors (BJTs) and others feature field effect transistors (FETs). Some OpAmps use both technologies to obtain better results in specific applications. In general, both types of OpAmps can nowadays offer the fast operation needed for MHz photoreceivers. The deciding factor for inter-satellite laser interferometers is the noise performance, which depends on the transistor technology of the OpAmp input stage.

Bipolar-based devices, like the LMH6624 from Figure 2.8, present higher $\tilde{\imath}_{\text{n}}$ than their FET-based counterparts. FET devices can easily reach fA $\mathrm{Hz}^{-1/2}$ current noise levels, due to the low current being injected at the transistor gate. On the other hand, the voltage noise $\tilde{e}_\mathrm{n}$ in bipolar devices is usually lower. As shown in Figure 2.8, models with higher voltage noise present a higher input current noise $\tilde{\imath}_\mathrm{en}$ at high heterodyne frequencies. A larger equivalent capacitance C_T magnifies this effect. For this reason, low noise high speed OpAmps based on bipolar technology are preferred for photoreceivers in intersatellite laser interferometry. Discrete heterojunction bipolar transistors (HBTs) for mobile communication, low noise amplifiers (LNAs) feature lower voltage noise $\tilde{e}_\mathrm{n}$ levels than commercially available bipolar OpAmps. The details about this technology are presented in Section 2.2.4 and the design and characterization of a new photoreceiver based on HBTs is presented in Section 3.5.

2.2.4 Discrete transistors

Prior to the hegemony of OpAmps, discrete semiconductor-based transistors were used to build simple TIAs. Back in the 1950s, the term preamplifier was commonly used to refer to the TIA [79]. In early designs, a transistor in a common emitter configuration was used to amplify the photocurrent, inducing voltage variations on a load resistor connected to the transistor collector. This simple configuration was later improved by adding an additional transistor, forming a cascode configuration. This configuration reduces the Miller capacitance and improves the frequency response of the device, as described in [80]. Discrete transistor designs did not become completely obsolete with the rise in popularity of OpAmps. Some photodetectors still benefited from the higher performance of particular transistor models. For example, better sensitivity was achieved by using transistors with high DC current gain β_0 (not to be confused with the transfer function of the feedback network β) and low input capacitance in [81]. A design based uniquely on discrete components is shown in Figure 2.10. A similar design was featured in [81]. Besides the cascode input stage, the TIA features an emitter follower as a voltage buffer which provides a low output impedance. The feedback resistor in this design provides the necessary transimpedance operation ($\Omega = V_o I_\mathrm{photo}^{-1}$) and the biasing for the input transistor. An AC-coupled feedback is also possible. This requires extra components for proper biasing of the input transistor but simplifies the design. A new photoreceiver topology presented in Section 3.5, which combines discrete transistors with OpAmps, features AC-coupled feedback. The power consumption of a TIA based on discrete transistors is in general lower than that of a TIA based on a high speed ultra-low noise OpAmp, due to the relatively high quiescent current I_Q of the latter (6 mA or higher).

In the last decade, silicon-germanium (SiGe) heterojunction bipolar transistors (HBTs) have been improved to the point of being able to compete with traditional low noise technologies such as gallium arsenide (GaAs) high electron mobility transistors (HEMTs) [82]. The original concept of HBTs dates back to the 1950s, and it is based on joining

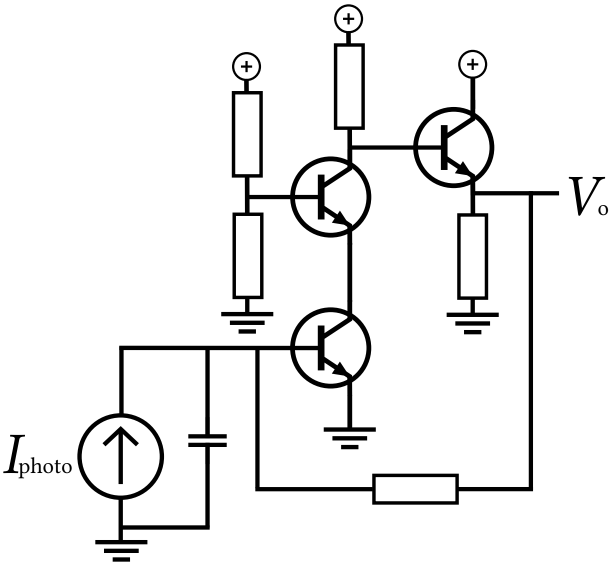

Figure 2.10: Circuit diagram of a transistor-based TIA. It features a cascode input stage and an emitter follower as a voltage buffer. The feedback resistor provides the transimpedance operation and the biasing for the input transistor. An AC-coupled feedback is also possible (Section 3.5).

diverse band gap structures to improve performance. Where BJTs only use differences in doping within a common semiconductor material to manipulate the absolute position of the material band gap across a junction, i.e. creating parallel potential barriers in valence and conduction band, an HBT switches semiconductor materials across its two junctions. This way, not only the band gap position but also its magnitude changes across the two junctions, such that the potential barrier in the emitter-base junction valence band is higher than its counterpart in the conduction band. Consequently, there is a limited injection of holes from the base into the emitter, due to the higher valence band compared to the conduction band. This increases the amount of doping that can be used in the base of the device, reducing an important noise-related parameter, the base-resistance ($r_{BB'}$), while maintaining the gain. In the specific case of SiGe devices, the gradual distribution of germanium in the base creates a corresponding gradual decrease of the band gap. The electric field that is subsequently created helps speed up the transport of the carriers and increases the frequency response. The parameter defining the speed of a transistor is usually the transition frequency f_T. The situation has improved further in last generation HBTs for mobile communications. In these devices, a small percentage of carbon is added to the alloy (SiGe:C) to achieve even a higher f_T

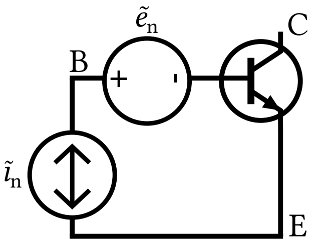

Figure 2.11: Bipolar junction transistor (BJT) noise model. As in the case of OpAmps, the noise of a BJT can be described with a voltage and a current noise source.

and a low $\mathrm{r_{BB'}}$ [83].

As in the case of OpAmps, the noise of a single transistor amplifier can be modeled with a voltage and a current noise source, as seen in Figure 2.11 [84]. The amount of noise generated by these two equivalent noise sources is determined not only by the physical properties of the device but also by its biasing. Equation 2.17 describes the voltage noise density $\tilde{e}_n$ in a BJT [84, p. 481].

$$\begin{aligned}\tilde{e}_\mathrm{n} &= \left(4k_\mathrm{B}T\left(\frac{V_\mathrm{T}}{2I_\mathrm{C}}+r_\mathrm{BB'}\right)\right)^{1/2}, \\ [\tilde{e}_\mathrm{n}] &= \mathrm{V\,Hz^{-1/2}},\end{aligned} \tag{2.17}$$

where k_B is the Boltzmann constant, T the temperature, V_T the thermal voltage, I_C the transistor collector current and $\mathrm{r_{BB'}}$ its base spreading resistance. Equation 2.18 describes the current noise density $\tilde{\imath}_\mathrm{n}$ in a BJT at frequencies above the flicker-noise corner frequency [84, p. 483].

$$\tilde{\imath}_\mathrm{n} = \left(2q\frac{I_\mathrm{C}}{\beta_0}\left(1+\frac{f}{f_\mathrm{T}}\right)\right)^{1/2}, \tag{2.18}$$

where q is the charge of an electron, β_0 the DC current gain of the BJT, and f_T the transition frequency at which the small signal current gain equals one. The transistor parameters $r_\mathrm{BB'}$ and f_T are fixed by the BJT materials and its geometry, while I_C can be changed using different DC operating points. Comparing Expressions 2.17 and 2.18, we can observe a trade-off between $\tilde{e}_\mathrm{n}$ and $\tilde{\imath}_\mathrm{n}$ as a function of the collector current I_C.

Last generation mobile communication HBTs feature high values of β_0 and f_T and low $r_\mathrm{BB'}$. Thanks to that, they can potentially outperform ultra-low noise bipolar-based OpAmps in terms of voltage noise $\tilde{e}_\mathrm{n}$. As described in Section 2.2.1, the voltage noise $\tilde{e}_\mathrm{n}$ dominates the photoreceiver electronic noise $\tilde{\imath}_\mathrm{en}$ at high heterodyne frequencies. A photoreceiver featuring HBTs was developed and characterized in the frame of this thesis (Section 3.5).

3 | Photoreceiver characterization

This chapter presents the characterization of different photoreceiver implementations, together with the measurement techniques and setups used. Section 3.1 describes a custom-made facility for measuring the spatial profile of quadrant photodiodes (QPDs), as well as a new functionality upgrade for the IfoCAD software to include the measured spatial responses in simulated interferometers. Thermally induced changes in the responsivity R of a silicon photodiode are studied in Section 3.2. Characterization methods to obtain noise and bandwidth of photoreceivers are presented in Section 3.3. Results from testing the photoreceiver flight models for GRACE-FO are presented in Section 3.4. Section 3.5 contains the details of the development and characterization of a new photoreceiver topology based on heterojunction bipolar transistors (HBTs) in conjunction with an off-the-shelf 0.5 mm diameter QPD. This new type of photoreceiver represents a competitive alternative to traditional OpAmp-based designs for future intersatellite interferometry missions.

3.1 Photodiode spatial response

In an intersatellite laser interferometer, the main longitudinal displacement is proportional to the average phase of all four QPD segments when the intensity of the interfering beams is integrated over the QPD area. Additionally, the angle between these beams is measured using the DWS technique [10, 85, 86] which relies on the differential phase between segments (see Section 1.6.2). QPDs used in our models have a uniform profile and no crosstalk between adjacent segments. Real QPDs might feature a non-uniform spatial response and crosstalk between adjacent segments. Non-uniformities could originate from dust particles or contamination on the QPD surface, misplaced wires, manufacturing defects or the internal structure of the QPD. Visual inspection (i.e. with a microscope) helps identify some of these issues but does not produce any quantitative information about the influence on the phase readout that could affect the longitudinal and DWS measurands mentioned above.

Previous research on the spatial response of photodetectors at different wavelengths was carried out by [87, 88, 89, 90, 91]. In this section, the spatially resolved response of several QPDs is presented. The operation of a computer-aided control-and-acquisition setup used to obtain the QPD responses is described. The laser wavelength chosen for the measurements is close to 1064 nm. Additionally, an extension of the optical simulation toolbox IfoCAD [92] was created, in order to include the measured QPD responses in simulations. In this way, the influence of real QPD features such as non-uniformities and crosstalk could be studied. The results presented in this section were published in Applied Optics [93].

Section 3.1.1 gives an overview of the setup built for the spatial characterization of QPDs. Section 3.1.2 contains the measured spatial responses of three QPD candidates for space-based interferometry. In Section 3.1.3, the optical simulation toolbox IfoCAD and its extension to include measured QPD responses are introduced. A description of the simulation environment along with results obtained using both the ideal QPD model and the measured response of a real QPD can be found in section 3.1.4.

3.1.1 Spatial characterization setup

Figure 3.1 shows the schematic of the setup, where the light of a fiber-pigtailed laser diode with 1066.7 nm center wavelength (LPS-1060-FC by Thorlabs) is collimated and injected onto a small optical bench. A lens with 50 mm focal length is used to focus the beam onto the device under test (DUT), a QPD. A beam diameter of 50 µm at the DUT was used in this work. The DUT is connected to a 4-channel TIA. The DUT can be scanned laterally over a 50 mm x 50 mm by means of stacked translation stages. The distance between the DUT and beam waist in the z-axis is controlled by a third translation stage (M-405.CG by Physik Instrumente).

The motion of the translation stages, as well as the sampling of the TIA output, is controlled by a LabVIEW program. A PCI-6014 data acquisition (DAQ) card by National Instruments samples the four channels at 200 kS s^{-1} with 16-bit resolution.

The optimal focusing of the laser beam on the DUT is achieved with the following procedure: The knife-edge method [94] is used to determine the beam diameter. This is repeated for a number of z-positions. The beam diameter of a Gaussian beam as a function of propagation distance is fitted to the measured diameter-distance pairs. The final z-position is chosen at the location of the fitted waist.

Once the focusing of the beam on the DUT is completed, the spatial response scan is performed with a translation in the x-axis, in which the photodiode moves from a starting point x_0 to a final point x_f, while the acquisition system records the QPD output signals using a sampling rate $\mathrm{f_s}$ that can be modified for every scan. Increasing $\mathrm{f_s}$ directly results in an increase of the number of samples in the x-coordinate $(x_0, x_1, x_2, ..., x_f)$. Choosing an $\mathrm{f_s}$ that generates x-axis steps $(\Delta x = x_{i+1} - x_i)$ very much below the laser

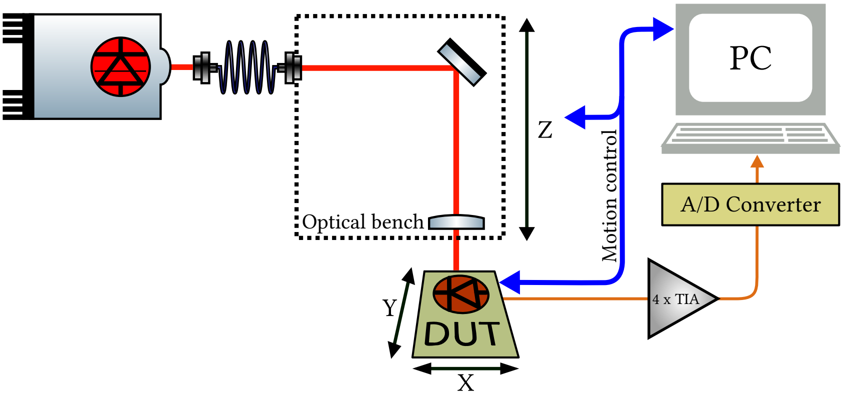

Figure 3.1: Schematic diagram of the experimental setup to measure the spatial response of photodiodes. The light of a fiber-pigtailed laser diode is collimated and injected onto a small optical bench. A focusing lens is used to focus the beam onto the DUT. The DUT is connected to a 4-channel TIA. The DUT position in the horizontal plane and the vertical position of the optical bench are set by translation stages. Motion of the stages and data sampling are controlled by a PC.

spot size does not increase the resolution further, since the detection of changes in the photodiode response is ultimately limited by the beam diameter. Theoretically, the measured response is a convolution of the probing Gaussian beam with the real photodiode response. The real photodiode response could be recovered using deconvolution algorithms, since the point spread function is, in principle, known. In reality, the point spread function of the probing beam is not exactly that of an ideal Gaussian beam. Any deviation from the theoretical model produces large errors, since the process of deconvolution involves dividing by very small numbers [95]. Only samples obtained when moving at constant velocity are stored in this part, discarding those recorded during the acceleration and deceleration phases of the translation stage. After the data have been recorded, the DUT returns to its start position x_0 and increments the y-position. Recording data only in one direction of the x-axis was chosen to eliminate the effects of hysteresis and mechanical play in the translation stage. This procedure is repeated several times within a y-axis range specified by the starting and final point (y_0,y_f) and the step size (Δy). Typical step sizes in x and y are below 10 µm.

3.1.2 Measured spatial response of quadrant photodiodes

Figure 3.2 presents the normalized spatially resolved response of the QP22 by First Sensor, a 5 mm diameter silicon QPD. The single segment response shows crosstalk between adjacent segments (see case 4 in Figure 3.8). This is discussed in Section 3.1.4.

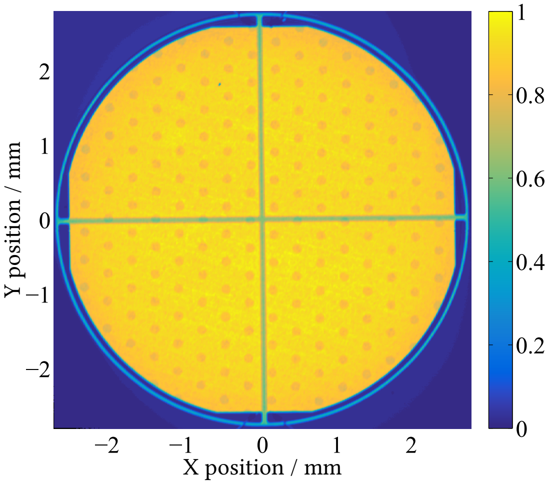

Figure 3.2: Normalized spatially resolved response of the QP22 by First Sensor. The sum of the four QPD segments was used for the plot. The measurement shows a distribution of spots across the photodiode surface with a 20% reduced responsivity. The low absorption of silicon in this wavelength range (typical responsivity of 0.2 A W^{-1}) is compensated by using a diffusely reflective layer below the active material to achieve a responsivity of 0.5 A W^{-1}. The reflectivity of this additional layer is affected by internal connections of the photodiode at the observed spots, reducing the responsivity [96].

The sum of the four QPD segments was used for Figure 3.2. The measurement shows spots across the photodiode surface with a 20% reduced responsivity. The spots are distributed along a hexagonal lattice and spaced 0.4 mm from one another. The QP22 is a silicon-based device designed to work at a wavelength of 1064 nm. The low absorption of silicon in this wavelength range (typical responsivity of 0.2 A W^{-1}) is compensated by using a diffusely reflective layer below the active material to achieve a responsivity of 0.5 A W^{-1}. The reflectivity of this additional layer is affected by internal connections of the photodiode at the observed spots, reducing the responsivity [96].

Figure 3.3 shows the normalized spatially resolved response of the GAP9119 by OEC GmbH, a 1 mm diameter InGaAs QPD with a gap of 20 µm between the active areas. At the outer edge of each segment, an area with reduced responsivity and bonding wires are visible. Figure 3.4 shows the normalized response of the FCIQ1000 by OSI Optoelectronics, also a 1 mm diameter InGaAs QPD but with a gap of 70 µm between the active areas. In both cases the sum of the four QPD segments was used for the plots and the responsivity deviation within the active area is around 1%.

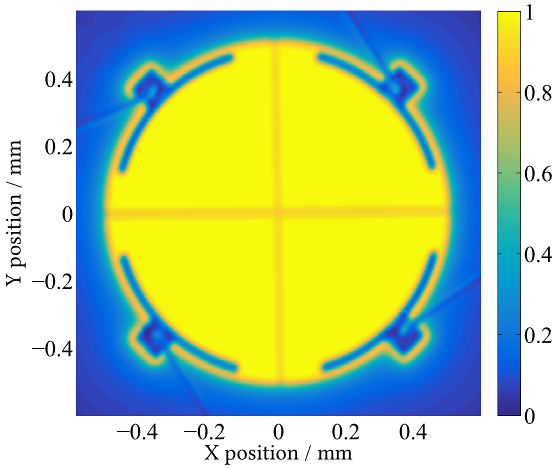

Figure 3.3: Normalized spatially resolved response of the GAP9119 by OEC GmbH. The sum of the four QPD segments was used for the plot. The responsivity deviation within the active area is around 1%.

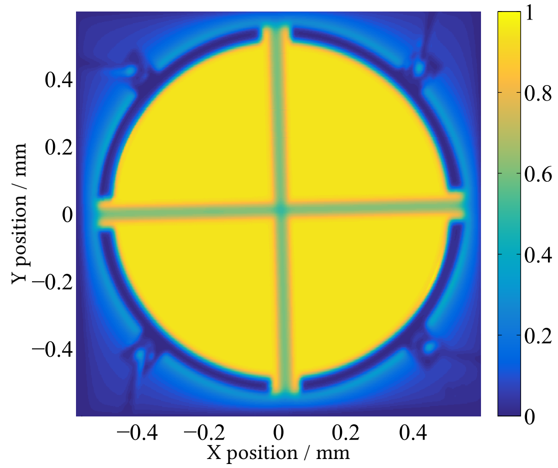

Figure 3.4: Normalized spatially resolved response of the FCIQ1000 by OSI Optoelectronics. The sum of the four QPD segments was used for the plot. The responsivity deviation within the active area is around 1%.

3.1.3 The IfoCAD extension

IfoCAD is a C/C++ software developed at the AEI in Hanover to simulate and optimize laser interferometers. IfoCAD can compute interferometric signals like longitudinal pathlength, DWS, differential power sensing (DPS) and contrast measurements [92]. At the core of IfoCAD, the electric fields of two interfering beams are integrated over the photodiode surface. So far, the response of the photodiode was assumed to be uniform over a given segment and zero outside. With the extension developed for this thesis, a specific photodiode response can be used to substitute the standard IfoCAD photodiode. Four matrices, describing the response of each segment, are loaded into the program during the simulation. The integration of the electric fields is performed as described in Equation 3.1 [97, p. 11],

$$\begin{aligned} \tilde{c}_i &= \frac{\int \mathrm{d}A\ E_1 E_2^* \tilde{R}_i}{\left(\int \mathrm{d}A\ E_1 E_1^* \tilde{R}_i \int \mathrm{d}A\ E_2 E_2^* \tilde{R}_i\right)^{1/2}}, \\ [\tilde{c}_i] &= 1, \end{aligned} \tag{3.1}$$

where A is the total area of the integral, E_1 and E_2 are the interfering electric fields and $\tilde{R}_i$ is the weighting factor from the measured normalized spatial response of segment i. E_1, E_2 and $\tilde{R}_i$ are in general dependent on the x and y positions. Equation 3.1 is usually referred to as the overlap integral. For the standard IfoCAD QPD model $\tilde{R}_i$ is equal to one within the bounds of an ideal segment. The denominator contains the normalization factors. The result $\tilde{c}_i$ is the normalized complex amplitude of segment i. Equation 3.1 is equivalent to Equation 1.5, in the sense that both the total optical power P_T and the complex amplitude $\tilde{c}_i$ contain the phase between the interfered electric fields. On the other hand, $\tilde{c}_i$ is normalized and does not take into account the characteristic impedance of the medium. Therefore, $\tilde{c}_i$ does not contain information about the actual DC and AC optical powers on the photodiode. To allow the adaptive integration method to evaluate the electric fields in any given point of the integral surface A, the required $\tilde{R}_i$ values are calculated by means of bilinear interpolation, with the photodiode response matrix as input. Once the electric fields are integrated over the QPD surface, IfoCAD can easily provide the fundamental measurands of the interferometric system. The normalized complex amplitudes are used to obtain the longitudinal pathlength signal (LPS) and the DWS signals [97, p. 12] (Equations 3.1, 3.2, 3.3, 3.4).

$$\begin{aligned} LPS &= \frac{\lambda}{2\pi} arg(\tilde{c}_A + \tilde{c}_B + \tilde{c}_C + \tilde{c}_D), \\ [LPS] &= \mathrm{m}. \end{aligned} \tag{3.2}$$

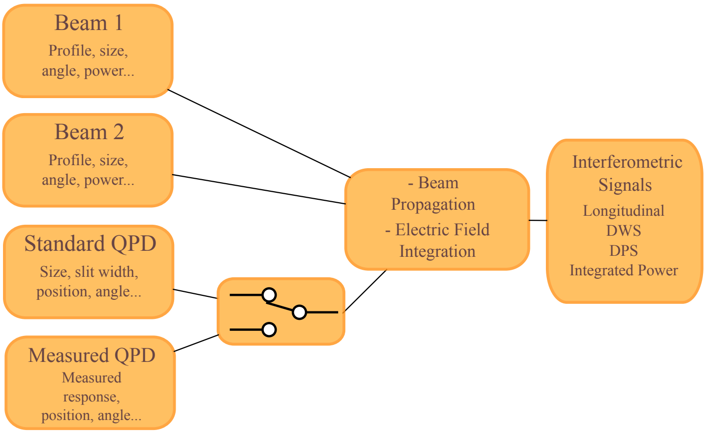
Beam 1
Profile, size, angle, power...
Beam 2
Profile, size, angle, power...
Standard QPD
Size, slit width, position, angle...
Measured QPD
Measured response, position, angle...
- Beam Propagation
- Electric Field Integration
Interferometric Signals
Longitudinal
DWS
DPS
Integrated Power

Figure 3.5: Flowchart of an IfoCAD simulation including the extension for measured QPD responses. First, the two interfering beams and the QPD are created and their parameters specified. At this stage, we can choose between the standard QPD model or a measured QPD response. Then, IfoCAD propagates the beams until they reach the QPD position and integrates the electric fields over the given surface. After that, the main interferometric signals can be obtained.

$$\begin{aligned} DWS_{\mathrm{H}} &= arg\left(\frac{\tilde{c}_A + \tilde{c}_C}{\tilde{c}_B + \tilde{c}_D}\right), \\ [DWS_{\mathrm{H}}] &= \mathrm{rad}. \end{aligned} \tag{3.3}$$

$$\begin{aligned} DWS_{\mathrm{V}} &= arg\left(\frac{\tilde{c}_A + \tilde{c}_B}{\tilde{c}_C + \tilde{c}_D}\right), \\ [DWS_{\mathrm{V}}] &= \mathrm{rad}. \end{aligned} \tag{3.4}$$

Here λ is the wavelength of the light wave. Figure 3.5 shows a block diagram of the process. By comparing the results using the standard QPD model and the measured QPD response, conclusions about the effect of the real QPD spatial response on the measurands can be obtained.

3.1.4 Simulation setup and results

Since the main motivation was to study the influence of non-uniform responses in the main measurands, the QP22 response was chosen for the simulations in IfoCAD. The larger fluctuations in its response would in principle intensify degradation in the

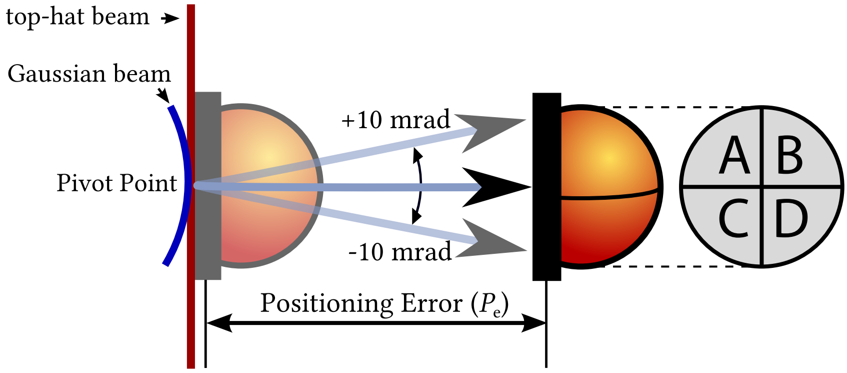

Figure 3.6: Scheme of the simulation setup used, based on the interferometer conditions in an intersatellite laser ranging mission like GRACE-FO. A 1.675 mm waist radius Gaussian beam (in blue) was used for the local beam, with the waist located at the pivot point. The red line represents the received top-hat beam wavefront. Yaw and pitch tilts from −10 mrad to 10 mrad were applied to both beams simultaneously, which would ideally lead to zero longitudinal and DWS signals. Three different QPD positions with respect to the pivot point (P_e) were used: 0 mm, 0.5 mm and 1 mm, in order to study deviations from the ideal case.

performance. In general, imaging systems are used in laser interferometers to focus beams on the photodiode surface, to reduce beam walk that could produce unwanted tilt-to-length coupling and to remove diffraction patterns in clipped top-hat beams. The lens system images the received aperture and the local beam waist onto the QPD surface, as depicted on the left side of Figure 3.6. In the particular case of the GRACE-FO mission, both input beams have the same angle of incidence, which varies a few mrad during operation due to spacecraft attitude changes.

The pivot point for tilts in the input beams would ideally be located on the photodiode center itself. A positioning error (P_e) when building the optical bench would translate to a wrongly placed photodiode, which leads to beam walk and tilt-to-length coupling. In the simulations, a variation in the angle of incidence of the beams was applied in order to understand the coupling in the main longitudinal and DWS signals in the presence of photodiode placement errors. The standard IfoCAD QPD model was used first, with a 2.7 mm radius and a 70 µm gap width (according to the QP22 datasheet), followed by the QP22 measured response. Three values for the separation between the pivot point and the photodiode (P_e) were used: 0 mm, 0.5 mm and 1 mm. A 1.675 mm waist radius Gaussian beam was used for the local beam, with the waist located at the pivot point. For the received beam, a top-hat beam larger than the QPD was used. This setup recreates the conditions of an intersatellite interferometric system

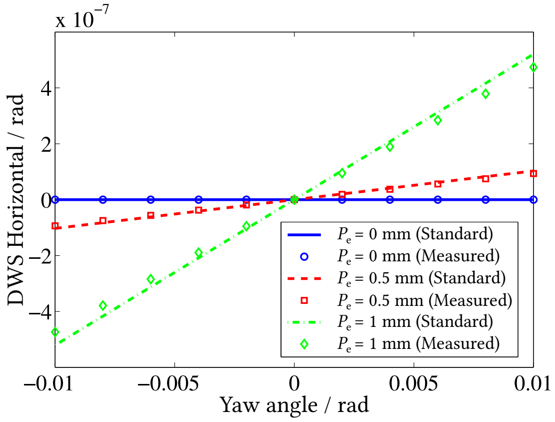

Figure 3.7: Horizontal DWS signal for yaw tilts obtained in the simulations. Results for the vertical DWS signals are equivalent and are omitted for the sake of clarity. The tilt is applied to both beams simultaneously. The lines correspond to simulations with the standard IfoCAD QPD, and the markers to ones with the measured QP22 response. There is an increasing deviation from zero for larger P_e in both the standard and the measured response.

like the one in GRACE-FO or LISA.

The yaw and pitch tilts were applied to both beams simultaneously, which would ideally lead to zero longitudinal and DWS signals. The maximum absolute tilt used was 10 mrad.

Figure 3.7 shows the results obtained for the horizontal DWS signals. Results for the vertical DWS signals using different pitch tilts are equivalent and are omitted for the sake of clarity. There is a degradation towards larger P_e, where the DWS signals deviate from zero when tilts are applied, both for the standard and the enhanced QPD models. Results indicate however that the deviation slightly decreases with the measured QP22 response. In order to investigate this further, two additional simulations were performed using modified measured QPD responses. Figure 3.8 shows the single segment response used in these additional simulations (Cases 2 and 3), together with the standard QPD model (Case 1) and the unmodified measured QPD response (Case 4).

In case 2, the QPD response is uniform within the segment and non-zero outside. That includes not only the gap but also crosstalk from adjacent segments. Case 3 is the opposite: the response is non-uniform within the segment but zero outside. Figure 3.9 shows the results obtained for the horizontal DWS signals at P_e = 1 mm for all 4 cases. Again, results for the vertical DWS signal are equivalent and therefore omit-

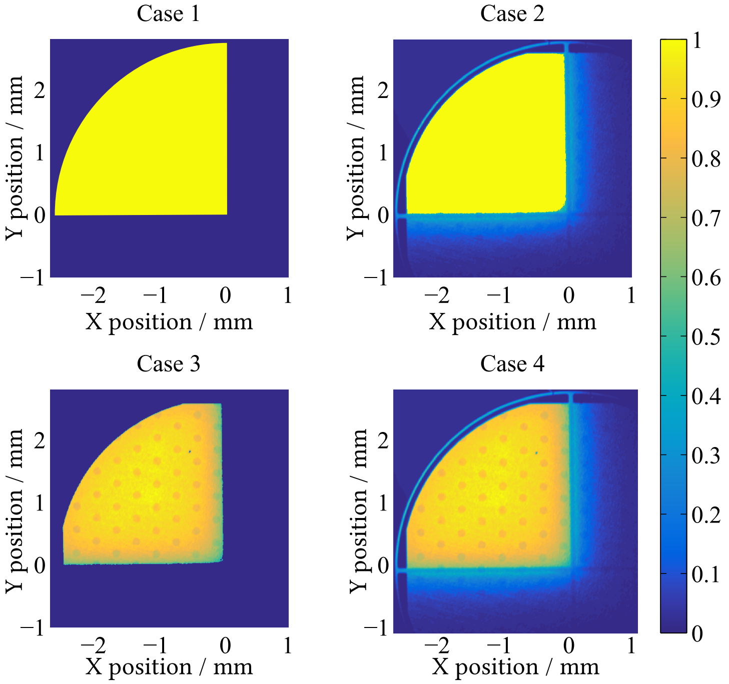

Figure 3.8: Example of a single segment response of the standard QPD model (Case 1), the modified profiles for additional simulations (Case 2 and 3) and the unmodified measured QPD response (Case 4). In case 2, the QPD response is uniform within the segment and non-zero outside. That includes not only the gap but also crosstalk from adjacent segments. Case 3 is the opposite: the response is non-uniform within the segment but zero outside.

ted. Cases 2 and 4 present roughly the same deviation, whereas it increases for cases 1 and 3. These results indicate that a non-zero response in the gap and the presence of crosstalk decrease deviations from zero in the DWS signal independently of the uniformity within the segment. In all cases, the maximum deviation of $\sim 0.1\,\mu$rad observed in the DWS signal is orders of magnitude below the maximum allowed value of 10 mrad for GRACE-FO.

Figure 3.10 shows the effect of simultaneous yaw tilts in both beams on the main longitudinal signal. Results for tilts in pitch are equivalent and therefore omitted. Once again, a degradation towards larger P_e for both the standard and the measured QPD can be observed, since the main longitudinal signal deviates from zero in a quadratic fashion when tilts are applied. The maximum of this quadratic trend shifts from 0 mrad

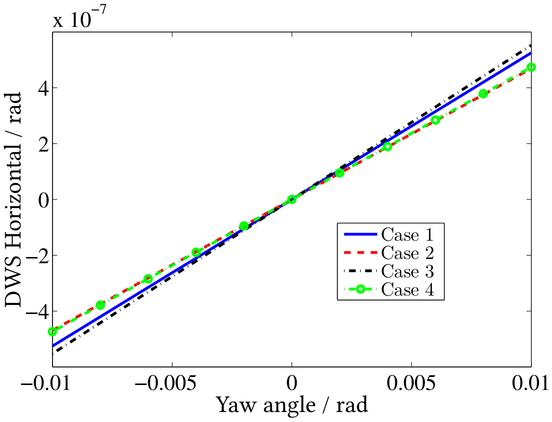

Figure 3.9: Horizontal DWS signal for yaw tilts at P_e = 1 mm for all 4 cases of Figure 3.8. In all cases, the maximum deviation of ~ 0.1 μrad observed is orders of magnitude below the maximum allowed value of 10 mrad for GRACE-FO.

to larger angles when the measured QPD response is used. Additional simulations at P_e = 1 mm were performed using the modified QPD responses of Figure 3.8. Results are shown in Figure 3.11. A lateral shift of the maximum for different responses can be seen. This maximum also represents the point of minimum coupling of this quadratic relation between the tilt angle and the longitudinal signal. In all cases, the maximum deviation of ~ 1 fm is very low compared to the maximum allowed value of 1 μm for GRACE-FO.

Results from these simulations indicate that deviations in the main measurands are of no concern in the simulated scenario, including standard and measured QPD profiles. This could open the door to future photodiode candidates that have excellent characteristics, such as a very low junction capacitance, and would otherwise have been rejected due to a non-standard profile.

The scans could be improved by reducing the spot-size of the beam. The measured responses presented here are a convolution of the probing beam with the actual QPD response. Numerical deconvolution was tested as an alternative to beam reduction but it introduces unwanted disturbances. A deviation of the probing beam from the 50 μm diameter Gaussian model could explain the disturbances. In the simulation environment, the large top-hat beam could be replaced with a more realistic clipped beam, whose diffraction patterns might also influence the measurands of interest.

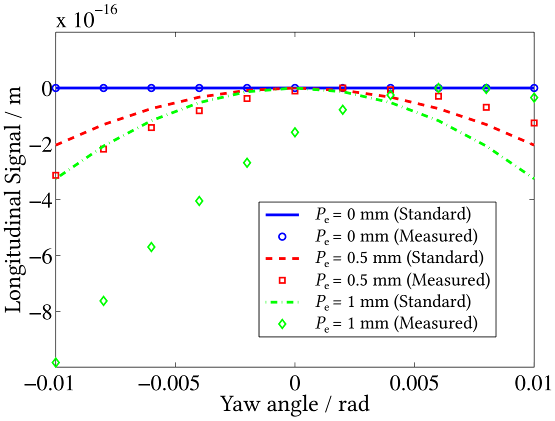

Figure 3.10: Main longitudinal signal for yaw tilts obtained in the simulations. Results for tilts in pitch are omitted for the sake of clarity. The tilt is applied to both beams simultaneously. The lines correspond to simulations with the standard IfoCAD QPD, and the markers to ones with the measured QP22 response. There is a degradation towards larger P_e for both the standard and the measured response.

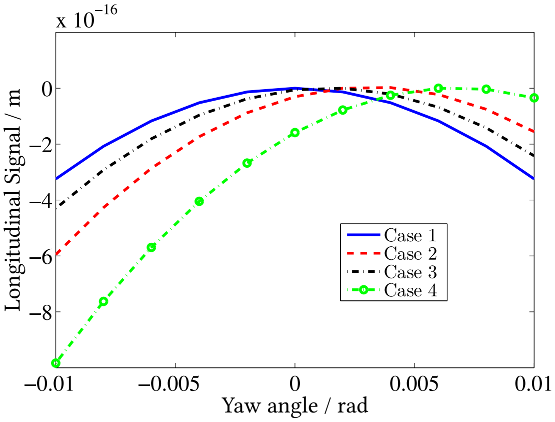

Figure 3.11: Main longitudinal signal for yaw tilts at P_e = 1 mm for all 4 cases of Figure 3.8. Results for tilts in pitch are equivalent and are omitted for the sake of clarity. A shift of the maximum (corresponding to the point of minimum coupling) for the different responses can be observed. In all cases the maximum deviation of ~ 1 fm is very low compared to the maximum allowed value of 1 µm for GRACE-FO.

3.2 Temperature stability of photodiodes

Temperature stability is essential in high precision metrology, as seen in Section 1.6.4 with the thermally induced photoreceiver noise. The thermal environment of components and equipment is in general monitored and controlled. Photodiodes are no exception, and characterizing the thermal dependence of their response is of great use for daily lab work and for noise estimation in more complex instruments and experiments. This section presents the thermal characterization of a silicon photodiode that is frequently used in the Space Interferometry group at the AEI.

The Satellite Test Environment for Laser Applications (STELA) at the AEI was used for the purpose of this test. STELA is a thermal vacuum chamber (TVAC) which can adjust the temperature of an optical table and shrouds in its interior. The adjustable temperature ranges from −65 °C to 125 °C, under a vacuum of 1×10^{-6} mbar. STELA also features an optical window which allows the transmission of 1064 nm optical beams. This facilitates the coupling of light into the chamber without optical fiber feedthroughs.

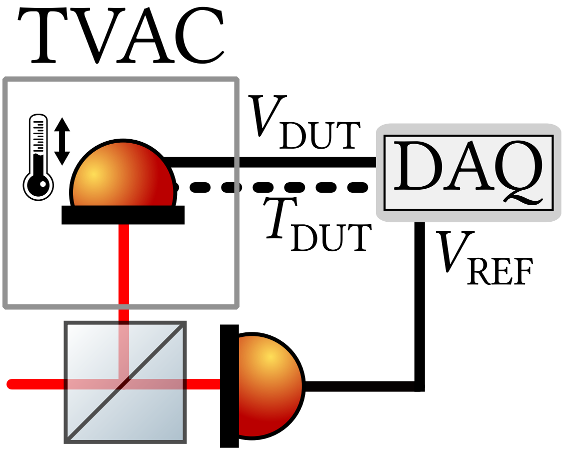

Figure 3.12: Setup for the thermal characterization of photodiodes. The photodiode under test is inside STELA and the reference photodiode is outside. The temperature of the DUT is changed while the output voltages are tracked. The ratio $V_{\mathrm{DUT}}V_{\mathrm{REF}}^{-1}$ cancels out power fluctuations of the laser source or induced by changes in optical components.

Figure 3.12 shows the setup used for the measurement. The device under test (DUT) was placed on the optical table inside STELA, whose temperature was swept from −40 °C to 85 °C. T_{DUT}, the actual temperature of the DUT in °C, was measured using a platinum temperature sensor. During the test, T_{DUT} ranged from −9 °C to 113 °C. The discrepancy between T_{DUT} and the set temperature was caused by the dissipated optical power on the photodiode. A reference monitor photodiode was placed outside the TVAC to monitor fluctuations in the optical signal. Both photodiodes were connected to TIAs (not shown in Figure 3.12). The output voltage from the TIAs (V_{DUT} and V_{REF}) and T_{DUT} were tracked in a LabVIEW-based DAQ system. A 50/50 beam splitter was used to illuminate the DUT and the reference photodiode simultaneously. The ratio $V_{\mathrm{DUT}}V_{\mathrm{REF}}^{-1}$ cancels out power fluctuations produced at the laser source or induced by changes in optical components. Two samples of the PC50-7 silicon photodiode (Figure 3.14) were tested using the setup described above. The ratio $V_{\mathrm{DUT}}V_{\mathrm{REF}}^{-1}$ versus temperature is shown in Figure 3.13 for one of the samples tested.

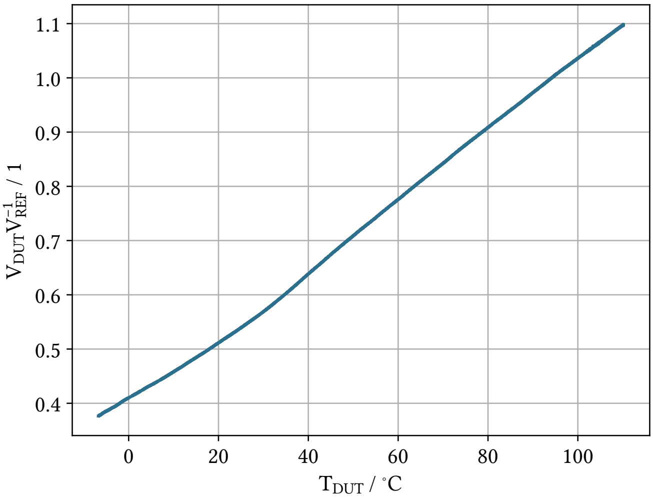

Figure 3.13: Ratio $V_{\mathrm{DUT}}V_{\mathrm{REF}}^{-1}$ versus temperature of a silicon-based photodiode (PC50-7). The ratio is a linear function of temperature. The two samples tested showed the same behavior.

The ratio $V_{\mathrm{DUT}}V_{\mathrm{REF}}^{-1}$ is a linear function of temperature. The same behavior was observed for the two samples tested. Assuming that only the responsivity R changes with temperature (Equation 3.5), the ratio $V_{\mathrm{DUT}}V_{\mathrm{REF}}^{-1}$ can be expressed by Equation 3.6.

$$R = mT_{\mathrm{DUT}} + n. \tag{3.5}$$

$$\frac{V_{\mathrm{DUT}}}{V_{\mathrm{REF}}} = KR = K(mT_{\mathrm{DUT}} + n). \tag{3.6}$$

Figure 3.14: Picture of one of the two PC50-7 samples tested in STELA. The PC50-7 is a silicon photodiode frequently used in experiments at the AEI.

K represents all constant factors involved, including the ratio between the optical powers on the photodiodes and the ratio between the TIA gains. Km and Kn can be obtained from a linear fit to the curve in Figure 3.13. The ratio mn^{-1} can be calculated from the fitted values. The ratio mn^{-1} obtained was 0.0157 for both samples, which indicates a temperature coefficient of $1.57\,\%\,°\mathrm{C}^{-1}$ of the responsivity R when normalized by $R(T = 0)$. An absolute calibration of the photodiode responsivity R can be obtained with a single measurement of the optical power on the DUT and the generated photocurrent. The measurement is performed at a fixed T_{DUT}. A NOVA II powermeter (OPHIR) was used to measure the absolute optical power on the DUT. The beam was well within the active area of the DUT and the powermeter head, avoiding clipping. The photocurrent can be obtained dividing V_{DUT} by the TIA gain. The absolute responsivity obtained for the PC50-7 is given in Equation 3.7. The temperature coefficient of the responsivity is $3.3 \times 10^{-3}\,\mathrm{A\,W^{-1}\,°C^{-1}}$.

$$\begin{aligned} R &= 0.0033 T_{\mathrm{DUT}} + 0.21, \\ [R] &= \mathrm{A\,W^{-1}}. \end{aligned} \tag{3.7}$$

3.3 Noise and bandwidth characterization

This section focuses on the main techniques used to experimentally measure the photoreceiver noise and bandwidth. In Section 1.6.4, the influence of these parameters in the final interferometer sensitivity was discussed. The first technique described below is sometimes called the white light method. The idea is to use a shot-noise-limited light source (i.e. with a white amplitude spectrum) to generate a predictable amount of noise. By measuring the total noise with and without the introduced shot noise, the photoreceiver electronic noise $\tilde{\imath}_{\mathrm{en}}$ can be derived.

The following equations can also be found in [77, p. 4]. Without illumination, the voltage noise at the photoreceiver output $\tilde{v}_{\mathrm{en}}$ is defined in Equation 3.8.

$$\tilde{v}_{\mathrm{en}} = G_{\mathrm{TIA}}\tilde{\imath}_{\mathrm{en}}, \tag{3.8}$$

where G_{TIA} is the TIA gain, which is another way to define the magnitude of the TIA frequency response shown in Figure 2.6 and described by Equation 2.11 for an OpAmp-based TIA. G_{TIA} is in general difficult to measure. $\tilde{\imath}_{\mathrm{en}}$ is the equivalent current noise at the input of the photoreceiver, which is the noise magnitude of interest (see Equation 1.19). Equation 3.9 defines the shot noise in terms of the generated DC photocurrent I_{DC}.

$$\tilde{\imath}_{\mathrm{sn}} = (2qI_{\mathrm{DC}})^{1/2}, \tag{3.9}$$

where q is the charge of an electron. The measured output voltage noise in the presence of shot noise $\tilde{v}_{\mathrm{n}}$ is given Equation 3.11

$$\tilde{v}_{\mathrm{n}} = G_{\mathrm{TIA}}(\tilde{\imath}_{\mathrm{sn}}^2 + \tilde{\imath}_{\mathrm{en}}^2)^{1/2}. \tag{3.10}$$

Dividing Equation 3.11 by Equation 3.8, we obtain:

$$\frac{\tilde{v}_{\mathrm{n}}}{\tilde{v}_{\mathrm{en}}} = \frac{G_{\mathrm{TIA}}(\tilde{\imath}_{\mathrm{sn}}^2 + \tilde{\imath}_{\mathrm{en}}^2)^{1/2}}{G_{\mathrm{TIA}}\tilde{\imath}_{\mathrm{en}}}. \tag{3.11}$$

Solving for $\tilde{\imath}_{\mathrm{en}}$ leads to Equation 3.12.

$$\tilde{\imath}_{\mathrm{en}} = \frac{\tilde{\imath}_{\mathrm{sn}}}{\left(\left(\frac{\tilde{v}_{\mathrm{n}}}{\tilde{v}_{\mathrm{en}}}\right)^2 - 1\right)^{1/2}} = \frac{(2qI_{\mathrm{DC}})^{1/2}}{\left(\left(\frac{\tilde{v}_{\mathrm{n}}}{\tilde{v}_{\mathrm{en}}}\right)^2 - 1\right)^{1/2}}, \tag{3.12}$$

where $I_{\mathrm{DC}} = V_{\mathrm{DC}}R_F^{-1}$. V_{DC} denotes the DC output voltage and R_F denotes the TIA gain at DC, normally set by a well-known feedback resistor. With this method, the electronic noise of the photoreceiver $\tilde{\imath}_{\mathrm{en}}$ can be obtained with two measurements of the photoreceiver output voltage noise, with and without illumination ($\tilde{v}_{\mathrm{n}}$, $\tilde{v}_{\mathrm{en}}$), and a measurement of the DC output voltage. There is no need to know the TIA gain over frequency since it cancels out in the process. Once the electronic noise $\tilde{\imath}_{\mathrm{en}}$ is obtained, the TIA gain can be easily calculated using Equation 3.13.

$$G_{\mathrm{TIA}} = \frac{\tilde{v}_{\mathrm{en}}}{\tilde{\imath}_{\mathrm{en}}}. \tag{3.13}$$

The actual measurement of $\tilde{v}_{\mathrm{n}}$ and $\tilde{v}_{\mathrm{en}}$ can be performed using a spectrum analyzer, which directly provides the spectral densities of the input signals. The voltage can also be sampled using a sufficiently fast ADC, and the spectral density can be calculated in post-processing. The latter option was the baseline of a measurement setup designed to automate the calculation of $\tilde{\imath}_{\mathrm{en}}$. The setup is shown in Figure 3.15. Both photoreceiver

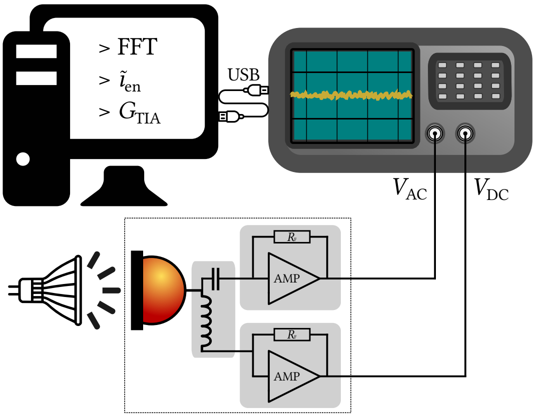

Figure 3.15: Setup diagram for photoreceiver characterization with the white light method. Both photoreceiver outputs (DC and AC) are connected to an oscilloscope. The oscilloscope features a fast ADC to sample the AC signal at the MHz range. A PC, connected to the oscilloscope via USB, commands the measurements and extracts the sampled data from the oscilloscope internal memory. The voltage noise spectral densities $\tilde{v}_{\mathrm{n}}$ and $\tilde{v}_{\mathrm{en}}$ are calculated applying the Welch's FFT method [98]. The input current noise $\tilde{i}_{\mathrm{en}}$ and the TIA gain G_{TIA} can be obtained using $\tilde{v}_{\mathrm{n}}$, $\tilde{v}_{\mathrm{en}}$ and the DC output voltage under illumination.

outputs (DC and AC) are connected to an oscilloscope. The oscilloscope must feature a fast ADC to correctly sample the AC input signal at the MHz range and it also needs a sufficiently large internal memory to store the sampled values. A PC, connected via USB to the oscilloscope, commands the measurements and extracts the sampled data. This is performed using a Python-based script that can be found in the Appendix. Once the sampled data from the two measurements (with and without illumination) is transferred to the PC, the Welch's FFT method [98] is used to calculate the voltage spectral densities. Using the voltage spectral densities $\tilde{v}_{\mathrm{n}}$ and $\tilde{v}_{\mathrm{en}}$ and the DC output voltage under illumination, the input current noise $\tilde{i}_{\mathrm{en}}$ and the TIA gain G_{TIA} can be obtained.

The white light technique is very convenient for the measurement of the photoreceiver noise and bandwidth, but it presents two major drawbacks:

- It is not possible to extract information about the TIA phase response.
- The transimpedance gain G_{TIA} does not include the photodetector frequency response. Bandwidth limitations imposed by silicon photodiodes in the MHz range [68, p. 82] would not be observable with the white light method.

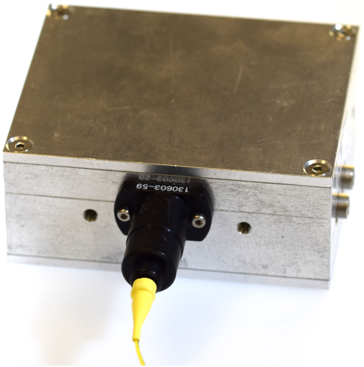

Figure 3.16: Picture of the fiber-pigtailed laser diode with its custom-made driver electronics. The circuit diagram of the driver can be found in the Appendix. An external RF signal can modulate the laser diode pump current, obtaining an AC-modulated light source. This device was used to test the TIA electronics of Figure 3.17.

Measuring the frequency response of the photoreceiver with an AC-modulated light source can solve these two issues. The light source must be fast, having a flat magnitude and phase response within the frequency range of the photoreceiver tested. A laser diode driver was created in the frame of this thesis for this purpose. A picture of the laser diode driver is shown in Figure 3.16. The driver is based on an earlier design from Gerhard Heinzel. The circuit diagram can be found in the Appendix (Figure 4.1). The driver pumps current into a fiber-pigtailed laser diode (LPS-1060-FC from Thorlabs), and this current can be modulated using an external radio frequency (RF) signal. An optical frequency response can be obtained from the ratio between the photoreceiver AC output V_{AC} and a swept-frequency signal modulating the laser diode current. The laser diode driver from Figure 3.16 provides a voltage output with a linear relation to the laser diode pump current that can be used to obtain the optical frequency response. This response inevitably includes the electrical-to-optical efficiency of the laser diode and losses along the optical path. For that reason, the magnitude of the optical frequency response cannot be used as an absolute reference and provides information only about relative changes over frequency.

The laser diode and driver electronics described above were used to measure the optical frequency response of a 16-channel TIA design built in the frame of this thesis to support the LISA optical bench (LOB) [41] [99] experiments and the advanced tilt Actuator (ATA) [100]. A picture of the implemented design can be seen in Figure 3.17. The circuit diagram and the printed circuit board (PCB) layout can be found in the Appendix. A silicon photodiode PC50-7, whose thermal-stability was measured in Section 3.2, was used as photodetector. A reverse bias voltage of 5 V was applied to the

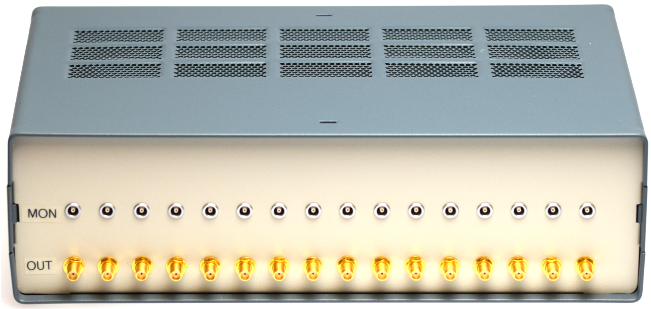

Figure 3.17: Picture of a 16-channel TIA design for the LOB and ATA experiments. The circuit diagram and PCB layout can be found in the Appendix. The frequency response of the TIA in combination with a PC50-7 silicon photodiode is shown in Figure 3.18.

photodiode.

Figure 3.18 shows the optical frequency response of a single channel of the full photoreceiver (photodiode and TIA). The same behavior was observed for all other channels. The magnitude of the frequency response starts decreasing at 10 kHz with no significant change in the phase response. This behavior was already observed by [68, p. 82] when using a silicon photodiode with a bias voltage below (100 V). The effect was attributed to the transit-time of electrons in the semiconductor, although an in-depth analysis is needed. The early drop in the magnitude frequency response starting at 10 kHz would not be observable with the white light method described at the beginning of the section.

In an ideal case, the photoreceiver performance should be tested under the expected LISA conditions and within the full metrology chain, together with other key components. For that purpose, an optical testbed based on an ultra-stable hexagonal optical bench has been implemented at the AEI. Figure 3.19 shows a picture of the core of the testbed. Three heterodyne beat-notes with a zero phase combination are generated on the bench, corresponding to the violet, light blue and yellow beams. The optical signals are detected by the photoreceivers, and their phases are extracted by the phasemeter to get an estimate of the full chain performance. The zero phase combination of the three signals can reveal non-linearities in the metrology chain. [101].

At the moment, the power of the interfered signals is of the order of mW. Therefore, they do not completely replicate the low power conditions of intersatellite laser interferometry. First, the priority is to reduce the noise floor of the system until reaching the expected performance for the LISA metrology chain. Once this milestone is achieved with mW signals, the power of one of the interfered beams can be decreased to the level of pW. In this fashion, the noise contribution of the photoreceivers can be properly tested (Equation 1.14).

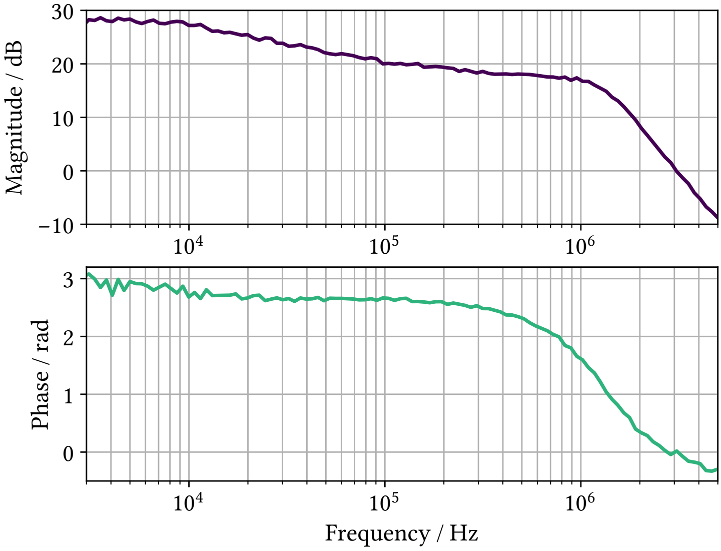

Figure 3.18: Single channel optical frequency response of the 16-channel TIA design for the LOB and ATA experiments. The PD50-7 silicon photodiode was used as photodetector with a reverse bias of 5 V. The early drop in the magnitude frequency response starting at 10 kHz was already observed in silicon photodiodes [68, p. 82]. This effect, attributed to the transit-time of electrons in the semiconductor, cannot be observed with the white light method. This measurement was performed with an AC-modulated laser diode (Figure 3.16).

3.4 The GRACE-FO photoreceiver

This section describes the experimental characterization of the photoreceiver flight models for GRACE-FO. Part of the contents of this section are already published in Optics Express [47]. The DLR in Berlin, in collaboration with the AEI, designed and built a set of photoreceivers, which are part of the GRACE-FO LRI. The topology of the LRI readout chain is equivalent to that shown in Figure 1.8. For the photoreceiver, a 1 mm diameter InGaAs QPD (FCIQ1000 from OEC GmbH) was chosen as photodetector. The spatially resolved profile of the FCIQ1000 was studied in Section 3.1.2. The circuit diagram of the actual TIA implementation can be seen in Figure 3.20. The current from the reverse-biased photodiode (V_{bias} = 5 V) splits into an AC (main interferometer signal) and a DC path. Two OpAmp-based TIAs, featuring the LMH6624 (AC) and the OP284 (DC), convert the current into voltage (V_{AC}, V_{DC}).

The GRACE-FO photoreceivers are used in pairs, detecting the interfered beams at

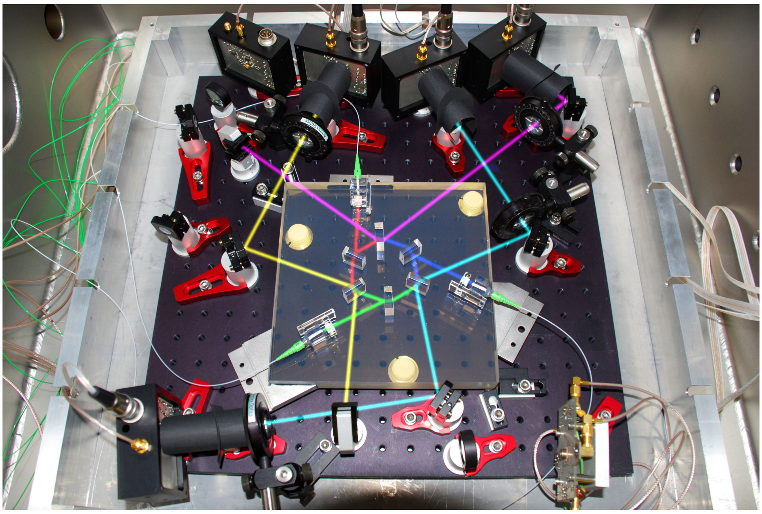

Figure 3.19: Picture of the hexagonal interferometer testbed. Three heterodyne beat-notes with a zero phase combination are generated on the bench, corresponding to the violet, light blue and yellow beams. The optical signals are detected by the photoreceivers, and their phases are extracted by the phasemeter to get an estimate of the full chain performance. The three-signal combination can reveal non-linearities. Once performance is achieved using mW signals, optical powers in the pW range can be used to test the noise contribution of the photoreceiver. Credit: Daniel Penkert.

the two output ports of the recombining beam splitter. This topology was described in Section 1.6.4 and in the GRACE-FO nomenclature it is defined as hot redundancy. Each of the two photoreceivers is defined as photoreceiver front-end (PRF), which contains a QPD and the corresponding TIAs. Both PRFs share a common photoreceiver back-end (PRB), which includes a summing amplifier and the AAF. The block diagram of this configuration is shown in Figure 3.21. The two (identical) beat-notes produced in the interferometer arrive at both PRFs and their output voltages are combined in the summing amplifier of the PRB prior the AAF. The topology is essentially the same for the DC and the AC paths, differing in the OpAmp used for the summing amplifier (LT1498 for DC and AD8001 for AC).

3.4.1 Radiation hardness

Environmental conditions in outer space are not ideal for electronic components. They can suffer damage and eventual failures produced by radiation of diverse origin, such as:

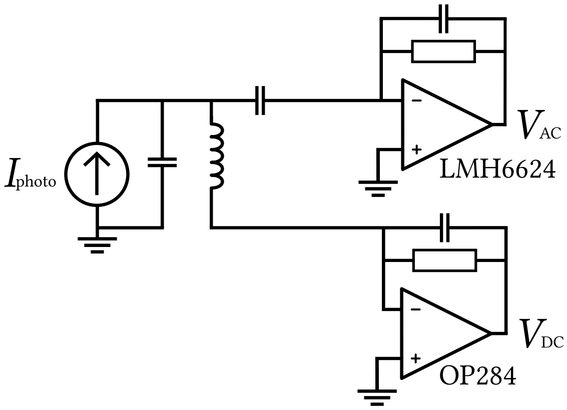

Figure 3.20: Electrical diagram of the TIA from the GRACE-FO photoreceiver. The current from the reverse-biased photodiode (V_{bias} = 5 V) splits into an AC (main signal) and a DC path. Two OpAmp-based TIAs, featuring the LMH6624 (AC) and the OP284 (DC), convert the current into voltage ($V_{\text{AC}}, V_{\text{DC}}$).

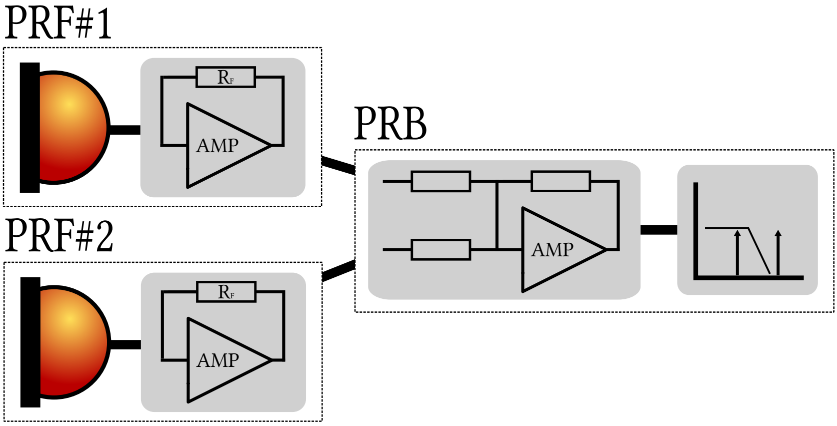

Figure 3.21: Block diagram of the GRACE-FO photoreceiver: two PRFs with independent QPDs and TIAs, sharing a common PRB, which includes a summing amplifier and the AAF. This configuration is known as hot redundancy in the GRACE-FO project, and is equivalent to the balanced detection configuration described in Section 1.6.4. The topology is essentially the same for the DC and the AC paths, differing in the OpAmp used for the summing amplifier (LT1498 for DC and AD8001 for AC).

- Cosmic rays coming from all directions in the sky
- Solar particle events coming from the Sun
- Van Allen radiation belts around the Earth

The amount of radiation from each source depends on the location of the spacecraft during the mission. The electrons, protons, neutrons, alpha particles and heavy ions from these sources can modify the structure of the electronics in single, highly energetic events, or by the cumulative dose from less energetic radiation. The effects in the semiconductor material include lattice displacement, trapped holes and stripped electrons. In bipolar devices like QPDs or the TIA electronics in a photoreceiver, the radiation-induced changes in the semiconductor material can increase leakage currents, degrade gain and reduce the efficiency of photodetectors [102]. For example, high radiation levels in the Van Allen belts quickly eroded the efficiency of the Engineering Test Satellite - 6 (ETS-6) solar panels, greatly reducing the mission lifetime. [103]

For the reasons mentioned above, non-space-qualified electronics for the GRACE-FO photoreceivers were intensively tested in terms of radiation hardness. The GRACE-FO spacecraft will follow a polar orbit at an altitude between 425 km to 500 km above the Earth. The GRACE-FO satellites will suffer from radiation, particularly from the Van Allen belts. The expected total ionizing dose for the GRACE-FO photoreceiver is 16 Gy, with an expected displacement damage equivalent fluence of 1.52×10^{10} protons cm^{-2} with a proton energy of MeV. These amounts are obtained considering the orbits, radiation models, satellite structure and mission duration.

The components tested include the OpAmp for the AC TIA (LMH6624) and the QPD (FCIQ1000). A safety margin of 2 is used during the radiation hardness test for both the total ionizing dose and the displacement damage equivalent fluence. A Cobalt60 gamma source produced a total ionization dose with energies of 1.17 MeV and 1.33 MeV. For the displacement damage equivalent fluence, a cyclotron produced up to 3.14×10^{10} protons cm^{-2} with a proton energy above 35 MeV.

The LMH6624 samples tested did not show any significant variation in the offset current, offset voltage or quiescent current. The FCIQ1000 QPDs showed no significant changes in their dark current, junction capacitance or responsivity. The test validated the non-irradiated samples from the same badge for use as flight components.

3.4.2 Noise and bandwidth

The white light source method explained in Section 3.3 was used to obtain the photoreceiver input current noise $\tilde{\imath}_{\mathrm{en}}$ and bandwidth of the GRACE-FO flight models. Figure 3.22 presents a representative example of $\tilde{\imath}_{\mathrm{en}}$ for a single channel in cold redundancy. The measured noise steadily increases over frequency, since the OpAmp voltage noise contribution $\tilde{e}_{\mathrm{n}}$ dominates (Equation 2.14). The mission requirement for a single segment in cold redundancy is 5 pA $\mathrm{Hz}^{-1/2}$ at 16 MHz. The value obtained at that frequency

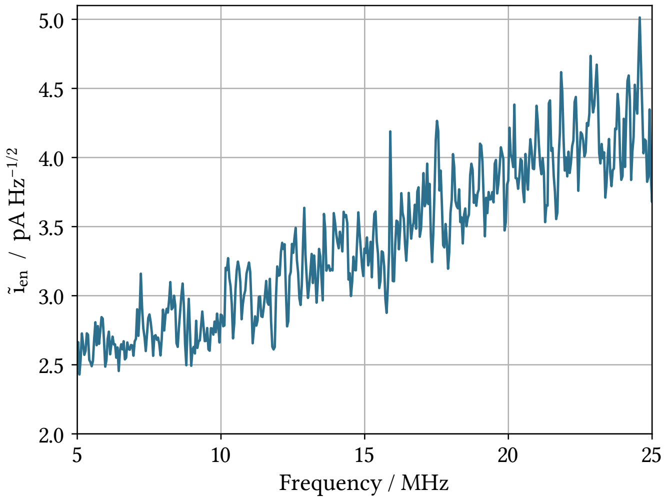

Figure 3.22: Input noise density $\tilde{\imath}_{\mathrm{en}}$ for a single channel, measured using cold redundancy (only one PRF). The requirement for GRACE-FO in this configuration is 5 pA Hz$^{-1/2}$ at 16 MHz. The value obtained is around 3.5 pA Hz$^{-1/2}$, fulfilling the requirement. The measurement was repeated for all channels of all PRFs obtaining similar results.

is around 3.5 pA Hz$^{-1/2}$, which fulfills the requirement. The measurement was repeated for all channels of all PRFs obtaining similar results.

The gain and bandwidth of the photoreceiver was also measured using the white light method. The total transimpedance gain is obtained by concatenating a TIA, a non-inverting amplifier (both in the PRF) and an adjustable-gain voltage amplifier in the PRB. This amplifier chain had to provide a variable amplification from 0.62 MΩ to 2.06 MΩ in a frequency band from 4 MHz to 16 MHz when operating in hot redundancy. Figure 3.23 shows the total transimpedance gain over frequency for the expected GRACE-FO heterodyne range, using the minimum and maximum variable gain settings. The photoreceiver was designed to exceed the expected range, clearly fulfilling the requirement on both ends, with a gain of about 0.15 MΩ for a minimum gain and 6 MΩ for the maximum gain.

3.4.3 Phase thermal stability

In May 2015, the GRACE-FO photoreceiver flight hardware was tested in a TVAC in order to verify correct operation in space conditions. The setup shown in Figure 3.24 was used for that purpose. The full photoreceiver (PRFs and PRB) was placed inside

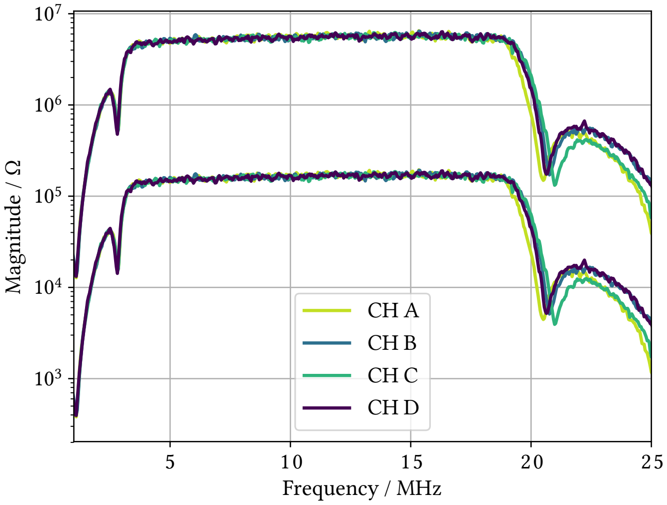

Figure 3.23: Magnitude of the frequency response (transimpedance gain) of a representative GRACE-FO photoreceiver flight model. The measurement shows all four channels for the minimum and maximum gain settings when operating in hot redundancy. The TIA gain, ranging from 0.15 MΩ to 6 MΩ at the desired heterodyne frequency range, fulfills the mission requirements.

the TVAC, together with infrared light emitting diodes (LEDs) whose purpose was the simulation of beat-notes on the PRFs. The optical power produced by each LED reaching the photodiode was of the order of 100 µW. The LEDs were amplitude-modulated from the outside using a frequency sweep from 4 MHz to 16 MHz, which is the nominal frequency range for the GRACE-FO photoreceivers. Outside the tank, the photoreceiver signals phases from the different channels $\phi_X = \{\phi_\mathrm{A}, \phi_\mathrm{B}, \phi_\mathrm{C}, \phi_\mathrm{D}\}$ were measured against the reference signal from the LED driver source ϕ_REF. The TVAC temperature changed during the test with a nominal range between −10 °C to 60 °C for the PRFs and between −15 °C to 55 °C for the PRB. The real temperature of the PRB, the most temperature sensitive element of the photoreceiver due to the AAF, was sensed during the test by a PT1000 resistance temperature detector (RTD) inside the unit. Using this temperature and the phasemeter data, the temperature coefficients that define the thermally induced phase noise in the photoreceivers were experimentally measured.

A picture of all 3 photoreceiver flight models prior to the TVAC test can be seen in Figure 3.25. The three PRBs are placed on the upper baseplate and the six PRFs (only 3 visible) on the lower baseplate. The LEDs were mounted underneath the PRFs.

As mentioned in Section 1.6.2, the segmented nature of the QPD used in the pho-

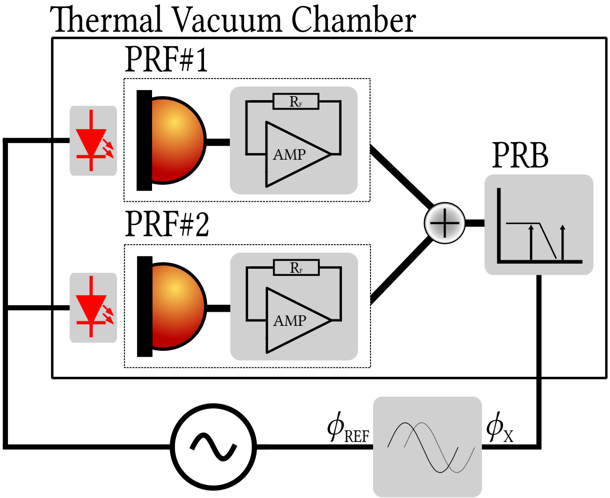

Figure 3.24: Block diagram of the setup used during the TVAC test. The full photoreceiver (PRF and PRB) was placed inside the TVAC, together with infrared LEDs for beat-note simulation. The LEDs were amplitude-modulated using a frequency sweep between 4 MHz to 16 MHz. The photoreceiver signals' phases $\phi_X = \{\phi_{\mathrm{A}}, \phi_{\mathrm{B}}, \phi_{\mathrm{C}}, \phi_{\mathrm{D}}\}$ were measured against the reference signal from the LED driver source ϕ_{REF}. With this setup, the temperature coefficient that defines the thermally induced noise of the photoreceiver output phase was experimentally measured.

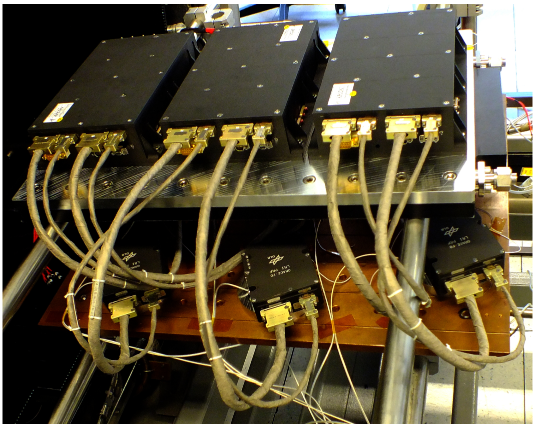

Figure 3.25: A picture of all 3 photoreceiver flight models prior to the TVAC test. The three PRB are placed on the top baseplate and the six PRFs (only 3 visible) on the lower baseplate. The LEDs were mounted underneath the PRFs.

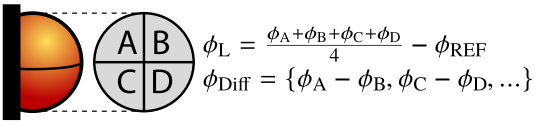
A
B
C
D
$\phi_L = \frac{\phi_A+\phi_B+\phi_C+\phi_D}{4} - \phi_{REF}$
$\phi_{Diff} = \{\phi_A - \phi_B, \phi_C - \phi_D, \ldots\}$

Figure 3.26: Diagram with the relation between the different quadrants and the longitudinal and differential phases. The main longitudinal phase ϕ_L is an average of the 4 different channels measured against the reference phase ϕ_{REF}. The differential phase between the channels ϕ_{Diff} is needed to derive the angular misalignment between the interfered beams.

toreceiver provides four different signals to simultaneously detect longitudinal displacements and angular misalignments between the two interfering beams. Since the four photoreceiver signals were tracked independently by the phasemeter, the phase stability over temperature could be obtained for the main longitudinal measurand ϕ_L and also for all differential phase combinations needed to derive the angular misalignment (E.g. $\phi_A - \phi_B$). Figure 3.26 shows a diagram with the relation between the different quadrants and the longitudinal and differential phases.

Figure 3.27 shows a representative example of the longitudinal phase stability obtained during the TVAC test (from flight model #1). The longitudinal phase ϕ_L was recorded for a total of 61 PRB temperatures (between −6.4 °C to 63.2 °C) at each 1 kHz-frequency bin from 4 MHz to 16 MHz. The plot on the left shows ϕ_L for the minimum and maximum temperatures. Since the results showed a mostly linear dependence of ϕ_L on temperature, a linear fit was performed to obtain the temperature coefficient ϕ_{LT} plotted on the right. There is an expected loss of phase over frequency due to the TIA and the AAF, increased by the low pass filtering from the meter-length cables used during the test. The maximum temperature coefficient ϕ_{LT} obtained (in absolute terms) is about $-5\,\mathrm{mrad\,K^{-1}}$ at 16 MHz. This is not exactly the coefficient from the photoreceiver, since the LED source has also a temperature coefficient of about $-2.5\,\mathrm{mrad\,K^{-1}}$ at 16 MHz, therefore with same sign. The LEDs were placed inside the tank and had a temperature profile similar to the PRFs. The value measured is nonetheless suitable as an upper limit for the longitudinal phase stability. Additionally, even if the photoreceiver was operated in hot redundancy, the major contribution to ϕ_{LT} comes from the PRB, making the measured value suitable for noise budget calculations in cold redundancy (one PRF) and for comparison to the requirement ($25\,\mathrm{mrad\,K^{-1}}$).

Figure 3.28 shows a representative example of the differential phase stability obtained during the TVAC test ($\phi_A - \phi_D$ of photoreceiver flight model #1). In the same way as for ϕ_L, the differential phase ϕ_{Diff} is plotted on the left for the minimum and maximum PRB temperatures measured during the test. A mostly linear dependence of ϕ_{Diff} on temperature was observed. Therefore, a linear fit provided again the temperature coefficient ϕ_{DiffT} plotted on the right. Since the differential phase does not require the use of a phase reference, the temperature coefficient of the LED does not affect the result. The maximum ϕ_{DiffT} obtained (in absolute terms) is about $-100\,\mu\mathrm{rad\,K^{-1}}$, 2 orders of magnitude below the $10\,\mathrm{mrad\,K^{-1}}$ requirement from GRACE-FO.

With the measured parameters of the GRACE-FO flight models presented along this section, a photoreceiver noise budget, such as the one presented for LISA in Figure 1.13, can be obtained. Figure 3.29 shows the phase noise budget using the measured photoreceiver performance and the expected interferometer parameters in GRACE-FO. These values are listed in Table 3.1. The calculations used to obtain the phase noise from those values are explained in Section 1.6.4, with the only difference being that in GRACE-FO there are 2 photoreceivers in the interferometer. That yields a total of 8 photoreceiver channels, as opposed to the 16 channels of LISA. The phase noise budget is shot-noise-limited at $60\,\mu\mathrm{rad\,Hz^{-1/2}}$ down to almost 0.3 mHz, where the thermally induced phase noise begins to dominate. The blue curve shows the top-level noise requirement for the LRI $\tilde{\phi}_{\mathrm{LRI}}$, which needs to be fulfilled from 2 mHz to 0.1 Hz (solid line), but was extended in this plot (dashed line) for comparison with the photoreceiver phase noise. The flat part of $\tilde{\phi}_{\mathrm{LRI}}$ corresponds to $80\,\mathrm{nm\,Hz^{-1/2}}$ of displacement noise, and it is dominated by laser frequency noise and tilt-to-length coupling driven by pointing jitter [10]. The photoreceiver contribution is at least 4 orders of magnitude below the LRI requirement $\tilde{\phi}_{\mathrm{LRI}}$.

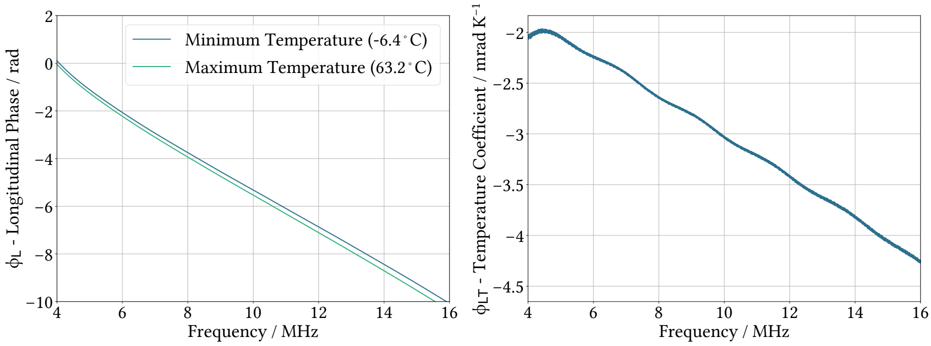

Figure 3.27: Representative example of the longitudinal phase stability obtained during the TVAC test (from flight model #1). The plot on the left shows ϕ_L for the minimum and maximum PRB temperatures. Since the results showed a mostly linear dependence of ϕ_L on temperature, a linear fit was performed to obtain the temperature coefficient ϕ_LT plotted on the right. The maximum ϕ_LT obtained (in absolute terms) is below $-5\,\mathrm{mrad\,K^{-1}}$ at 16 MHz. The requirement of $25\,\mathrm{mrad\,K^{-1}}$ is fulfilled.

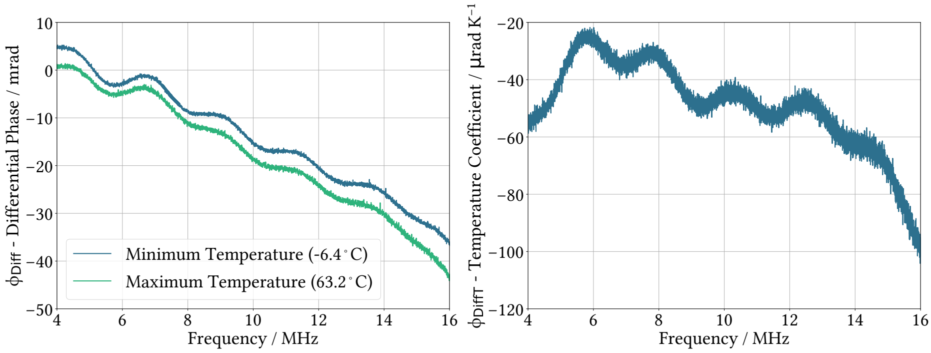

Figure 3.28: Representative example of the differential phase stability ($\phi_\mathrm{A} - \phi_\mathrm{D}$ of photoreceiver flight model #1). The differential phase ϕ_Diff is plotted on the left for the minimum and maximum PRB temperatures. The temperature coefficient ϕ_DiffT is plotted on the right. The maximum temperature coefficient obtained in absolute terms is about $-100\,\mathrm{\mu rad\,K^{-1}}$, 2 orders of magnitude below the $10\,\mathrm{mrad\,K^{-1}}$ requirement.

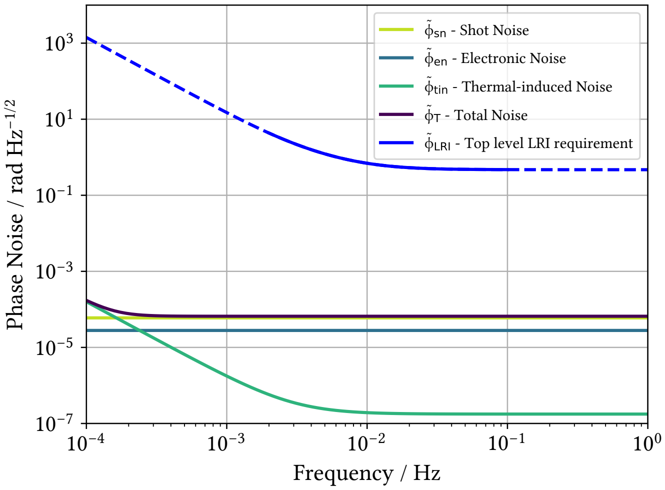

Figure 3.29: Phase noise budget using the measured photoreceiver performance and expected interferometer parameters in GRACE-FO. The calculations used to obtain the phase noise contributions were explained in Section 1.6.4. The phase noise budget is shot-noise-limited at 60 µrad Hz$^{-1/2}$. The blue curve shows the top-level noise requirement for the LRI $\tilde{\phi}_{\mathrm{LRI}}$. The photoreceiver noise is at least 4 orders of magnitude below $\tilde{\phi}_{\mathrm{LRI}}$. The LRI noise is dominated by laser frequency noise and tilt-to-length coupling driven by pointing jitter [10].

Table 3.1: Photoreceiver and interferometer parameters in GRACE-FO. The phase noise budget of Figure 3.29 is based on these values. A detailed description of the parameters and their impact on the interferometer noise budget can be found in Section 1.6.4. T_{PR} shows only the noise floor at 1 Hz for simplification. In reality, it increases towards low frequencies.

Local laser power	P_{LO}	2	mW
Received power	P_{RX}	80	pW
Photodiode responsivity	R	0.7	A W^{-1}
Heterodyne efficiency	γ	0.8	1
Photoreceiver electronic noise	$\tilde{i}_{\mathrm{en}}$	3.5	pA Hz$^{-1/2}$
Temperature stability	T_{PR}	$10^{-4}*$	K Hz$^{-1/2}$
Longitudinal phase temperature coefficient	ϕ_{LT}	5×10^{-3}	rad K^{-1}

3.5 A photoreceiver for LISA based on discrete transistors

The development of low noise, high bandwidth LISA-like quadrant photoreceivers have been focused on using custom-designed, low capacitance quadrant photodiodes (QPDs) in combination with transimpedance amplifiers (TIAs) based on wideband, ultra-low noise operational amplifiers [65]. In a similar way, improvements in the noise performance of a MHz photoreceiver were achieved by lowering the effective capacitance of commercially available photodiodes via bootstrapping [66]. The latter option is not suitable for standard QPDs due to their common-cathode configuration. As opposed to previous methods, the photoreceiver design presented in this section focuses on reducing the noise of the TIA electronics. These results are published in IEEE Sensors [104].

The most critical part of the photoreceiver in terms of electronic noise and bandwidth is the first stage of the TIA, as discussed in Section 2.2. Although bipolar-based OpAmps used in previous designs [65][77] have remarkable noise properties, the need for low $\tilde{\imath}_\mathrm{n}$, low $\tilde{e}_\mathrm{n}$ and low power consumption makes discrete HBTs an attractive solution for the TIA first stage, as discussed in Section 2.2.4.

The BFP842ESD is an HBT from Infineon Technologies based on silicon, germanium and carbon (SiGe:C), designed for mobile communication low-noise amplifiers [105]. It was chosen as the core element of a photoreceiver TIA featuring discrete transistors. Using a theoretical estimation based on datasheet values and SPICE model parameters, the BFP842ESD has a voltage noise contribution $\tilde{e}_\mathrm{n} = 0.55\,\mathrm{nV\,Hz^{-1/2}}$ and a current noise contribution $\tilde{\imath}_\mathrm{n} = 1\,\mathrm{pA\,Hz^{-1/2}}$ at a collector current of 1 mA. The emitter base capacitance C_EB, which contributes to the amplifier input capacitance, is 0.44 pF. On the other hand, SPICE models do not always reflect the noise of the device at the specific conditions of the desired circuit. Models of the same device from different manufacturers can also present different noise parameters [106]. Additionally, the nominal specifications of a given component can differ from those of the actual device, as seen in the characterization of a LISA-like photoreceiver [77]. The results presented here rely on the experimental characterization of the photoreceiver performance.

Figure 3.30 shows the TIA of a single photoreceiver channel. The topology is based on an idea by Gerhard Heinzel. The current source with a capacitance in parallel represents the electrical model of a QPD segment. The photocurrent I_photo produced by the reverse-biased QPD ($V_\mathrm{bias} = 5\,\mathrm{V}$) splits into an AC (science signal) and a DC path. The BFP842ESD is used in a common emitter configuration as the first stage of the AC signal path. The first stage is the most critical, as the signal needs to be amplified without introducing excessive noise [74]. To this end, the resistors used to adjust the base voltage of the BFP842ESD (R_1 and R_2) were intentionally chosen to exhibit a high resistance in order to reduce their Johnson current noise contribution. Another discrete HBT (BFR181) follows the BFP842ESD in a cascode configuration, reducing the

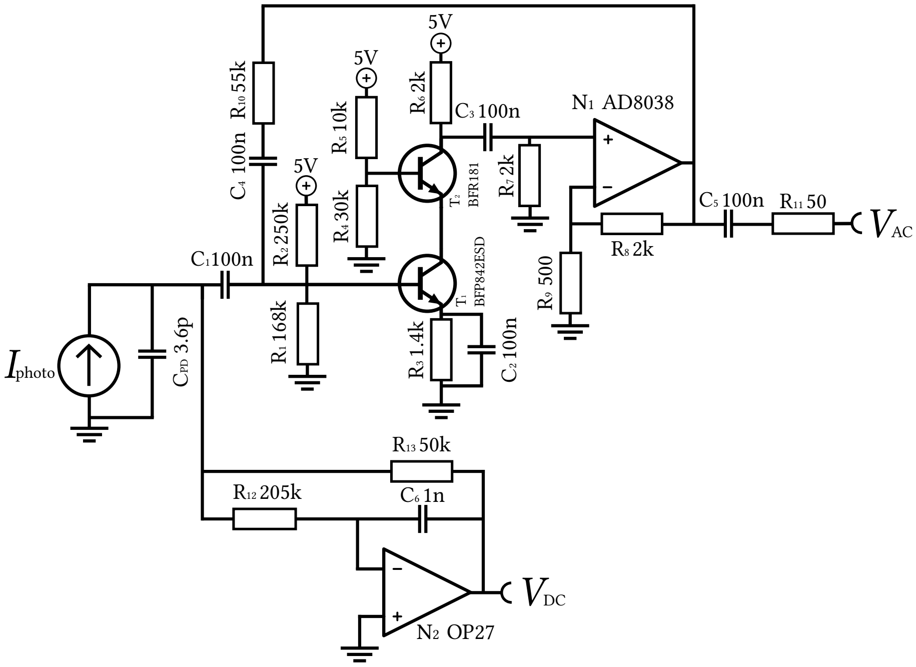
5V
5V
5V
R10 55k
C4 100n
R5 10k
R4 30k
R6 2k
C3 100n
N1 AD8038
R7 2k
T2 BFR181
T1 BFP842ESD
R2 250k
C1 100n
R1 168k
R3 1.4k
C2 100n
R9 500
R8 2k
C5 100n
R11 50
V_AC
I_photo
C_PD 3.6p
R13 50k
R12 205k
C6 1n
V_DC
N2 OP27

Figure 3.30: Schematic of the TIA of a single photoreceiver channel. The current source with a capacitance in parallel represents a QPD segment. The photocurrent splits into an AC and a DC path. The low noise HBT BFP842ESD is used in a common emitter configuration as the first stage of the AC path. R_1 and R_2 have intentionally high resistances to reduce their Johnson current noise contribution. A cascode structure and an additional low power non-inverting amplifier are used to maintain the bandwidth and increase the gain. The DC path features a standard OpAmp-based TIA (OP27).

Miller effect and maintaining a high bandwidth [84]. An OpAmp-based non-inverting amplifier connected to the cascode output is used to provide low output impedance and additional gain. The use of a non-inverting amplifier instead of an emitter follower voltage buffer (see Section 2.2.4) is the major difference with respect to previous discrete designs developed at the AEI [68, p. 87]. Due to the combination of discrete transistors with an OpAmp stage, this topology is also referred to as hybrid TIA. Since the noise performance of this second OpAmp stage is non-critical, the AD8038 from Analog Devices was selected due to its low power consumption (quiescent current I_Q = 1 mA) and high speed performance. Stability and a flat AC transimpedance gain were achieved by applying negative feedback from the AD8038 output to the BFP842ESD input (base).

For the DC path, a more standard OpAmp-based TIA is used to convert the DC component of the photocurrent. Since high frequency operation is not needed in this signal path, the common OP27 was selected. A 200 kΩ resistor (R_{12}) was used to isolate the OP27 output from the sensitive input node. These two nodes would otherwise be connected at high frequencies, when C_6 takes on a low impedance. The feedback resistor R_{13} sets the gain for the DC photocurrent. A drawback of this design is that R_{13} cannot be easily replaced by a different resistor without special care replacing also other components to avoid oscillations.

The LM7805 and LM7905 linear regulators provide ±5 V for the TIA supply and for the bias of the QPD. The noise of linear regulators is not critical at the required MHz heterodyne band, where photoreceiver electronic noise measurements are performed [107]. Bypass capacitors additionally filter residual high frequency noise from the supply lines.

All four channels of the photoreceiver feature the same values for all electronic components. The surface-mount resistors and capacitors used have a 1% and a 10% tolerance, respectively. The photoreceiver was built on a two-sided PCB. The layout follows standard RF design techniques. All components were placed on the bottom side, leaving the top layer of the PCB solely as a ground plane. Cutouts were performed on both sides of the PCB in areas surrounding the main signal path in order to avoid parasitic effects. Copper tracks were kept as short as possible to minimize unwanted delays. To avoid interruptions of the signal path or ground plane, the regulated ±5 V from the power supply were distributed using copper wires with a cross-sectional area of 0.2 mm^2. A set of 100 nF bypass capacitors were placed at the supply nodes to reduce the signal path to ground. Figure 3.31 is a picture of the bottom side of the populated PCB, where the QPD and all four TIAs are visible.

The QPD in Figure 3.31 is the GAP500Q from OEC GmbH, a 0.5 mm diameter InGaAs device. The measured junction capacitance (C_j) of the GAP500Q sample used was 3.6 pF per segment. This capacitance is comparable to the C_j = 2.5 pF of the 1 mm diameter InGaAs QPD developed by Discovery Semiconductors Inc used in [65] [77]. In general, larger area QPDs facilitate the alignment of components in an optical setup, but increase the noise (Equation 2.14) and decrease the bandwidth (Equation 2.11) of the photoreceiver due to the larger junction capacitance.

In order to measure the photoreceiver input current noise $\tilde{\imath}_\mathrm{en}$ and the transimpedance amplifier gain G_TIA, a shot-noise-limited light source (halogen lamp) was used as described in Section 3.3. For the readout and post-processing, the setup shown in Figure 3.15 was used. The output voltage noise of the photoreceiver is measured with different light levels, from which $\tilde{\imath}_\mathrm{en}$ can be derived. With the hybrid photoreceiver design, the voltage noise is measured at the output of the AC path. The DC output and the DC photocurrent gain (50 kΩ) are used to calculate the shot noise introduced by the halogen lamp.

The specific oscilloscope utilized to sample the voltage from the AC and the DC out-

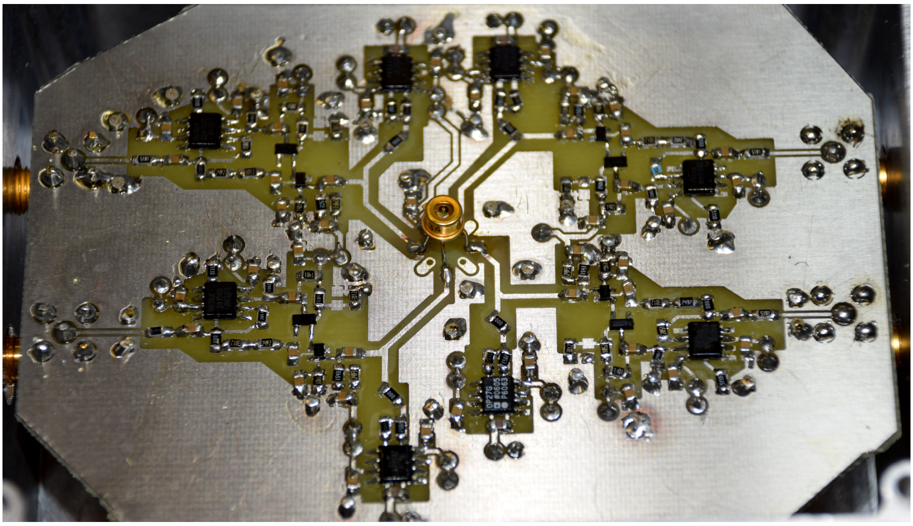

Figure 3.31: Picture of the implemented transistor-based photoreceiver. The QPD (GAP500Q from OEC GmbH) and all four TIAs are visible on the bottom side of the PCB. The layout follows standard RF design techniques, including a dedicated ground plane, selective cutouts on sensitive areas, short copper tracks and bypass capacitors.

puts was an Agilent Technologies MSO-X 4054A 5 GS s^{-1} oscilloscope. Once the data is digitized and transferred to a computer, the voltage noise spectral densities, obtained by the Welch's FFT method [98], are used together with the shot noise to calculate the input current noise density. Additionally, the gain of the TIA over frequency can be extracted in the process.

Figure 3.32 shows the input current noise $\tilde{\imath}_{\mathrm{en}}$ and the transimpedance amplifier gain G_{TIA} over frequency for one photoreceiver channel. The measurement was repeated with different transistor collector currents (I_{C}). The higher noise towards high frequencies indicates that the input current noise $\tilde{\imath}_{\mathrm{en}}$ above 20 MHz is dominated by the TIA voltage noise $\tilde{e}_{\mathrm{n}}$ component (see Equation 2.14). The input current noise $\tilde{\imath}_{\mathrm{en}}$ decreases with higher I_{C} at frequencies above 20 MHz, indicating a decrease in the voltage noise $\tilde{e}_{\mathrm{n}}$ (as described by Equation 2.17). The bandwidth of G_{TIA} also improves with increasing I_{C}. This is likely produced by an increase of the transition frequency f_{T} at the input transistors. The noise at 25 MHz, which is the maximum heterodyne frequency expected in LISA, reaches a minimum at $I_{\mathrm{C}} = 0.75$ mA. This limitation is probably due to the BFP842ESD base spreading resistance $r_{\mathrm{BB'}}$, as shown in Equation 2.17.

Figure 3.33 presents the input current noise and TIA gain over frequency of all four photoreceiver channels at a collector current $I_{\mathrm{C}} = 0.75$ mA. All channels exhibit a

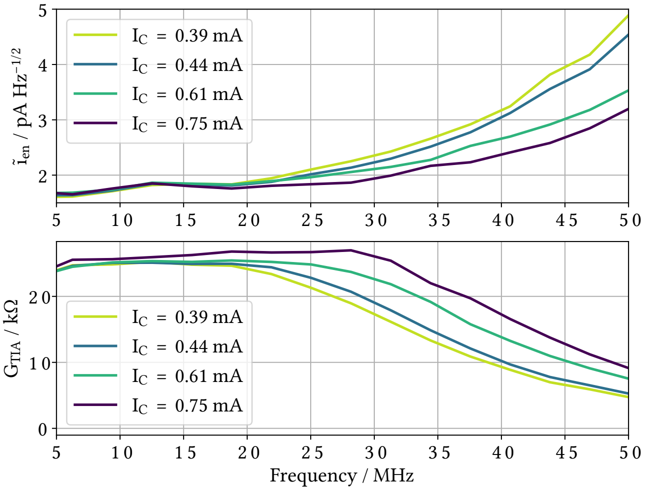

Figure 3.32: Input current noise $\tilde{\imath}_{\mathrm{en}}$ and transimpedance gain G_{TIA} over frequency from a single channel of the transistor-based photoreceiver. The measurement was repeated at different transistor collector currents (I_{C}). The input current noise decreases with higher I_{C} at frequencies above 20 MHz. The bandwidth of the TIA also improves with increasing I_{C}. The noise at 25 MHz, which is the maximum heterodyne frequency expected in LISA, reaches a minimum at $I_{\mathrm{C}} = 0.75$ mA. This limitation is probably caused by the transistor base spreading resistance $r_{\mathrm{BB}'}$.

similar behavior, with an input current noise of 1.7 pA Hz$^{-1/2}$ at 5 MHz, increasing to 1.9 pA Hz$^{-1/2}$ at 25 MHz, which is the maximum heterodyne frequency in LISA. The noise at 25 MHz is 0.2 pA Hz$^{-1/2}$ below the noise measured in a previous LISA-like photoreceiver featuring the same QPD [77]. This reduction of photoreceiver electronic noise translates to a 0.13 pm Hz$^{-1/2}$ decrease of its contribution to the LISA long-arm interferometer readout displacement noise. This value is obtained assuming the expected interferometer conditions in LISA and using Equation 1.19. The input current noise stays below 2 pA Hz$^{-1/2}$ up to 30 MHz, the same level obtained with the custom-made low capacitance InGaAs QPDs used in [65]. The photoreceivers in [65, 77] use the ultra-low noise, high bandwidth EL5135 operational amplifier from Intersil as the core of the TIA. The results shown in Figure 3.33 and discussed above demonstrate that the TIA based on HBTs surpasses the noise performance of the EL5135. The 3 dB bandwidth of G_{TIA} is 37 MHz. In order to study the impact of a larger photodiode junction capacitance on the transistor-based design, the GAP500Q was replaced by a 1 mm diameter InGaAs QPD: the GAP9119 from OEC GmbH (also called GAP1000Q). Figure 3.34 shows a comparison of the input current noise and bandwidth of a photoreceiver channel using both QPD models. The higher photodiode junction capacitance (C_j = 11.5 pF) magnifies the effect of the total impedance magnitude on the input current noise (see Equation 2.14). The input current noise stays below 3 pA $\mathrm{Hz}^{-1/2}$ at 25 MHz. The 3 dB bandwidth of G_TIA was determined to be 24 MHz. The higher photodiode capacitance reduces the G_TIA bandwidth due to its effect on the feedback network β (see Equation 2.11). The power consumption of the transistor-based photoreceiver was measured using the current flowing through the ±5 V supply lines. The value obtained was 178 mW, with the OP27 from the DC path being the largest contributor (quiescent current I_Q = 3 mA). This power consumption is possible thanks to the transistor-based AC input stage and the low power operational amplifiers at the DC stage and the second AC stage. Low noise, high bandwidth operational amplifiers used in previous designs are not optimized for low power consumption. For instance, the EL5135 has a nominal quiescent current of I_Q = 6.7 mA.

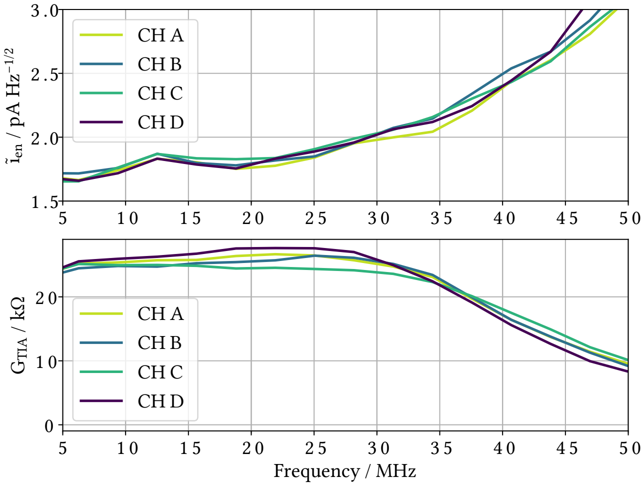

Figure 3.33: Input current noise $\tilde{\imath}_{\mathrm{en}}$ and transimpedance gain G_{TIA} from all four channels of the transistor-based photoreceiver, using a collector current I_C of 0.75 mA. All channels exhibit a similar behavior, with an input current noise of 1.7 pA Hz$^{-1/2}$ at 5 MHz, increasing to 1.9 pA Hz$^{-1/2}$ at 25 MHz, which is the maximum heterodyne frequency in LISA. The noise at 25 MHz is 0.2 pA Hz$^{-1/2}$ below the noise measured in a previous LISA-like photoreceiver featuring the same QPD [77]. The noise stays below 2 pA Hz$^{-1/2}$ up to 30 MHz. The 3 dB bandwidth of G_{TIA} is 37 MHz.

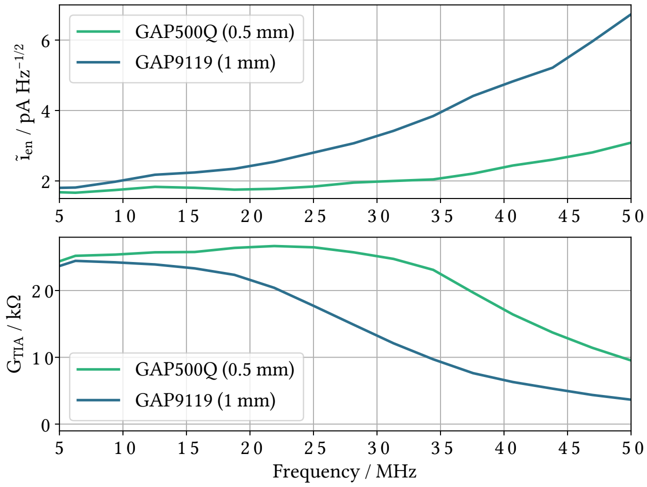

Figure 3.34: Comparison of the input current noise $\tilde{\imath}_{\mathrm{en}}$ and transimpedance gain G_{TIA} from a single channel of the transistor-based photoreceiver using a GAP500Q (C_j = 3.6 pF) and a GAP9119/GAP1000Q (C_j = 11.5 pF). The input current noise using the GAP9119 is higher but stays below 3 pA Hz$^{-1/2}$ at 25 MHz. The 3 dB bandwidth of G_{TIA} is 24 MHz.

4 | Summary and outlook

The main motivation for this thesis was the development of a photoreceiver for inter-satellite laser interferometers with better performance than previous designs [65][77] in terms of noise, bandwidth and power consumption. Analyzing the influence of these photoreceiver parameters on the interferometer sensitivity was a significant part of the thesis, in which the requirements for the photoreceiver were derived. In order to fulfill these requirements, different solutions for the photodetector and the amplifier electronics were considered. As a result, a photoreceiver prototype featuring discrete heterojunction bipolar transistors (HBTs) was designed, implemented and characterized. The thesis also contains the experimental characterization of the GRACE-FO photoreceiver flight hardware, and other properties of photodiodes such as spatial response and the temperature coefficient of the responsivity.

Chapter 1 set the framework of the thesis, describing the operation of an inter-satellite laser interferometer conceived to detect gravitational waves or measure time-variations of the Earth's gravity field. The chapter introduced the basics of heterodyne interferometry and photodetection, as well as the main interferometer subsystems in LISA. The last section of the chapter contains a breakdown of the LISA noise budget and the implications for the photoreceiver requirements. Orbital dynamics in LISA require a photoreceiver with a bandwidth higher than 25 MHz. The displacement noise contribution must be less than $2.2\,\mathrm{pm\,Hz^{-1/2}}$. This amount of displacement noise corresponds to an equivalent input current noise $\tilde{\imath}_{\mathrm{en}}$ of $3.5\,\mathrm{pA\,Hz^{-1/2}}$, using the expected interferometer parameters of the last LISA study for the calculation. The power consumption of the photoreceiver front-end, containing the quadrant photodiode and the corresponding TIAs, must be below 500 mW. These requirements were extracted from a rather conservative mission design, meaning that improvements in the photoreceiver are plausible and would be beneficial for the final observatory sensitivity.

Different technologies for the photodetector and the TIA electronics were studied in Chapter 2, in order to find an optimal solution given the photoreceiver requirements illustrated in Chapter 1. Semiconductor-based QPDs featuring a ternary alloy of InGaAs were identified as the best type of detector. They can be etched in a segmented structure, have a high responsivity at 1064 nm ($\sim 0.7\,\mathrm{A\,W^{-1}}$), operate at a low bias voltage

($\sim 5\,\mathrm{V}$), and are able to detect optical power beat-notes in the MHz regime. The junction capacitance C_j represents the major drawback of InGaAs-based devices, which can be compensated for by using wider intrinsic regions in the internal photodiode structure. New types of detectors based on 2D materials, such as graphene, are still far from reaching the performance of traditional InGaAs QPDs. As for the TIA, bipolar electronics are preferred. The lower equivalent voltage noise $\tilde{e}_n$ of this technology compared to FET devices translates into lower input current noise at high heterodyne frequencies. In particular, last generation discrete HBTs present a low base resistance $r_{\mathrm{BB}'}$ and high DC current gain β_0, both essential parameters for low electronic noise.

Chapter 3 focused on the efforts to experimentally characterize photoreceivers and components, also introducing a new type of photoreceiver developed in the frame of this thesis. The spatial response of three QPD models was obtained by scanning the samples in a LabVIEW-controlled setup. A new functionality upgrade for the software IfoCAD was developed in order to include the measured spatial responses in the simulated environments. Simulations using the measured responses demonstrated that the effects of non-uniform patterns do not significantly increase the coupling effect of beam tilt on the displacement and DWS measurands. The temperature coefficient of the responsivity R for a silicon photodiode (PC50-7) was measured to be $3.3 \times 10^{-3}\,\mathrm{A\,W^{-1}\,{}^\circ C^{-1}}$, or $1.57\,\%\,{}^\circ\mathrm{C}^{-1}$ after normalizing by $R(T = 0)$. The chapter also presented the experimental characterization of the GRACE-FO photoreceiver flight models. The characterization at unit level was necessary prior to integration in the satellites. The GRACE-FO photoreceivers showed an input current noise density below $3.5\,\mathrm{pA\,Hz^{-1/2}}$ for a single TIA channel, a thermal stability better than $5\,\mathrm{mrad\,K^{-1}}$ for the longitudinal phase and $100\,\mu\mathrm{rad\,K^{-1}}$ for the differential phase in the required frequency range. In the last section, a new photoreceiver design featuring discrete HBTs was presented. The design also features an off-the-shelf 0.5 mm diameter InGaAs QPD with a junction capacitance C_j of 3.6 pF. All photoreceiver channels exhibit an input current noise $\tilde{\imath}_\mathrm{en}$ of $1.9\,\mathrm{pA\,Hz^{-1/2}}$ at the LISA maximum heterodyne frequency, 25 MHz. The measured noise is $0.2\,\mathrm{pA\,Hz^{-1/2}}$ lower than in a previous design based on the EL5135 operational amplifier and the same QPD [77]. The reduction of photoreceiver noise translates to a $0.13\,\mathrm{pm\,Hz^{-1/2}}$ decrease of the photoreceiver contribution to the LISA readout displacement noise. The input current noise stays below $2\,\mathrm{pA\,Hz^{-1/2}}$ up to 30 MHz. The 3 dB bandwidth was measured to be 37 MHz. The effect of the collector current of the input transistor on the noise and bandwidth was studied. The collector current represents an adjustable design parameter not available in traditional OpAmp-only TIAs. An additional characterization using a larger QPD (GAP9119/GAP1000Q), which has a greater junction capacitance per segment ($C_\mathrm{j} = 11.5\,\mathrm{pF}$), shows an input current noise density below $3\,\mathrm{pA\,Hz^{-1/2}}$ at 25 MHz and a 3 dB bandwidth of 24 MHz. The measured power consumption of the full photoreceiver is 178 mW, thanks to the low power, transistor-based input stage and the OpAmps used. This constitutes an improvement compared to standard OpAmp-only photoreceiver designs, not optimized for power consumption. Due to the described performance, this new type of photoreceiver is a competitive candidate for future intersatellite interferometry missions.

Next steps for the photoreceiver development, particularly for the LISA mission, include the environmental test of the HBT-based design. Radiation hardness qualification and thermal tests in vacuum are planned for the photoreceiver prototypes and components. A redesign of the photoreceiver layout is also planned, in order to conform the constraints given in the LISA optical bench, such as beam height. A further improved design could be obtained from the combination of the HBT-based TIA and the custom-built low-capacitance QPDs from Discovery Semiconductors Inc [65]. Once the Hexagon experiment operates at pW optical levels, photoreceiver designs can be tested not only electrically but with LISA-like signals.

Appendix

This Appendix contains schematics and PCB layouts of circuits mentioned in the main text. The last section of the Appendix also contains the Python code for noise measurements using the white light technique and an MSO-X 4054A oscilloscope.

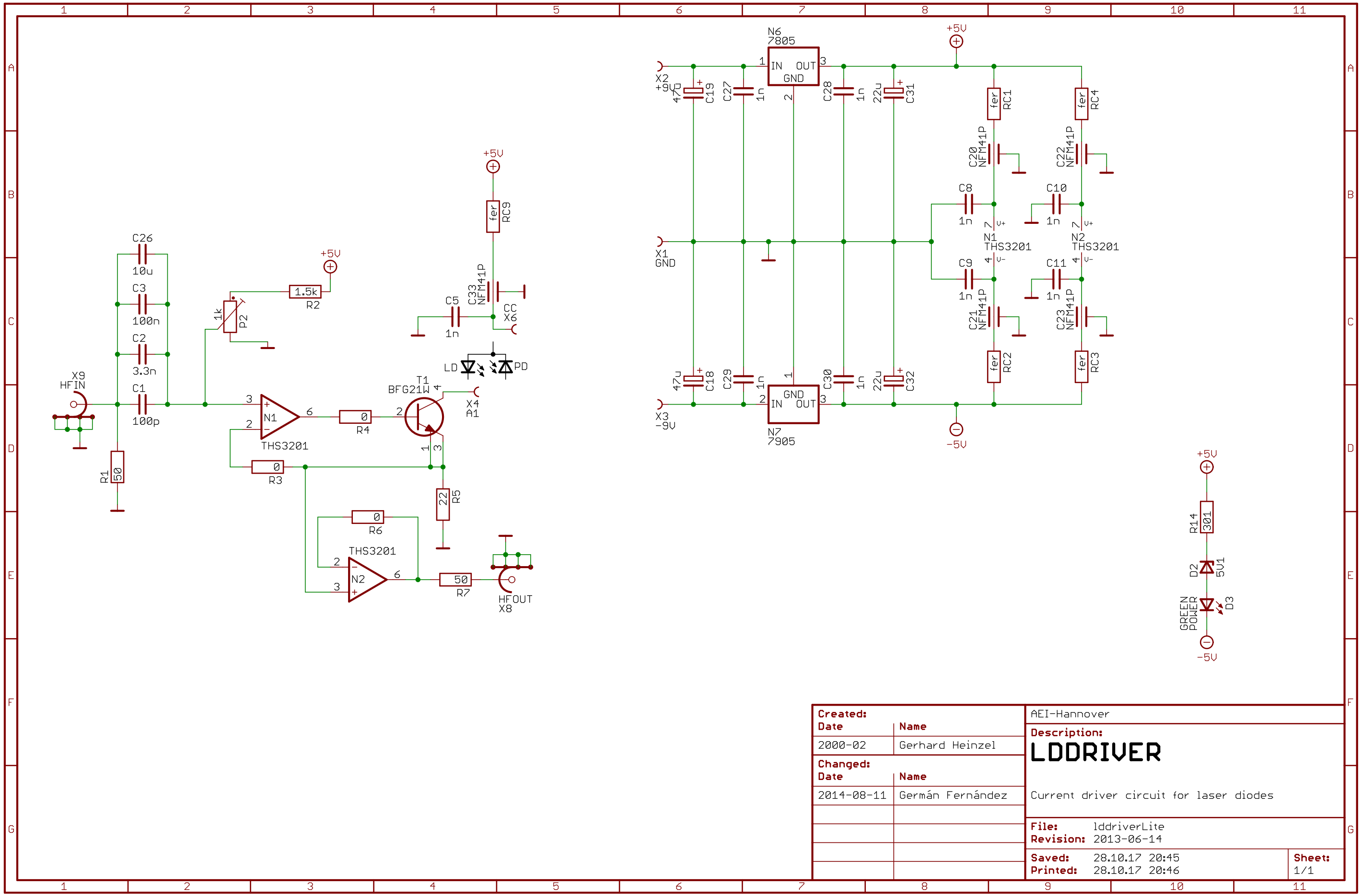
X9
HFIN
R1
50
C26
10u
C3
100n
C2
3.3n
C1
100p
1k
P2
1.5k
R2
+5V
N1
THS3201
0
R4
T1
BFG21W
X4
A1
0
R3
22
R5
0
R6
THS3201
N2
50
R7
HFOUT
X8
C5
1n
C33
NFM41P
CC
X6
fer
RC9
LD
PD
X2
+9V
47u
C19
C27
1n
N6
7805
IN
OUT
GND
C28
1n
22u
C31
X1
GND
X3
-9V
C18
C29
N7
7905
C30
C32
+5V
-5V
fer
RC1
RC4
C20
NFM41P
C22
C8
C10
C9
C11
C21
C23
RC2
RC3
N1
THS3201
N2
THS3201
V+
V-
R14
301
D2
5V1
GREEN
POWER
D3
Created:
Date
Name
2000-02
Gerhard Heinzel
Changed:
Date
Name
2014-08-11
Germán Fernández
AEI-Hannover
Description:
LDDRIVER
Current driver circuit for laser diodes
File: lddriverLite
Revision: 2013-06-14
Saved: 28.10.17 20:45
Printed: 28.10.17 20:46
Sheet:
1/1

Figure 4.1: Circuit diagram of the laser diode driver shown in Figure 3.16.

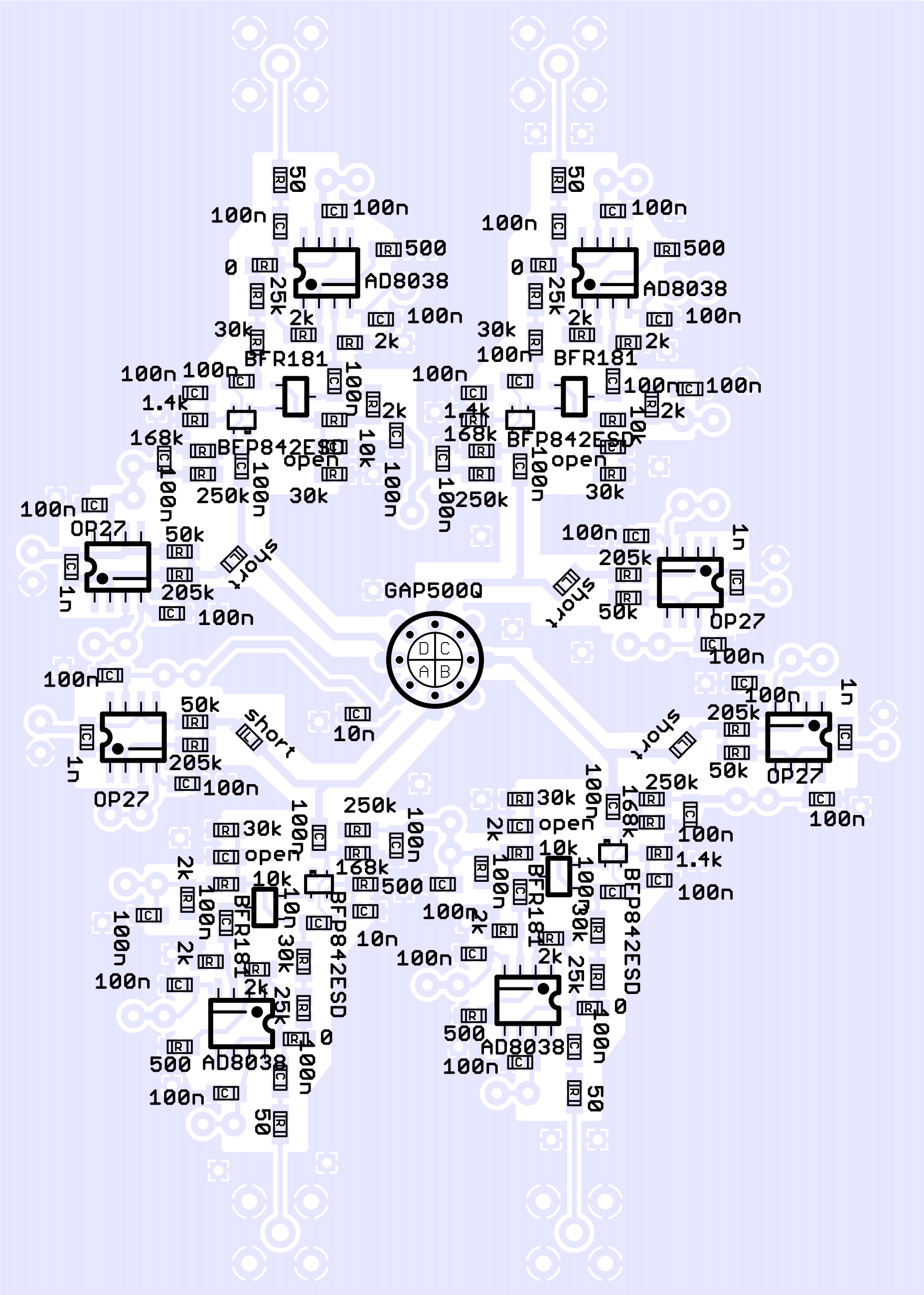
50
100n
100n
500
0
25k
AD8038
30k
2k
100n
2k
BFR181
100n
1.4k
168k
BFP842ESD
open
10k
250k
30k
OP27
50k
205k
1n
short
GAP500Q
D
C
A
B
10n

Figure 4.2: Layout of the HBT-based photoreceiver from Section 3.5.

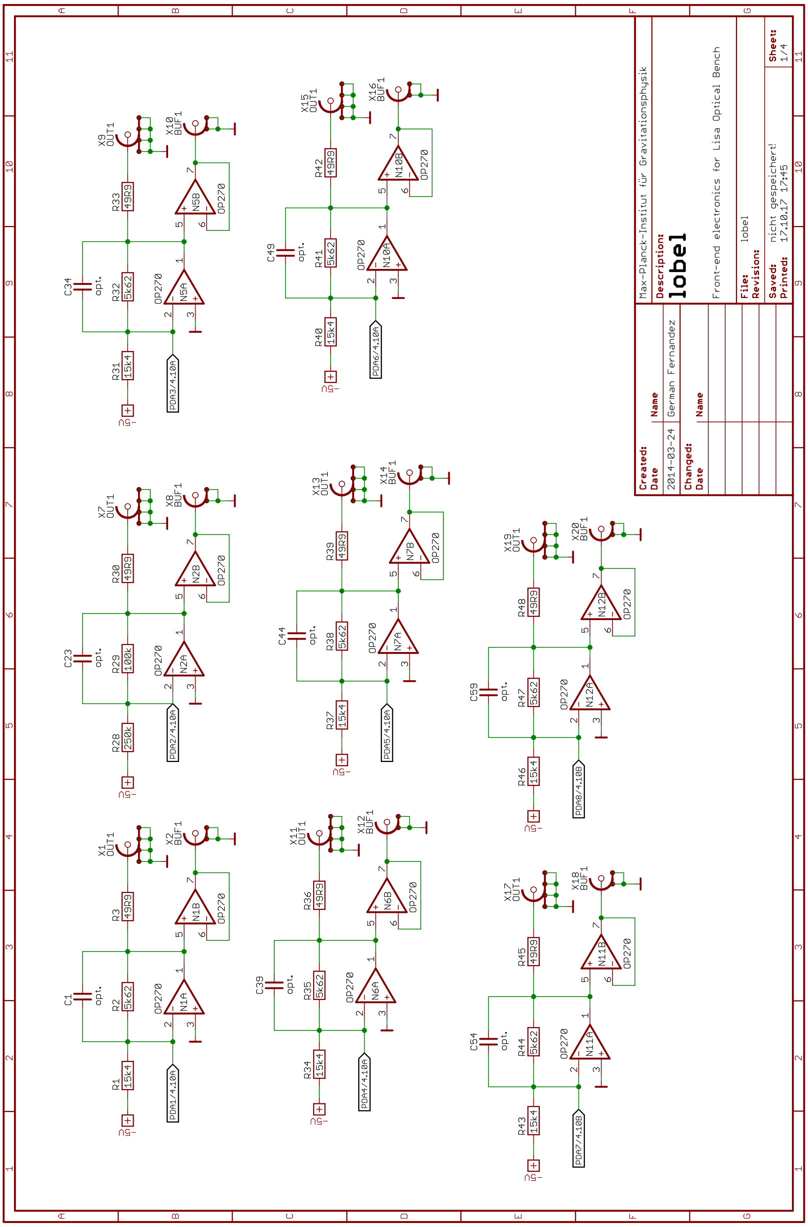
Max-Planck-Institut für Gravitationsphysik
Description:
lobel
Front-end electronics for Lisa Optical Bench
File: lobel
Revision:
Saved: nicht gespeichert!
Printed: 17.10.17 17:45
Sheet: 1/4
Created:
Date 2014-03-24
Name German Fernandez
Changed:
Date
Name
X1 OUT1
X2 BUF1
X7 OUT1
X8 BUF1
X9 OUT1
X10 BUF1
X11 OUT1
X12 BUF1
X13 OUT1
X14 BUF1
X15 OUT1
X16 BUF1
X17 OUT1
X18 BUF1
X19 OUT1
X20 BUF1
N1A
N1B
N2A
N2B
N5A
N5B
N6A
N6B
N7A
N7B
N10A
N10B
N11A
N11B
N12A
N12B
OP270
R1 15k4
R2 5k62
R3 49R9
R28 250k
R29 100k
R30 49R9
R31 15k4
R32 5k62
R33 49R9
R34 15k4
R35 5k62
R36 49R9
R37 15k4
R38 5k62
R39 49R9
R40 15k4
R41 5k62
R42 49R9
R43 15k4
R44 5k62
R45 49R9
R46 15k4
R47 5k62
R48 49R9
C1
C23
C34
C39
C44
C49
C54
C59
opt.
PDA1/4.10A
PDA2/4.10A
PDA3/4.10A
PDA4/4.10A
PDA5/4.10A
PDA6/4.10A
PDA7/4.10B
PDA8/4.10B
-5V

Figure 4.3: Circuit diagram of the LOB and ATA TIA electronics. The diagram shows 8 out of 16 TIAs channels for beat-note amplification in the kHz regime. Each channel implements an offset correction and a monitor output. The frequency response of a single channel is shown in Figure 3.18.

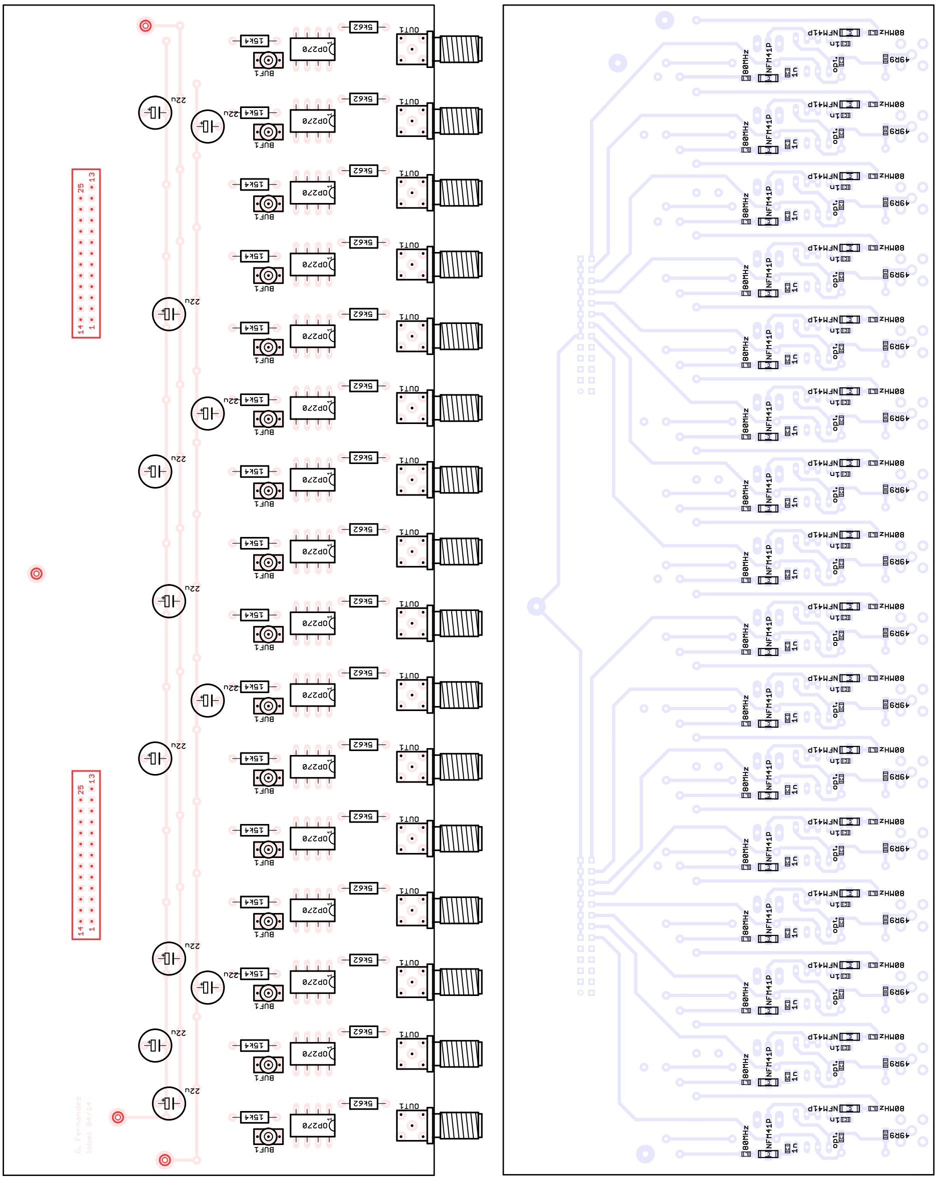
OUT1
BUF1
OP270
5k62
15k4
22u
80MHz
NFM41P
1n
10p

Figure 4.4: Layout of the LOB and ATA TIA electronics. The box includes a set of 16 TIA channels for beat-note amplification in the kHz regime. The frequency response of a single channel is shown in Figure 3.18.

Python code for noise measurements using the white light method (Section 3.3)

```python
import matplotlib.pyplot as plt
from scipy import signal
import numpy as np
import time
import datetime
import usbtmc

rf=20e3 # TIA DC gain
q=1.602e-19 # charge of an electron

instr =  usbtmc.Instrument(0x0957, 0x17b2) # ID of the MSO-X 4054 Agilent Osci
npoints=1000000 # Number of voltage samples
ch=1 # Channel 1 = AC Ch

oscidata=oscisave("1000000","1") # Number of points, Channel (AC output)
vdark=oscidata['voltage'] # Output AC voltage in dark conditions
fsample=oscidata['fs'] # Sampling frequency set in the oscilloscope

# The program  white light source is on
raw_input("Press Enter to continue...")

oscidata2=oscisave("1000000","1") # Number of points, Channel (AC output)
vlight=oscidata2['voltage'] # Output AC voltage with light

oscidataDC=oscisave("1000","2") # Number of points, Channel (DC output)
vDClight=np.mean(oscidataDC['voltage']) # Output DC voltage with light

# Timestamp for the output files
datetime=datetime.datetime.fromtimestamp(time.time()).strftime("%Y%m%d_%H%M%S")

# Saving voltage time series into a file
np.savetxt(datetime+'prnoise_'+'_'+str(int(-1*vDClight*1000))+'mV.csv', np.transpose([vdark,vlight]),delimiter=',', fmt=['%0.8f','%0.8f'],header="vdark,vlight")

# Calculating the voltage noise spectrum (FFT) with the Welch's method
N=1000
nenbw=1.5
f,Pxx_den_dark=signal.welch(vdark, fsample, window=('kaiser',5.0), nperseg=N, scaling='density')
f,Pxx_den_light=signal.welch(vlight, fsample, window=('kaiser',5.0), nperseg=N, scaling='density')

# Converting the spectrum to V/sqrt(Hz) units
vdark_den=np.sqrt(Pxx_den_dark)
vlight_den=np.sqrt(Pxx_den_light)

# Calculating the input current noise density i_en and the TIA gain
inoise=np.sqrt((2*q*(-vDClight/rf))/((vlight_den/vdark_den)*(vlight_den/vdark_den)-1))
tiagain=vdark_den/inoise

# Plotting the data
plt.close('all')
plt.figure(1)
plt.subplot(211)
plt.semilogx(f,inoise)
plt.ylabel('inoise [A/sqrt(Hz)]')
plt.grid(True, which="both")
#plt.xlim((1e6,30e6))
#plt.ylim((1e-12,5e-12))
plt.subplot(212)
plt.semilogx(f,tiagain)
plt.xlabel('Frequency [Hz]')
plt.ylabel('TIA gain [Ohms]')
plt.grid(True, which="both")
#plt.xlim((1e6,30e6))


# Defining the function to communicate and import data from
# the oscilloscope via SCPI and USB.
def oscisave(npoints,ch):
    instr =  usbtmc.Instrument(0x0957, 0x17b2)

    instr.write(":ACQuire:TYPE NORMAL")
    instr.write(":TIMebase:MODE MAIN")
    instr.write("WAVeform:POINts:MODE RAW") # Raw mode to use full oscilloscope memory
    instr.write(":WAVeform:SOURce CHANnel"+ch)
    instr.write(":WAVeform:FORMat BYTE")
    instr.write(":WAVeform:POINts "+npoints);
    instr.write(":DIGitize CHANnel"+ch)

    y_increment=float(instr.ask_raw(":WAVeform:YINCrement?"))
    y_reference=int(instr.ask_raw(":WAVeform:YREF?"))
    y_origin=float(instr.ask_raw(":WAVeform:YORigin?"))

    dataBytes=instr.ask_raw(":WAVeform:DATA?")
    dataBytes=np.fromstring(dataBytes,dtype=np.uint8)
    dataBytes=np.int_(dataBytes)
    dataBytes=dataBytes[10:dataBytes.size-1]
    voltage=(dataBytes-y_reference)*y_increment+y_origin
    fs=int(instr.ask(":ACQuire:SRATe?"))

    return {'voltage':voltage,'fs':fs}
```

Bibliography

[1] J. C. Wyant, “Interferometric Optical Metrology,” *Laser Focus*, p. 65, 1982.

[2] D. Martynov, E. Hall, B. Abbott, R. Abbott, T. Abbott, C. Adams, R. Adhikari, R. Anderson, S. Anderson, K. Arai, *et al.*, “Sensitivity of the Advanced LIGO detectors at the beginning of gravitational wave astronomy,” *Physical Review D*, vol. 93, no. 11, p. 112004, 2016.

[3] B. P. Abbott, R. Abbott, T. Abbott, M. Abernathy, F. Acernese, K. Ackley, C. Adams, T. Adams, P. Addesso, R. Adhikari, *et al.*, “Observation of gravitational waves from a binary black hole merger,” *Physical review letters*, vol. 116, no. 6, p. 061102, 2016.

[4] B. Abbott, R. Abbott, T. Abbott, M. Abernathy, F. Acernese, K. Ackley, C. Adams, T. Adams, P. Addesso, R. Adhikari, *et al.*, “GW151226: Observation of gravitational waves from a 22-solar-mass binary black hole coalescence,” *Physical Review Letters*, vol. 116, no. 24, p. 241103, 2016.

[5] B. P. Abbott, R. Abbott, T. Abbott, F. Acernese, K. Ackley, C. Adams, T. Adams, P. Addesso, R. Adhikari, V. Adya, *et al.*, “GW170104: Observation of a 50-Solar-Mass Binary Black Hole Coalescence at Redshift 0.2,” *arXiv preprint arXiv:1706.01812*, 2017.

[6] B. P. Abbott, R. Abbott, T. Abbott, F. Acernese, K. Ackley, C. Adams, T. Adams, P. Addesso, R. Adhikari, V. Adya, *et al.*, “GW170814: A three-detector observation of gravitational waves from a binary black hole coalescence,” *Physical Review Letters*, vol. 119, no. 14, p. 141101, 2017.

[7] B. P. Abbott, R. Abbott, T. Abbott, F. Acernese, K. Ackley, C. Adams, T. Adams, P. Addesso, R. Adhikari, V. Adya, *et al.*, “GW170817: observation of gravitational waves from a binary neutron star inspiral,” *Physical Review Letters*, vol. 119, no. 16, p. 161101, 2017.

[8] S. A. Hughes and K. S. Thorne, “Seismic gravity-gradient noise in interferometric gravitational-wave detectors,” *Physical Review D*, vol. 58, no. 12, p. 122002, 1998.

[9] H. Audley *et al.*, “Laser PInterferometer Space Antenna,” *arXiv preprint arXiv:1702.00786*, 2017.

[10] B. S. Sheard, G. Heinzel, K. Danzmann, D. A. Shaddock, W. M. Klipstein, and W. M. Folkner, “Intersatellite laser ranging instrument for the GRACE follow-on mission,” *Journal of Geodesy*, vol. 86, no. 12, pp. 1083–1095, 2012.

[11] M. Armano, H. Audley, G. Auger, J. Baird, M. Bassan, P. Binetruy, M. Born, D. Bortoluzzi, N. Brandt, M. Caleno, *et al.*, “Sub-femto-g free fall for space-based gravitational wave observatories: LISA pathfinder results,” *Physical review letters*, vol. 116, no. 23, p. 231101, 2016.

[12] European Space Agency, “Gravitational Wave mission selected, planet-hunting mission moves forward,” *ESA Space Science News*, 2017.

[13] K.-S. Isleif, L. Bischof, S. Ast, D. Penkert, T. S. Schwarze, G. Fernández Barranco, M. Zwetz, S. Veith, J.-S. Hennig, M. Tröbs, *et al.*, “Towards the LISA Backlink: Experiment design for comparing optical phase reference distribution systems,” *arXiv preprint arXiv:1709.06515*, 2017.

[14] J. Livas, S. Sankar, G. West, L. Seals, J. Howard, and E. Fitzsimons, “eLISA Telescope In-field Pointing and Scattered Light Study,” in *American Astronomical Society Meeting Abstracts*, vol. 229, 2017.

[15] J. Camp, K. Numata, and M. Krainak, “Progress and Plans for a US Laser System for LISA,” *Journal of Physics: Conference Series*, vol. 840, no. 1, p. 012013, 2017.

[16] B. D. Tapley, S. Bettadpur, M. Watkins, and C. Reigber, “The gravity recovery and climate experiment: Mission overview and early results,” *Geophysical Research Letters*, vol. 31, no. 9, 2004.

[17] B. Bachman, G. de Vine, J. Dickson, S. Dubovitsky, J. Liu, W. Klipstein, K. McKenzie, R. Spero, A. Sutton, B. Ware, *et al.*, “Flight phasemeter on the Laser Ranging Interferometer on the GRACE Follow-On mission,” in *Journal of Physics: Conference Series*, vol. 840, p. 012011, IOP Publishing, 2017.

[18] M. C. Teich and B. Saleh, “Fundamentals of photonics,” *Canada, Wiley Interscience*, vol. 3, 1991.

[19] O. Gerberding, “Phase readout for satellite interferometry,” *Ph.D. Thesis, Gottfried Wilhelm Leibniz Universität Hannover*, 2014.

[20] I. Cooper, “Doing physics with MATLAB. Computational Optics. Poynting Vector and Irradiance,” *School of Physics, University of Sydney*, 2014.

[21] A. H. Cook, “Interference of electromagnetic waves.,” *Interference of electromagnetic waves., by Cook, AH. Int. Ser. Monogr. Phys.(Oxford (UK): Clarendon Press), 8+ 253 p.*, 1971.

[22] T. Young, “A Course of Lectures on Natural Philosophy and the Mechanical Arts: In Two Volumes,” *Johnson*, vol. 2, 1807.

[23] N. Kipnis, “History of the Principle of Interference of Light,” *Birkhäuser*, vol. 5, 2012.

[24] J. Jamin, “Description d’un nouvel appareil de recherches, fondé sur les interférences,” *CR Acad. Sci. Paris*, vol. 42, pp. 482–485, 1856.

[25] A. Michelson, F. Pease, and F. Pearson, “Repetition of the Michelson-Morley experiment,” *JOSA*, vol. 18, no. 3, pp. 181_1–182, 1929.

[26] R. H. Brown and R. Q. Twiss, “LXXIV. A new type of interferometer for use in radio astronomy,” *The London, Edinburgh, and Dublin Philosophical Magazine and Journal of Science*, vol. 45, no. 366, pp. 663–682, 1954.

[27] J. Blayney and R. Gilman, “A portable strain meter with continuous interferometric calibration,” *Bulletin of the Seismological Society of America*, vol. 55, no. 6, pp. 955–970, 1965.

[28] W. H. Pielemeier, “The Pierce acoustic interferometer as an instrument for the determination of velocity and absorption,” *Physical Review*, vol. 34, no. 8, p. 1184, 1929.

[29] P. R. Berman, “Atom interferometry,” *Academic press*, 1997.

[30] R. G. Gould *et al.*, “The LASER, light amplification by stimulated emission of radiation,” in *The Ann Arbor conference on optical pumping, the University of Michigan*, vol. 15, p. 128, 1959.

[31] R. Drever, J. L. Hall, F. Kowalski, J. Hough, G. Ford, A. Munley, and H. Ward, “Laser phase and frequency stabilization using an optical resonator,” *Applied Physics B*, vol. 31, no. 2, pp. 97–105, 1983.

[32] M. Pitkin, S. Reid, S. Rowan, and J. Hough, “Gravitational wave detection by interferometry (ground and space),” *Living Reviews in Relativity*, vol. 14, no. 1, p. 5, 2011.

[33] B. Brandl, “Detection of Light. Principle of Heterodyne Receivers.,” *Universiteit Leiden*, 2015.

[34] H. Gernsheim, “A concise history of photography,” *Courier Corporation*, 1986.

[35] E. Becquerel, “On electric effects under the influence of solar radiation,” *Compt. rend.*, vol. 9, p. 561, 1839.

[36] A. Wilson, "The internal photoelectric effect in crystals," *Nature*, vol. 130, no. 913, p. I932, 1932.

[37] A. Arons and M. Peppard, "Einstein's Proposal of the Photon Concept. A Translation of the Annalen der Physik Paper of 1905," *American Journal of Physics*, vol. 33, no. 5, pp. 367–374, 1965.

[38] W. Lamb, "Anti-photon," *Applied Physics B: Lasers and Optics*, vol. 60, no. 2, pp. 77–84, 1995.

[39] J. Brugler, "Optoelectronic nomenclature for solid-state radiation detectors and emitters," *IEEE Journal of Solid-State Circuits*, vol. 5, no. 5, pp. 276–283, 1970.

[40] M. Tröbs, L. d'Arcio, S. Barke, J. Bogenstahl, I. Bykov, M. Dehne, C. Diekmann, E. Fitzsimons, R. Fleddermann, O. Gerberding, *et al.*, "Testing the LISA optical bench," in *Proc. of the Int. Conf. on Space Optics*, 2012.

[41] M. Chwalla, K. Danzmann, G. Fernández Barranco, E. Fitzsimons, O. Gerberding, G. Heinzel, C. J. Killow, M. Lieser, M. Perreur-Lloyd, D. I. Robertson, *et al.*, "Design and construction of an optical test bed for LISA imaging systems and tilt-to-length coupling," *Classical and Quantum Gravity*, vol. 33, no. 24, p. 245015, 2016.

[42] R. A. Pease, "What's all this transimpedance amplifier stuff, anyhow?," *Electron. Design*, 2001.

[43] O. Gerberding, C. Diekmann, J. Kullmann, M. Tröbs, I. Bykov, S. Barke, N. C. Brause, J. J. Esteban Delgado, T. S. Schwarze, J. Reiche, *et al.*, "Readout for intersatellite laser interferometry: Measuring low frequency phase fluctuations of high-frequency signals with microradian precision," *Review of Scientific Instruments*, vol. 86, p. 074501, 2015.

[44] S. Barke, "Inter-Spacecraft Frequency Distribution for Future Gravitational Wave Observatories," *Ph.D. Thesis, Gottfried Wilhelm Leibniz Universität Hannover*, 2015.

[45] M. Tinto and S. V. Dhurandhar, "Time-delay interferometry," *Living Reviews in Relativity*, vol. 17, no. 1, p. 6, 2014.

[46] M. Hewitson, E. Fitzsimons, and W. J. Weber, "LISA Performance Model and Error Budget - LISA-LCST-INST-TN-003," *Pending for publication*, 2018.

[47] G. Fernández Barranco, O. Gerberding, T. S. Schwarze, B. S. Sheard, C. Dahl, B. Zender, and G. Heinzel, "Phase stability of photoreceivers in intersatellite laser interferometers," *Opt. Express*, vol. 25, no. 7, pp. 7999–8010, 2017.

[48] T. H. O'Dell, "Electronic circuit design: art and practice," *Cambridge University Press*, 1988.

[49] O. Gerberding, C. Diekmann, J. Kullmann, M. Tröbs, I. Bykov, S. Barke, N. Brause, J. E. Delgado, T. S. Schwarze, J. Reiche, K. Danzmann, T. Rasmussen, T. Hansen, A. Enggaard, S. Pedersen, O. Jennrich, M. Suess, Z. Sodnik, and G. Heinzel, "Readout for intersatellite laser interferometry: Measuring low frequency phase fluctuations of high-frequency signals with microradian precision," *Rev. Sci. Instrum.*, vol. 86, p. 074501, 2015.

[50] T. J. Kane, A. C. Nilsson, and R. L. Byer, "Frequency stability and offset locking of a laser-diode-pumped Nd:YAG monolithic nonplanar ring oscillator," *Opt. Lett.*, vol. 12, no. 3, pp. 175–177, 1987.

[51] P. Kwee, "Laser characterization and stabilization for precision interferometry," *Ph.D. Thesis, Gottfried Wilhelm Leibniz Universität Hannover*, 2010.

[52] M. Armano, H. Audley, G. Auger, J. Baird, P. Binetruy, M. Born, D. Bortoluzzi, N. Brandt, A. Bursi, M. Caleno, *et al.*, "The LISA pathfinder mission," in *Journal of Physics: Conference Series*, vol. 610, p. 012005, IOP Publishing, 2015.

[53] A. Van Herwaarden and P. Sarro, "Thermal sensors based on the Seebeck effect," *Sensors and Actuators*, vol. 10, no. 3-4, pp. 321–346, 1986.

[54] R. H. Hadfield, "Single-photon detectors for optical quantum information applications," *Nature photonics*, vol. 3, no. 12, pp. 696–705, 2009.

[55] L. Werner, R. Friedrich, U. Johannsen, and A. Steiger, "Precise scale of spectral responsivity for InGaAs detectors based on a cryogenic radiometer and several laser sources," *Metrologia*, vol. 37, no. 5, p. 523, 2000.

[56] M. I. Dyakonov, "Basics of Semiconductor and spin physics," 2008.

[57] G. Pearson and W. H. Brattain, "History of semiconductor research," *Proceedings of the IRE*, vol. 43, no. 12, pp. 1794–1806, 1955.

[58] M. Barnoski, "Fundamentals of optical fiber communications," *Elsevier*, 2012.

[59] B. Van Zeghbroeck, "Principles of Semiconductor Devices," *University of Colorado Boulder Online Resources*, 2011.

[60] D. Colliver, "Germanium," in *Electronics Design Materials*, pp. 125–132, Springer, 1971.

[61] OSI-Optoelectronics, "Photodiode Characteristics and Applications."

[62] Thorlabs, *FDG03 Ge Photodiode*, 2017. Datasheet available at https://www.thorlabs.de/thorproduct.cfm?partnumber=FDG03.

[63] First Sensor, *PC50-6 TO - PIN Silicon PD*, 2011. Datasheet available at http://www.mouser.com/ds/2/313/PC50-6-TO8-10194.pdf.

[64] Hamamatsu, *Standard type InGaAs. InGaAs Photodiodes Selection Guide*, 2017. Available at https://www.hamamatsu.com/resources/pdf/ssd/ingaas_kird0005e.pdf.

[65] A. Joshi, S. Datta, J. Rue, J. Livas, R. Silverberg, and F. Guzmán Cervantes, "Ultra-low noise large-area InGaAs quad photoreceiver with low crosstalk for laser interferometry space antenna," *Proc. SPIE*, vol. 8453, pp. 84532G–84532G–10, 2012.

[66] H. Zhou, W. Wang, C. Chen, and Y. Zheng, "A low-noise, large-dynamic-range-enhanced amplifier based on jfet buffering input and JFET bootstrap structure," *IEEE Sensors Journal*, vol. 15, no. 4, pp. 2101–2105, 2015.

[67] T. Swe and K. Yeo, "An accurate photodiode model for DC and high frequency SPICE circuit simulation," in *Technical Proceedings of the 2001 International Conference on Modeling and Simulation of Microsystems*, vol. 1, pp. 362–365, 2001.

[68] C. Diekmann, "Development of core elements for the LISA optical bench - Electro-optical measurements systems and test devices," *Ph.D. Thesis, Gottfried Wilhelm Leibniz Universität Hannover*, 2013.

[69] Voxtel, "Avalanche Photodiode Receiver Performance Metrics."

[70] F. Koppens, T. Mueller, P. Avouris, A. Ferrari, M. Vitiello, and M. Polini, "Photodetectors based on graphene, other two-dimensional materials and hybrid systems," *Nature nanotechnology*, vol. 9, no. 10, pp. 780–793, 2014.

[71] N. Liu, H. Tian, G. Schwartz, J. B.-H. Tok, T.-L. Ren, and Z. Bao, "Large-area, transparent, and flexible infrared photodetector fabricated using PN junctions formed by N-doping chemical vapor deposition grown graphene," *Nano letters*, vol. 14, no. 7, pp. 3702–3708, 2014.

[72] M. A. Khan, K. K. Nanda, and S. B. Krupanidhi, "Reduced graphene oxide film based highly responsive infrared detector," *Materials Research Express*, vol. 4, no. 8, p. 085603, 2017.

[73] K. Zhang, X. Fang, Y. Wang, Y. Wan, Q. Song, W. Zhai, Y. Li, G. Ran, Y. Ye, and L. Dai, "Ultrasensitive Near-Infrared Photodetectors Based on a Graphene–MoTe2–Graphene Vertical van der Waals Heterostructure," *ACS applied materials & interfaces*, vol. 9, no. 6, pp. 5392–5398, 2017.

[74] H. T. Friis, “Noise figures of radio receivers,” *Proceedings of the IRE*, vol. 32, no. 7, pp. 419–422, 1944.

[75] X. Ramus, “Transimpedance considerations for high-speed amplifiers,” *Application Report SBOA122. Texas Instruments*, 2009.

[76] M. Gallant, “Transimpedance f3dB and Cf Design Curves for Maximally Flat Frequency Response,” *JavaScience Consulting*, 2012.

[77] F. Guzmán Cervantes, J. Livas, R. Silverberg, E. Buchanan, and R. Stebbins, “Characterization of photoreceivers for lisa,” *Classical and Quantum Gravity*, vol. 28, no. 9, p. 094010, 2011.

[78] Vishay, *Attain Audiophile-Level Music With Vishay MELF Resistors.* Technical Note VMN-AD0409-1607.

[79] G. Pruett and R. Petritz, “Detectivity and preamplifier considerations for indium antimonide photovoltaic detectors,” *Proceedings of the IRE*, vol. 47, no. 9, pp. 1524–1529, 1959.

[80] R. Wolfson *et al.*, “Circuit for improving the frequency response of photoelectric devices,” 1966. US Patent 3,240,944.

[81] A. Mitchell, M. O’mahony, and B. Boxall, “PIN-bipolar optical receiver using a high-frequency high-beta transistor,” *Electronics Letters*, vol. 19, no. 12, pp. 445–447, 1983.

[82] J. C. Bardin, “Silicon-Germanium heterojunction bipolar transistors for extremely low-noise applications,” *Ph.D Thesis, California Institute of Technology*, 2009.

[83] J. D. Cressler, “Silicon Heterostructure Handbook: Materials, Fabrication, Devices, Circuits and Applications of SiGe and Si Strained-Layer Epitaxy,” *CRC press*, 2005.

[84] P. Horowitz and W. Hill, *The Art of Electronics*, vol. 3. Cambridge university press Cambridge, 2015.

[85] E. Morrison, B. J. Meers, D. I. Robertson, and H. Ward, “Experimental demonstration of an automatic alignment system for optical interferometers,” *AO*, vol. 33, pp. 5037–5040, 1994.

[86] E. Morrison, B. J. Meers, D. I. Robertson, and H. Ward, “Automatic alignment of optical interferometers,” *AO*, vol. 33, pp. 5041–5049, 1994.

[87] H. Gong, L. Hanssen, and G. Eppeldauer, “Spatial and angular responsivity measurements of photoconductive HgCdTe LWIR radiometers,” *Metrologia*, vol. 41, no. 3, pp. 161–166, 2004.

[88] A. Lamminpaa, M. Noorma, T. Hyyppa, F. Manoocheri, P. Karha, and E. Ikonen, “Characterization of germanium photodiodes and trap detector,” *Measurement Science & Technology*, vol. 17, no. 4, pp. 908–912, 2006.

[89] L. C. Alves, F. Reis, M. C. Torres, G. B. Almeida, and I. B. Couceiro, “Spatial uniformity of the silicon photodiodes for establishment of spectral responsivity scale,” *Proceedings of the XIX IMEKO World Congress on Fundamental and Applied Metrology*, pp. 164–167, 2009.

[90] N. Fox, E. Theocharous, and T. Ward, “Establishing a new ultraviolet and near-infrared spectral responsivity scale,” *Metrologia*, vol. 35, no. 4, pp. 535–541, 1998.

[91] E. Theocharous, M. A. Itzler, J. Cheung, and C. J. Chunnilall, “Characterization of the Linearity of Response and Spatial Uniformity of Response of Two InGaAsP/InP Geiger-Mode Avalanche Photodiodes,” *IEEE Journal Of Quantum Electronics*, vol. 46, no. 11, pp. 1561–1567, 2010.

[92] G. Wanner, G. Heinzel, E. Kochkina, C. Mahrdt, B. S. Sheard, S. Schuster, and K. Danzmann, “Methods for simulating the readout of lengths and angles in laser interferometers with Gaussian beams,” *Optics communications*, vol. 285, no. 24, pp. 4831–4839, 2012.

[93] G. Fernández Barranco, M. Tröbs, V. Müller, O. Gerberding, F. Seifert, and G. Heinzel, “Spatially resolved photodiode response for simulating precise interferometers,” *Appl. Opt.*, vol. 55, no. 24, pp. 6688–6693, 2016.

[94] J. A. Arnaud, W. M. Hubbard, G. D. Mandeville, B. de la Clavière, E. A. Franke, and J. M. Franke, “Technique for Fast Measurement of Gaussian Laser Beam Parameters,” *Appl. Opt.*, vol. 10, no. 12, pp. 2775–2776, 1971.

[95] P. C. Hansen, “Discrete inverse problems: insight and algorithms,” *SIAM*, 2010.

[96] F. Blumenschein, “Spatially Resolved Characterization of RF QPDs,” *Master Thesis, University of Konstanz*, 2011.

[97] E. Kochkina, “Stigmatic and Astigmatic Gaussian Beams in Fundamental Mode - Impact of Beam Model Choice on Interferometric Pathlength Signal Estimates,” *Ph.D. Thesis, Gottfried Wilhelm Leibniz Universität Hannover*, 2013.

[98] P. Welch, “The use of fast Fourier transform for the estimation of power spectra: a method based on time averaging over short, modified periodograms,” *IEEE Transactions on audio and electroacoustics*, vol. 15, no. 2, pp. 70–73, 1967.

[99] M. Tröbs, M. Chwalla, K. Danzmann, G. Fernández Barranco, E. Fitzsimons, O. Gerberding, G. Heinzel, C. Killow, M. Lieser, M. Perreur-Lloyd, *et al.*, "Experimental demonstration of reduced tilt-to-length coupling by using imaging systems in precision interferometers," in *International Conference on Space Optics 2016*, vol. 10562, p. 1056245, International Society for Optics and Photonics, 2017.

[100] N. Brause, Y. H. Lee, S. Sönke, , G. Wanner, and G. Heinzel, "Optical noise sources of low Earth orbiter links," 2017.

[101] T. S. Schwarze, G. Fernández Barranco, D. Penkert, O. Gerberding, G. Heinzel, and K. Danzmann, "Optical testbed for the LISA phasemeter," in *Journal of Physics: Conference Series*, vol. 716, p. 012004, IOP Publishing, 2016.

[102] C. Dyer and D. Rodgers, "Effects on spacecraft & aircraft electronics," in *ESA WPPP-155 Proceedings of ESA Workshop on Space Weather*, pp. 11–13, 1998.

[103] K. Bedingfield, R. D. Leach, M. B. Alexander, *et al.*, "Spacecraft system failures and anomalies attributed to the natural space environment," *NASA Reference Publication 1390*, 1996.

[104] G. Fernández Barranco, B. S. Sheard, C. Dahl, W. Mathis, and G. Heinzel, "A low-power, low-noise 37-MHz photoreceiver for intersatellite laser interferometers using discrete heterojunction bipolar transistors," *IEEE Sensors Journal*, vol. 18, no. 18, pp. 7414–7420, 2018.

[105] I. Technologies, "BFP842ESD Datasheet. Robust Low Noise Silicon Germanium Bipolar RF Transistor"," *Datasheet*, 2013.

[106] V. Janásek, "Design of ultra low noise amplifiers," *www.janascard.cz*, 2017.

[107] S. Gupta, "How to pick a linear regulator for noise-sensitive applications," *Texas Instruments Application Note*, 2013.

Acknowledgments

I would like to thank Prof. Dr. Karsten Danzmann for giving me the opportunity of doing my research at the AEI in Hannover. It was a pleasure to work in such a great scientific environment, where assuring the best job conditions is always a priority. His enthusiasm and life-long dedication to the field of gravitational waves were always an inspiration. I would also like to thank Prof. Dr.-Ing. Wolfgang Mathis for accepting me as a Ph.D. candidate at the Institut für Theoretische Elektrotechnik of the Leibniz Universität Hannover. His advice on fundamental research and thesis writing kept me on track and helped me a lot to improve this dissertation.

As my direct supervisor, apl. Prof. Dr. Gerhard Heinzel was an extraordinary support to me during the last years. His vast knowledge in electronics (among many other fields) provided not only the foundation for this thesis but also the guidance along the way. No matter how tight his schedule was, he always had time to talk when I showed up at his office door. I am deeply grateful to him for sharing all that valuable knowledge.

It was a great experience to work in the diverse and welcoming atmosphere of the Space Interferometry group, where I could benefit from the expertise of my postdoc colleagues Vitali Müller and Michael Tröbs on many occasions. And, of course, from the guidance of Oliver Gerberding, who was not only capable of giving an answer to any question I would fire at him, but could also crack us up in any situation and keep us motivated during tough times.

I would like to thank my long-time office mates Daniel Penkert and Thomas Schwarze for their support and friendship. They did not mind me sharing whatever thought crossed my mind, whether it was a fundamental work-related question, philosophy of life, series gags or the last YouTube trend. Thanks to them, going to the office every day was something to look forward to. I am also grateful to my former office mates Stefan Ast, Heather Audley and Ingo Diepholz, whose company I enjoyed a lot.

A big thank you goes to all TEAM Mensa members over the years. Having lunch and coffee together became more of a cathartic ritual. I am also deeply grateful for all the trips, parties and moments we shared together. They also provided their sharp eyes and expertise for the correction of this thesis. For all of that, I want to thank Vaishali Adya, Oliver Gerberding, Víctor Huarcaya, Katharina-Sophie Isleif, Steffen Kaufer, Daniel Penkert, Marina Trad Nery, Thomas Schwarze and David Wu.

I want to express my gratitude to the staff members of the AEI, who do a superb job to reduce our workload: administration, IT department, mechanical workshop...

and in my particular case, special thanks to the colleagues of the electronic workshop. The hours in front of the soldering iron were more pleasant with their assistance and company.

During my time as a Ph.D. student, I could also be a part of the international effort to develop the Laser Ranging Interferometer (LRI) of the GRACE-FO satellites. I would like to thank my colleagues from the LRI team in Hannover but also all members at the DLR Berlin, STI and NASA JPL. It was a great experience working with them, night shifts included!

I would like to give my mates from Meute Royal a big shout-out for all the rehearsals, gigs and beverages shared over the last few years. Thanks for making me feel part of the gang. "Gemeinsam gehen wir diesen Weg".

I am deeply thankful to my family and friends in Almería, always caring about me, no matter the distance.

And the biggest thank you goes to my girlfriend Karo. I cannot really describe how grateful I am for being with such a supportive, strong and loving person. Regardless of the difficulties suffered, we grew together along this trip. Kocham Cię, Kochanie!

I want to acknowledge the DLR and the Bundesministerium für Bildung und Forschung (BMBF) for funding the LISA and GRACE-FO technology development. I am also indebted to the communities behind the multiple open-source software packages on which this thesis is based. Among all the software used, I would like to mention Kubuntu (OS), GNU Emacs (text editor), the SciPy (scientific and technical computing) and matplotlib (plotting) Python libraries, Inkscape (Vector graphics editor) and LaTeX (document preparation). I would like to thank my friends Abel Fernández López and Thomas Schwarze for helping me design the cover. I would also like to thank A. Franzen and the users of flaticon.com for creating the vector graphics components used in the figures of this thesis.

Curriculum Vitae

Germán Fernández Barranco
Oeltzenstraße 27
30169 Hannover

Born on December 7, 1988 in Almería, Spain

2000 – 2006	High School Diploma, I.E.S. Fuente Nueva
2006 – 2013	Master in Telecommunication Engineering, University of Granada
2011 – 2013	Master in Electrical Engineering, University of Granada
2010 – 2011	Erasmus Exchange Program, Warsaw University of Technology Excellence in International Mobility Award, University of Granada
2013 – 2017	Doctoral Studies, Albert Einstein Institute & Institut für Theoretische Elektrotechnik, Leibniz Universität Hannover
2013 – 2017	Member of the GRACE-FO Laser Ranging Interferometer Team
12/2013	Research visit at NASA Goddard Space Flight Center, Washington D.C.

Publications

Refereed journal articles

- M. Chwalla, K. Danzmann, **G. Fernández Barranco**, E. Fitzsimons, O. Gerberding, G. Heinzel, C. J. Killow, M. Lieser, M. Perreur-Lloyd, D. I. Robertson, S. Schuster, T. S. Schwarze, M. Tröbs, H. Ward and M. Zwetz. "Design and construction of an optical test bed for LISA imaging systems and tilt-to-length coupling" *Classical and Quantum Gravity*, Volume 33, Number 24, 2016.

- **G. Fernández Barranco** M. Tröbs, V. Müller, O. Gerberding, F. Seifert, and G. Heinzel. "Spatially resolved photodiode response for simulating precise interferometers" *Applied Optics*, 55(24), 6688-6693, 2016.

- **G. Fernández Barranco**, O. Gerberding, T. S. Schwarze, B. S. Sheard, C. Dahl, B. Zender, and G. Heinzel. "Phase stability of photoreceivers in intersatellite laser interferometers" *Optics Express*, 25(7):7999, 2017.

- K. S. Isleif, L. Bischof, S. Ast, D. Penkert, T. S. Schwarze, **G. Fernández Barranco**, M. Zwetz, S. Veith, J. S. Hennig, M. Tröbs, J. Reiche, O. Gerberding, K. Danzmann and G. Heinzel. "Towards the LISA Backlink: Experiment design for comparing optical phase reference distribution systems" *Classical and Quantum Gravity*, Volume 35, Number 8, 2018.

- M. Tröbs, S. Schuster, M. Lieser, M. Zwetz, M. Chwalla, K. Danzmann, **G. Fernández Barranco**, E. D. Fitzsimons, O. Gerberding, G. Heinzel, C. J. Killow, M. Perreur-Lloyd, D. I. Robertson, T. S. Schwarze, G. Wanner and H. Ward. "Reducing tilt-to-length coupling for the LISA test mass interferometer" *Classical and Quantum Gravity*, Volume 35, Number 10, 2018.

- **G. Fernández Barranco**, B. S. Sheard, C. Dahl, W. Mathis and G. Heinzel "A low-power, low-noise 37-MHz photoreceiver for intersatellite laser interferometers using discrete heterojunction bipolar transistors" *IEEE Sensors*, Volume 18, Number 18, 2018.

Conferences

- Development of photoreceivers for space-based interferometry
  Deutsche Physikalische Gesellschaft Spring Meeting
  March 2013, Hannover (Germany)

- Study of photoreceivers for space-based interferometry
  Edoardo Amaldi Conference on Gravitational Waves
  July 2013, Warsaw (Poland)

- Study of photoreceivers for space-based interferometry
  Deutsche Physikalische Gesellschaft Spring Meeting
  March 2014, Berlin (Germany)

- Study of photoreceivers for space-based interferometry
  LISA Symposium X
  May 2014, Gainesville (USA)

- Design and test of photoreceivers for space-based interferometry
  URSI Atlantic Radio Science Conference
  May 2015, Gran Canaria (Spain)

- Photoreceivers in present and future intersatellite laser interferometry
  LISA Symposium XI
  September 2016, Zurich (Switzerland)

- Optical three-signal test for the LISA phasemeter
  Deutsche Physikalische Gesellschaft Spring Meeting
  March 2017, Mainz (Germany)

- Photoreceivers in intersatellite laser interferometry
  Edoardo Amaldi Conference on Gravitational Waves
  July 2017, Pasadena (USA)